Laser Processing of Aluminum Alloys: Hypereutectic Al-Si Surface Remelting and Al6061- RAM2 Additive Manufacturing

by

Metin Kayıtmazbatır

A dissertation submitted in partial fulfillment
of the requirements for the degree of
Doctor of Philosophy
(Mechanical Engineering)
in the University of Michigan
2024

Doctoral Committee:

Professor Mihaela Banu, Co-Chair
Professor Amit Misra, Co-Chair
Dr. Tahany El-Wardany, RTRC
Professor Alan Taub
Professor Margaret Wooldridge

Metin Kayıtmazbatır

metink@umich.edu

ORCID iD: 0000-0001-6249-7976

Dedication

To the times I've spent away from my family

To all whose names I have not mentioned but who made the Ph.D. journey worthwhile in countless ways, I am eternally grateful for your unspoken contributions. In my quest for knowledge, I have relied on countless shoulders and for that, I thank you all.

Thank you for making this significant milestone in my academic journey possible

Table of Contents

List of Tables

List of Figures

Abstract

This dissertation undertakes a comprehensive exploration of laser processing of Aluminum alloys. The studies began with laser surface remelting, which is a basic form of laser-matter interaction. In Chapter 3, Aluminum-Silicon surface remelting experiments were designed around the laser, utilizing its ability to induce many different heat histories within the interaction zone. Microstructure transformation (from flakes to the fibers), microstructure refinement (increasing more than 100 times), creation of fully eutectic area (up to 90% of the processed area), and extension of the solid solubility limit of Aluminum due to high cooling rates were reported in this chapter. A processing-structure relationship was presented in terms of the undercooling amount (ΔT_k) for the readers' understanding. Additionally, the nano-mechanical hardness measurements of the laser-processed region were reported, and it was discovered that the laser-affected area was 1.5 times harder than the base plate.

After a certain knowledge of laser surface remelting, the research advances to additive manufacturing of commercial-grade Aluminum alloys: Al7075 (consisting of ~ 6% Zinc, 2.5 % Magnesium, 1.5 % Copper, and 1% Silicon) and Al6061-RAM2 (comprising of ~0.9% Magnesium, 0.7% Silicon, 0.6% Iron) reactive additive manufacturing variant with 2% ceramic addition. The former one studied for increasing the process yield by online defect detection, while the latter was for scaled-up prototyping. In Chapter 4, plasma signals emanating from laser-material interaction were monitored for defects (voids and cracks) detection within seconds. These signals are compared with the μCT data to identify and locate the defects. It was demonstrated that a randomly chosen spectrum signal can reveal a defect with 87% accuracy.

Chapter 5 investigates the direct metal deposition of Al6061-RAM2 in search of a printing strategy capable of creating functional prototypes at 1:100 and 1:20 scales. Preliminary studies within this chapter affirmed the ability to produce a rectangular

coupon with less than 2.5% porosity. Scaled prototypes at 1:20 for wind blade manufacturing molds (dimensions of 50x50x15 cm) were generated, showcasing intricate interior details due to topology optimization, based on the previous chapter's findings. These printed modules underwent testing for dimensional accuracy and vacuum integrity, to confirm the absence of connected porosities from production states. The results were highly satisfactory, asserting the practicality of direct metal deposition for creating complex molds at a 1:1 scale.

Chapter 1 Introduction

1.1 Motivation

The Earth's crust has been the sole source of metals mankind uses and will likely remain so for the next few decades. Aluminum (Al) and Silicon (Si), taking pride in place among the most abundant elements on the earth, are at the heart of this study. Although their mechanical properties and extraction process have posed challenges as compared to other prevalent metals such as iron and copper, advancements in pre-processing and post-processing tools over the last two centuries have overcome these hurdles.

The aviation and automotive industries' evolution, coupled with a burgeoning need for lighter materials, have spurred exciting research into Al and its alloys. This shift is clearly demonstrated by the five-fold increase in vehicle aluminum content over the past 45 years, surging from 84 to 469 pounds per vehicle.

Stimulated by accessibility and interest in their application, experimental and manufacturing procedures for aluminum (Al) and its alloys have considerably improved. Subsequently, these advancements have been accompanied by the evolution of quality assurance strategies. Therefore, the escalating volume of literature on aluminum points to a significant increase in research interest in this field.

Our exploration further extends into the domain of Light Amplification by Stimulated Emission of Radiation, or in a known form; LASER, an invention of the 1960s. Manipulation of light properties like directionality, coherence, and wavelength through lasers has opened the doors to wide-ranging contactless operations, spanning from the medical sector to aerospace. In

this aspect, it is one of the most marvelous accomplishments mankind has achieved. If there had been a time traveler from past centuries, scientists would have faced extreme difficulties in explaining how an invisible form of energy (infrared lasers) can kill or severely damage a human.

Laser material processing is yet another way of utilization of this light source in modern science. To list a few: laser melting, laser cutting, laser welding, laser bending, laser cleaning, laser shot peening, laser cladding, and laser additive manufacturing. Each technique leverages the distinct and mutable properties inherent to light. The laser, acting as a potent and adjustable energy reservoir, offers numerous manipulative parameters: beam diameter, focal depth, energy polarization, gating (an attribute enabling the release of energetic streams in a designed pattern), and one cannot forget the crucial influence of the power in the incident beam.

Focusing a laser on a small area enables us to increase its power density (Equation 1.1) many times. Such a mechanism culminates in an exceedingly condensed energy source, leading to temperature magnification within the localized region by several orders of magnitude. Surpassing the temperature of the sun's surface was accomplished many years ago with lasers [1] and currently, many research workshops around the world are able to attain these temperatures with relative ease. This huge concentration of energy possesses many opportunities in material processing. The materials subject to these processes could even be biological entities, such as corneal stroma cells.

$$\frac{Laser\ Power\ [W]}{Laser\ Spot\ Area\ [mm^2/s]} \qquad (1.1)$$

The thermal history of a material—its exposure to heating and cooling processes—substantially dictates its resultant state, influencing its characteristics, structural formation, and

spatial dimensions. The field of thermodynamics, often analogized to the science of metal mixing, elucidates the inherent influence of heat and pressure on phase transitions within metallic substances. Nevertheless, the practical application of these foundational principles in real-world scenarios poses inherent complexities, thereby necessitating the specialty field of 'Heat Treatment'.

Amplifying the intricacy of the computations of these physical phenomena, these calculations must be dynamically solved across each grid domain and each time increment. Such requirements proliferate the computational duration, from several days to several weeks. Although research-oriented environments may accommodate these extended time frames, high-velocity settings such as manufacturing industries increasingly necessitate more efficient methods. Consequently, this situation has incited a competitive struggle between two distinct scholarly perspectives seeking to streamline and optimize this computationally intensive procedure.

1.2 State of the art

1.2.1 Laser Surface Remelting

Laser Surface Remelting (LSR), an operation of remelting a thin layer from the surface of substrates, serves as a valuable approach to understanding unconventional solidification in metal alloys. Hence, the final microstructures, phases, and solid solubilities can be deduced from that solidification path.

Owing to the nature of the Al-Si binary system, especially particularly the lack of nucleation of intermetallic phases, it presents a comparatively simpler framework to manipulate and early researchers like Lu and Hellawell took advantage of it and reported the growth mechanism[2]. Some cooling rate calculations and microstructural characterizations pertaining to

the Al-Si system were reported in a paper by Xu *et al.*, on the melt-spun technique[3] and in a paper penned by Kalay *et al.* on the gas-atomization method[4].

The modern studies that incorporate laser as an energy source in this topic date back to the early 90s[5]. There, Pierantoni *et al.* employed a high-power CO2 laser and partially remelted the top surface of an Al-Si alloy and reported their findings about its solidification parameters. Dinda *et al.* reported the equilibrium Al-Si production via laser Direct Metal Deposition (DMD) technique, which has quite similar solidification parameters to LSR.

Laser Surface Remelting (LSR) may be instrumental in explaining the underlying mechanics of a prevalent additive manufacturing methodology, namely Laser Powder Bed Fusion (LPBF). While LPBF predominantly engages with dispersed powders, the rapid movement of a laser across a selected surface displays substantial similarity to the LSR procedure.

The meticulous refinement of microstructures within certain alloys can bring about significant enhancements in the final mechanical attributes of materials. Scientific inquiry over an extended period has engendered a multitude of techniques aimed at achieving such refinement. These include the addition of minor elements, hot forging, and the application of ultrasonic treatment (referred to as sonotrode application) during the solidification phase, among others. In addition, LSR materializes as another efficacious tool in facilitating microstructural refinement.

Highlighted by its extraordinarily high cooling rates, LSR restricts the requisite nucleation time for larger microstructure formation (agglomeration). Upon the material reaching temperatures below its solidus threshold, insufficiency in sustaining heat diffusion arises within

the remelted zone. To further augment the efficacy of microstructural refinement, a synergistic application of the aforementioned techniques may be executed concurrently.

1.2.2 Direct Metal Deposition

Another metal deposition technique, known as Direct Metal Deposition (DMD), or Directed Energy Deposition (DED) in its universally accepted nomenclature, underscores another application. In this method, the feedstock materials can comprise of wire or powder contingent upon the specific application requirement. Similarly, a high-energy laser or electron beam might be utilized to catalyze the melting of the incoming feedstock material. Within the context of this study, the author has explored a powder delivery DMD system, fitted by a solid-state, infrared (with a wavelength of 1030 nm) laser beam.

Powder-based laser DMD systems exhibit certain superiorities over their powder-bed counterparts. These include an approximately tenfold elevation in build rate, the capability to work with multiple powders simultaneously, the flexibility to alter the compositional mixture of the powders during the operational phase, and the proficiency to repair existing components that have experienced partial fractures. Notwithstanding their substantial contributions to materials research, these attributes carry practical implications for industrial applications, particularly in the manufacture of larger components (defined as one of the dimensions exceeding 1 meter throughout this dissertation).

In essence, the system conventionally depends on localized gas shielding to protect the metal from oxidation and hence does not necessitate investment in expensive vacuum and/or inert enclosures. Further, the operational chamber can be equipped with a diverse array of sensors for data acquisition. These can include optical emission spectrometers, contact

(thermocouples) or non-contact (pyrometers) temperature sensors, high-speed cameras, metrology sensors, and even secondary machining heads.

1.3 Gap in the field

Thermodynamic sciences explain to us what should happen when you cool a mixture of elements down in terms of microstructure formations and their respective composition. This is true under certain conditions, generalized under "equilibrium" terms. However, situations where a matter undergoes huge pressure, or a large heating/cooling cycle are studied in a different topic: non-equilibrium. Laser-matter interaction is a subject of the latter. Therefore, the final microstructures formed within the solidified region after a laser operation require further studies to account for the discrepancies.

Microstructure refinements have been a topic of interest for over a century. Whether it is refinement of a grain or secondary phase, it holds the potential to improve the mechanical properties of metals. As put forward by the Hall-Petch relationship (Equation 1.2), finer grains result in higher yield strength due to grain boundary blockades of slips. While this is the case, efforts of the microstructure refinements have been on individual methods. There is a lack of experiments on how combinations of these methods would result in. In particular, the control groups and the experiment groups need to be studied.

$$\sigma_y = \sigma_{y0} + k/d^x$$

(1.2)

The heat history calculations induced by a laser have always been a complicated problem because of the nature of the laser; being too powerful for a contact measurement method not having constant heat flux due to the effects like inverse bremsstrahlung and so on. As many

6

phenomena occur at the same time (phase chances, flow disturbances, transport phenomena, dynamically changing thermophysical properties, etc.), the calculation of a heat history gets complicated and requires a holistic multi-physics approach. However, those methods come with a high computation requirement. One second of real-time calculations may take up to 14 days with supercomputer clusters, therefore making it almost useless for real-world, on-time applications. Determining the heat history in a fast way is crucial for researchers to control and manipulate the processing parameters in laser material processing.

Direct Metal Deposition (DMD) is another way of printing metals for novel applications or repairing intricate parts with dimensional accuracy. However, there are as many as 18 parameters to control in DMD and the method of discovering the suitable parameters takes a long time to be practical. This issue needs to be addressed in a small increment. One example would be the printing strategy of a material via direct metal deposition, starting with complete darkness to full-scale printing. Such information is quite critical and can be considered confidential business information (a trade secret) to many professionals. However, a method to discover these in a scientific way can be offered to the community through this dissertation.

Metal additive machines are expensive tools to own and operate. Depending on the machine type, an average minimum price starts around half a million dollars. If there is such an investment, it is expected to create bigger value for its owner. As mentioned earlier, it is not an easy task to manufacture a part using this method. The scenario of producing defective parts in these machines is highly possible but totally unacceptable. Moreover, due to its layer thickness (which can be as low as 20 μm), manufacturing a part is going to take from 10 to 40 hours. Mechanical testing of these parts until their failure is a standard method for quality assurance in conventional manufacturing. This becomes not so cost-effective in additive manufacturing.

Under those circumstances, producing a part in one cycle and in a proper way is crucial. Any attempt to serve this purpose is valuable and needed in the scientific and industrial community.

1.4 Proposed approach

A thorough design of experiments with changing laser beam sizes, laser powers, and scanning speeds needs to be planned. Evaluation of the results in a Taguchi method, and repetitions of a few selected and promising experiments to make sure it is replicable, are the main philosophy throughout this dissertation. Microstructure refinement is done with a combination of laser surface remelting and trace element addition (cerium and strontium). The formed microstructures will be characterized by their sizes and refinement levels.

The interaction between a laser and a material generates plasma above the material's surface. To capture and analyze this plasma, Optical Emission Spectroscopy—a relatively economical method— is employed which may provide critical insights to operators involved in metal-printing from the deposition process. During the printing of Aluminum 7075, plasma monitoring will occur in real-time using a combination of a collimator lens and fiber cables. The captured light is subsequently transmitted to Ocean Optic's HR2000+ device. The device's reading, taken at a temporal resolution of 10 milliseconds, will consist of 2038 elements ranging between a wavelength of 320-410nm. Following the printing process, the deposition beads will undergo preparation for micro-computed tomography (μCT), which will detect any present pores in increments of 10 microns. A software environment will be employed to identify correlations between the in-situ plasma signals and the ex-situ μCT images, considering that the latter disclose the final product's defects including porosities and micro-cracks and effectively serve as an indicator of the process outcome.

Last but not least, the DMD of a new powder (in our case, it is Al6061RAM2) will be examined. While the literature is full of the final results of materials; to the author's best knowledge, there is no step-by-step guideline for the initial printings on the DMD system. Here, this gap is aimed to be addressed. Once completed, scale-up productions toward functional deposited prototypes are also reported in this study.

Chapter 2 Literature Review and Background

In this chapter, a comprehensive examination of existing literature pertinent to laser processing is undertaken. Chapter 3 discusses surface remelting, while chapter 4 and chapter 5 mention the in-situ monitoring via spectroscopy, and direct metal deposition for larger parts, respectively. The succeeding chapters seek to introduce innovative conclusions, building upon the foundational knowledge constructed via the comprehensive literature review articulated within the present chapter.

2.1 Laser Surface Remelting of Hypereutectic Aluminum Silicon Alloys

Aluminum (Al) alloys have undergone extensive scientific evaluation for their potential applications, most notably within the automotive and aerospace sectors [6]. The inaugural scholarly documentation on this subject can be traced back to the latter stages of the 19th century [7]. Al alloys with various content of Silicon (Si) also follow the same trend. Initial explorations primarily concentrated on hypo-eutectic Al alloys. Subsequent research commenced gravitating towards eutectic and hyper-eutectic alloys, as a consequence of their favorable strength-to-weight ratio, enhanced machinability, and exceptional resistance to wear[8].

In their scientific observation, Tenekedjiev *et al.* remarked on the composite material-like attributes exhibited by Silicon (Si) fibers embedded within an Aluminum (Al) matrix. Notably, this instance represents one of the rare occurrences where the incorporated reinforcement material possesses a lower density than the matrix itself. To elaborate, Aluminum and Silicon exhibit densities of 2.7 g/cm^3 and 2.35 g/cm^3 respectively. This unique property of Al-Si alloys

makes it a good candidate for applications where light-weighting is needed [9]. In equilibrium conditions, Al-Si alloys form a eutectic structure at 12.6 Si weight percent[10]. However, non-equilibrium conditions like a very high cooling rate ($10^3 - 10^8$ K/sec), often generated by a laser heat source, may result in a shift of eutectic point toward higher Si composition [11]. With increasing Si content, Al-Si alloys perform better in terms of mechanical properties like fracture toughness, hardness, and tensile strength. However, Si starts to nucleate in a polygonal form once it exceeds a certain threshold, which is also detrimental to the overall mechanical properties. So, a method that combines higher Si content and refinement in the Si particles might enable promising final properties for this alloy system. To that end, the author of this dissertation planned to employ laser surface remelting for this study. It has been reported that laser-processed alloys have ultra-fine microstructure, causing high strength, up to five times higher than alloys made by conventional means [12]. Consequently, Al-Si eutectic structures, bearing a high silicon content (>12.6 wt.%), cultivated under non-equilibrium conditions, may pose as an efficacious alternative material selection within industrial applications.

Estimating the final dimensions of the laser-processed material, called melt pool, with the help of spectral signals is particularly important because it provides in-situ results. Conventionally, the processed part needs to be prepared for SEM by mounting, polishing, and etching, then requires relatively expensive equipment as well as a trained user for characterizations. All that process takes around two days. Utilization of spectral signals as a process output reduces this time requirement drastically: to milliseconds. Moreover, the signal can be utilized as feedback for the laser process. Throughout these processes, the plasma signals generated by laser-material interaction are planned to be monitored. Optical emission spectral data in the range of 320 to 410 nm were collected as signal output, as this is where most of the

metal plasma's emissions occur [13]. Then, these signals were processed via Smart Optical Manufacturing Systems (SOMS) software to characterize the microstructure and estimate the dimensions of the melt pool. Similar studies are available elsewhere[14]–[16] This work will try to establish and present yet another correlation between plasma signals and melt pool dimensions.

Aluminum (Al) and Silicon (Si) are the 2nd and 3rd most abundant elements in the Earth's crust[17]. Still, these elements lag behind steel in terms of production and use due to steel's unmatched strength and cost-effectiveness. However, there has been an effort to switch from steels to Al alloys[18] for structural [19] and tribological applications[20]. The higher strength-to-weight ratio of Al-Si alloys makes it a good candidate for industries interested in lightweighting[21]. In addition, Al-Si alloys exhibit good weldability, castability, corrosion resistance, wear resistance, and high thermal conductivity [22], and Al-Si alloys promise good recyclability. To fully take advantage of the harder Si phase, more attention was gradually moved from hypo-eutectic (<12.6 wt.% Si) to hypereutectic Al-Si alloys[23], [24]. However, Si tends to nucleate as large flakes in hypereutectic Al-Si alloys, significantly increasing the propensity for crack formation. Therefore, methods to refine and control the morphology and distribution of Si in Al-Si alloys are an area of active investigation.

Many ways have been developed to refine primary and eutectic Si particles. For conventional casting, refinement starts with stirring of the alloy melt, originally done mechanically and nowadays performed electromagnetically[25] or via ultrasonic treatment[26]. Chemical modification of the molten liquid has been examined to hinder Si segregation, by the addition of Na [27], [28]and P[29], [30]. Likewise, chemical modification by rare earth elements microalloying is studied for Ce[31], [32], Sr[33], Y[34], La [35], Eu[36], [37], Yb[38] and Nd

[39]. Chemical modification often leads to thermodynamically favorable phases other than primary Silicon, thereby reducing the degree of Si segregation. However, the excess addition of rare earth elements leads to the formation of intermetallic phases that can be detrimental to the ductility and toughness of the alloy [40]. Melt spinning [41], thin film deposition [42], and gas atomization[43] have also been used for micro to nanoscale research and applications for refined Si phases. Another method for Al-Si alloy refinement is laser surface remelting (LSR)[44]–[46]. The technique involves scanning a high-power laser across a polished surface. The laser quickly heats the surface of the alloy above the liquidus temperature, forming a shallow melt pool. Due to the high thermal conductivity of the Al alloy and fast laser scan speed, the trailing end of the melt pool solidifies with estimated cooling rates up to 10^6 K/s [47]. If excimer lasers are used, cooling rates estimated from measured cell spacing could be up to 10^9 K/s [48]. Cooling rates are dependent on many process parameters such as laser power and laser scanning speed. There has been research on chemical, mechanical, and high energy beam (laser or electron beam) modifications as well as their combination[49].

Although LSR leads to microstructure refinement, the microstructure within the melt pool can vary from fully eutectic to hypoeutectic (mixture of primary Al dendrite and eutectic) with fine Si precipitates eventually forming in the Al dendrites[50]. In this work, the effect of LSR process parameters and rare earth elements, cerium (Ce) and strontium (Sr), on the microstructure in the melt pool of Al-20Si alloys planned to be studied, in particular, to correlate the cooling rate with the microstructure, specifically with the volume fraction of the fully eutectic regions in the melt pool as well as the size of eutectic Si particles. This combinatory effect of LSR and rare earth element alloying of Ce or Sr has not been investigated in prior literature and is not correlated quantitatively with the cooling rate, to the owner of this

dissertation's best knowledge. For LSR, the laser power was varied in a range that caused melting within a thin layer at the surface. The cooling rates for these experiments were estimated using the Eagar-Tsai model[51] with backward-fitting. A correlation between the cooling rate and the size and morphology (eutectic versus hypoeutectic) of the microstructure within the melt pool will enable the tailoring of the microstructure in laser-processed and printed alloys for high strength and plasticity.

To reiterate, the use of high silicon substance Al-Si alloys in the automobile, aerospace, and transport industries has been constantly increasing due to their excellent mechanical, tribological, and casting properties[52], [53]. However, when the silicon content exceeds 20 wt.%, the alloys suffer from a deterioration of other mechanical properties due to the formation of massive and angular silicon particles with sharp edges, which act as crack initiation sites and significantly reduce fatigue life. Therefore, to meet the growing demands in automotive, transport, aerospace, marine, aeronautical, and missile technology; the size and morphology of the silicon phase must be refined and modified as the finer primary silicon crystals generally result in improved mechanical properties, such as toughness and ductility[54].

For the hypereutectic Al-Si alloys, where the microstructure consists of coarse, angular, and irregular shapes of the primary Si immersed in Al-Si eutectic, the phosphorus (P) proved to be an effective modifier and refiner of primary Si particles but not for the eutectic Si[55]. Wu *et al.*[56] have reported that the addition of phosphorus to the Al-20 wt. %Si alloy with a controlled temperature and holding time has led to a reduction of the size of the primary silicon to 20 μm due to the formation of primary Al particles, which acted as a heterogeneous nucleation agent on the solid primary Al particles, which promotes the modification and refinement of the primary Si without affecting the eutectic Si morphology. A combination of P with other elements was also

investigated to refine the primary and the eutectic Si. Faraji *et al*.[57] have demonstrated that (P + Sr) was effective to some extent in improving the strength and ductility but the size of the primary silicon crystals did not reach the nanoscale size. Li *et al*.[58] have demonstrated that the morphology of primary Si was refined from coarse irregular star-like and plate- like shape to fine block-like when the addition contents of Y increased to 0.8%. The average size of primary Si reduced from 89 μm to 33 μm. Xia *et al*.[59] have reported that the addition of Erbium (0.5%Er) refined the primary Si from 94 μm to 33 μm and the morphology transfers from a coarse star-like and polygonal shape to a fine blocky shape. A similar result was obtained by the addition of Er to 0.5%[60]. However, when the level of rare earth Er was up to 0.8%, the primary and eutectic Si phases became coarser. It is clear from the above-mentioned research that modification of hypereutectic Al-Si alloys by chemical additions is not efficient in reducing the size of the primary Si to a micron- scale or nano-size, nor does it produce a desirable shape. Besides, there are a lot of negatives resulting from the chemical agents, such as evaporation, and oxidation during services. Qian *et al*.[61] and Liao *et al*. [62] have reported that Sr modifier increases the porosity level and deteriorates the performance of the castings.

Rapid solidification methods, such as melt spinning[41], powder atomization [4], and laser melting[63]–[68] proved to be effective approaches for the refinement of the Si phase. The high-cooling rates associated with these processes, which may reach up to 10^7 °C/s play a large role in the size of the critical nuclei, and subsequently, the effective number of nuclei that will ultimately produce fine-grained structures. Chaus *et al*. [69] have recently shown that rapid quenching technology resulted in significant grain refinement of the eutectic constituents (α (Al) + Si), as well as primary silicon, which gave rise to better tensile and fracture properties compared to that of the conventionally cast Al-18%Si-2%Cu alloy. Xu *et al*. [3] decreased;

obtained a 40 µm thick melt-spun ribbon by using a single roller melt- spinning technique of the Al-20 wt.%Si alloy and reported a drastic change in the morphology of the primary Si to fine block-shape with a significant reduction in the size to 2 µm. Kalay *et al*. [4] have studied gas-atomized Al-Si powders of different compositions (15, 18, 25, and 50 wt.%Si), and showed that as the droplet size decreased, the structure became much finer. The primary silicon in Al-50 wt.%Si alloy continued to form even at the smallest droplet sizes (25 µm) with sizes ranging from 2 to 5 µm, the Al-25 wt.%Si showed a predominantly eutectic state with a few primary Si while Al-18 wt.%Si, and Al- 15 wt.%Si showed dendritic and eutectic structures. Laser surface treatment of hypereutectic Al-Si alloys has been studied by several investigators, who showed a reduction of the primary Si to 10 µm, and the formation of fibrous eutectic Si. Bhowmik *et al*.[68] have recently developed Al-50 wt.%Si laser-clad on Al 7075 substrate and found local heterogeneity in the composition and the structure with the single clad layer due to different cooling rates. Three phases, namely primary Si of size, Al-Si eutectic, and α-Al dendrites were obtained with an increase in the solubility of Si in Al. Recently, Abboud and Mazumder [64] have produced a series of Al-Si layers on a commercially pure Al substrate with compositions 35, 50, and 60 wt.% and showed a great refinement in all the micro- structural constituents and increased hardness and the highest cooling rates did not suppress the formation of the primary Si but reduced the sizes to 2 µm and increased the amount of the nano-fibrous eutectic. Lien *et al*. [65] reported a high density of nano-twinned ultrafine Si in hypereutectic Al-Si alloy by laser surface remelting of Al-20 wt.%Si alloy.

It appears from the above-mentioned review that there is an increased interest in the high-silicon content of Al-Si alloys due to their outstanding mechanical properties, especially after the modification. Therefore, to increase the engineering and industrial applications of these alloys,

the size, and the morphology of silicon crystals should be refined to a minimum value. The present investigation is an attempt to use the laser melting and remelting technique, at controlled laser processing parameters, for two purposes. First, to fabricate high silicon Al-Si alloyed layers by laser melting at a fixed laser power density and scan speed. The second is to remelt the produced layers at a fast scan speed with relatively low power levels to refine the silicon phase to a nano sized. The other objective of the study is to measure the nano-indentation hardness in different areas of the eutectic region and correlate the hardness value with the resulting eutectic spacing. The long-term objective of this research is to create a surface layer rich in nano- sized silicon crystals on the aluminum surface, which improves its wear resistance [70].

2.2 In situ and Ex situ Characterization of Laser Processed Materials

Investigations surrounding the formation of plasma within the domain of laser-matter interactions have been a subject of enduring scientific inquiry. When an electron is stimulated, it leaps to a higher energy level or electron layer. When the source of this excitation is removed, it reverts back to its initial state of balance, or equilibrium. During this reversion, any surplus energy is discharged as radio waves, often emanating within the Ultraviolet-Near Infrared (UV-NIR) spectrum for metallic elements. This distinct emission is akin to a unique fingerprint, bespoke to each element and electron at varying energy levels. Optical Emission Spectroscopy (OES) leverages these emissions, interpreting their significance and underlying patterns.

The initial stage of this decoding process involves the recognition and identification of each signal. Research bodies, such as NIST, provide extensive databases to aid other researchers in this signal identification process (https://www.nist.gov/pml/atomic-spectra-database). Once discerned, these signals can be deployed across a host of applications.

Included here is a sample output screen captured from OES, showcasing the spectral range between 320-410nm; courtesy of SenSigma LLC.
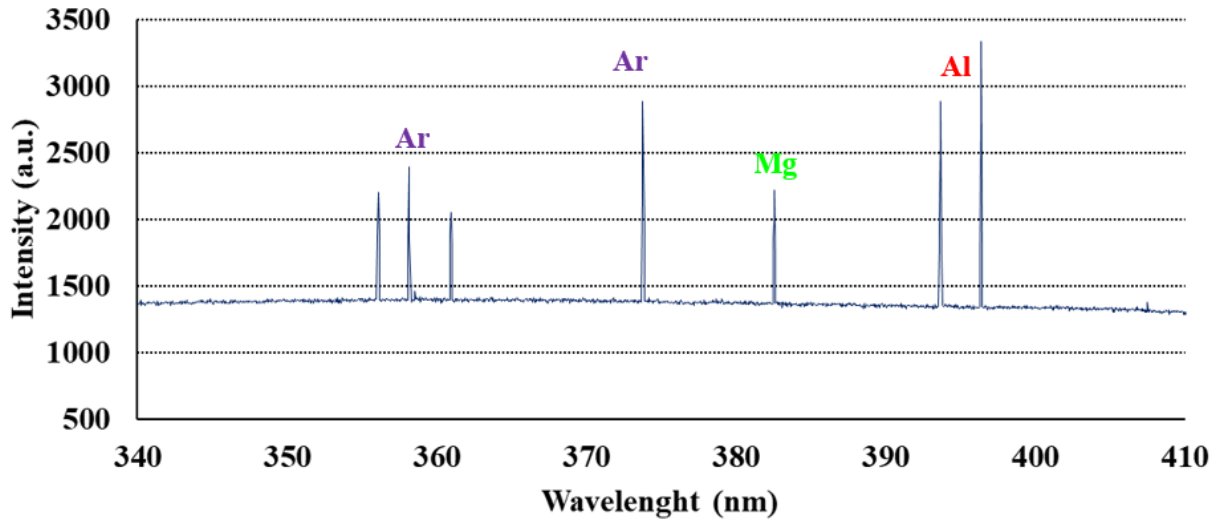
Figure 2.1 Representation of the element's signals captured during laser processing of Al7075. Predictions were based on the pre-defined specific wavelengths of elements from NIST. The horizontal axis shows the wavelengths (320-407nm) and the vertical one shows intensity in arbitrary unit (Courtesy of Sensigma LLC)

In the context of a specific chosen timestep, a signal, characterized by an arbitrary unit, is acquired corresponding to a distinct wavelength. The likelihood of obtaining well over one million data points from a single observation is contingent upon both the spectral and time-associated resolution. Due to this fact, data processing methodologies become significantly consequential in this context, with a few noteworthy illustrations including the Boltzmann plot, line intensity, the line intensity ratio of disparate elements, the linear correlation coefficient to a reference spectrum, principal component analysis, and machine learning tools, reported by Song and Mazumder[71]. These methodologies are typically tailored to meet specific application requirements. Although certain methods may yield results within an acceptable timeframe, others prioritize robustness at the expense of prolonged computation duration.

Screening and setting standardized parameters engender a tolerance for extensive computational duration. Nonetheless, real-time monitoring and in-situ rectification of defects in production systems invariably necessitate either the establishment of pre-defined, acceptable parameter sets, or the development of methodologies intended to expedite the generation of results. This is a critical consideration given the requisite that a production system's response time should not exceed the computation duration.

Song and Mazumder studied the composition analysis of chromium and iron with different mixture ratios at their DMD setup with CO_2 laser. The collected spectra signals were used for establishing a calibration curve. Their 2010 work reports the calibration curve for the above-mentioned elements and their 2012 work takes it one step further: detecting H13 tool steel's deposition and its final Cr percentage[71], [72]. More recently, Wang *et al.* worked on yet another commercial steel, AlSl4140 with Fe/Cr line intensity analyses for composition analysis.

Mazumder *et al.* studied the line intensity ratios for Ti-Fe, Ni-Al, Ni-Ti, Fe-Cr, and Ni-Fe. To get rid of the baseplate's effect, they deposited 5 layers of these mixtures, and the data collection was not started until the beginning of the third layer. While the line intensity ratio for an element is linear with the increasing/decreasing composition ratio, the deviations were observed when there was a phase change. This is important because the final property of the material is also dependent on the phase change. Additionally, phase change may occur within the same composition. So, it could be insensitive to any composition measurement technique in optical emission spectroscopy. [73]

Laser drilling, a processing method using a laser's high energy to vaporize a material in the focal point, also generates plasma and it makes another good candidate for plasma monitoring. Shin *et al.* showed that laser drilling depth and line intensity from Inconel 718 were

inversely proportional. Using the Boltzmann equation, the temperature of the drilling operation is estimated to be around 7700-9200 K degrees [74]. This team also reported a promising 1.6% error in the measurement of Ni composition. Though the results were promising, its applicability is limited to transition elements, that emit. many quality signals to inspect[75].

As stated before, the amount of data that is collected from the process observation is huge and requires a delicate inspection. Comparing A to B, A to C, B to C, … can be challenging as the possible inspection number approaches infinity. When the data output is enormous, tools like machine learning and neural networks gain importance. Huang *et al.* [15] showed an early application of composition measurement. Sun *et al.* [76], on the other hand, proved that one-layer track quality is reflected in the collected spectra signals. Ren and Mazumder[77] used a similar approach and found that the 2D deposition plane's defects and wavelength's intensity are closely related.

SenSigma LLC, an Ann Arbor-based start-up company, has been working on the industrialization of that plasma monitoring system. Their system (SOMS) is able to detect process-related defects and final chemical composition, not only in metal 3D printing but also in the processes that generate plasma such as laser welding, and plasma arc melting.[78] Their application is focused on, but not limited to 7000 series aluminum alloys because of their unique sets of problems(inclusion of volatile elements, susceptibility of tearing, oxidation, etc.) and enormous market potential.

2.3 Direct Metal Deposition of Molds for Wind Turbine Blades using Al6061-RAM2

Proponents of additive manufacturing portrayed it as the third industrial revolution and this claim was substantiated by the esteemed international weekly newspaper, "The Economist",

back in 2012 [79], from the front page. The inherent advantages of this innovative mode of production, including enhanced production flexibility, dispersion of the supply chain, and minimization of waste materials, contribute towards its revolutionary potential. Nonetheless, the realization of its true potential remains impeded by regulatory issues pertaining to scalability, elongated processing durations, and quality assurance hurdles.

Big area additive manufacturing (BAAM), a term used to refer to systems that can create parts in which one dimension exceeds 1 meter, has progressively gained significance, bridging the preexisting limitations in the field of manufacturing. The commencement of BAAM was primarily centered around polymer-based machinery, using materials such as Acrylonitrile Butadiene Styrene (ABS), Polycarbonate (PC), and Polylactic Acid (PLA), due to their relative ease of implementation. Then, researchers working on metal additive manufacturing started to adapt this idea to their technologies. While some of them (like wire-arc additive manufacturing technologist) highlighted their unparalleled build volume per hour with relatively smaller fiscal initial investment costs, others tried to increase the number of laser sources they employ within their machines. The archetype sectors for the integration of BAAM methodologies include, but are not limited to, aerospace engineering, which comprises the construction of space rockets, aircraft bulkheads, and static elements of large-scale turbine engines. Additionally, defense and prototyping for more substantial pieces are also prime candidates, with applications ranging from the manufacture of naval ships and tank hulls, amongst others.

The advent of wind blade turbines, designed to harness kinetic energy from air streams, presents itself as a potential solution for delivering renewable energy to society. This new technique has been drawing interest from both industrial and academic sectors due to its promise of sustainability. However, the ever-increasing dimensions of individual blades, some reaching

heights exceeding 140 meters, pose logistical challenges that impair the growth of the wind blade industry in its quest to meet escalating energy demands.

A potent solution to this issue may lie in modifying the monoblock molds, which could impact two key areas: enhancing mobility and possibly decreasing the size of these blocks. Within a given set of wind blades, some sections are typically shared, which potentially reduces the total number of blocks required. This is due to the ability to use a specific mold module for several different wind blade dimensions.

Our cost-effective strategy for mold manufacture introduces an innovative, intelligently designed family of modular molds. These modules can be transported with ease to produce blades near their on-site locations, bolstering the convenience factor of the process.

Moreover, the implementation of additive manufacturing (AM) facilitates the establishment of conformal thermal management channels. These channels present a flexible platform for tailoring thermal profiles, based on the blade's material constitution. This strategy also allows for an in-situ quality control mechanism during mold production, enhancing mold lifespan, reusability, and throughput time. As a benefit, the cost of mold creation is spread over a larger production volume, offering more substantial returns on investment.

Chapter 3 Laser Surface Remelting of Hypereutectic Aluminum Silicon Alloys

3.1 Laser Surface Remelting of Aluminum Hypereutectic Alloy: Fast Dimensional Estimations and Improved Properties

This article was originally published in ICALEO proceedings 2019 and is planned to be submitted to the Journal of Laser Application with some improvements.

3.1.1 Abstract

Laser surface remelting offers high cooling rates, which makes it a perfect candidate for microstructure refinement. Higher cooling rates also allow for extended solid solubility, moving the eutectic point to higher silicon content. This paper describes how fibrous silicon particles, and the aluminum matrix were refined from the order of microns to nanometers through laser surface remelting. Aluminum spacings were refined more than the silicon fiber diameters. The final composition of the eutectic structure was 17.55 weight percent Si, while the equilibrium eutectic composition is 12.6 % Si (in wt.). Microstructure dimensions in molten zones (hereinafter mentioned as melt pools) were also studied. One specific melt pool was examined under SEM at nearly every 20μm from the surface. A total of 11 micrographs show that silicon fibers are getting bigger with increasing depth. Hardness variation between the base plate and melt pools revealed that the hardness was increased by at least 50%. Melt pool dimensions were also characterized using SEM. Corresponding energy density figures and spectral signals were studied to predict the dimensions in situ, which can significantly reduce characterization time from days to seconds.

Moreover, it is possible to use the obtained data in order to establish a library for the process parameters and resultant dimensions for future experiments.

3.1.2 Introduction

Aluminum (Al) alloys have long been studied for various applications, particularly in the automotive and aerospace industries[6]. The earliest publications on this subject date back to the late 19th century[7]. Al alloys with various content of Silicon (Si) also follow the same trend. Early research focused on hypo-eutectic Al alloys, then, the focus shifted to eutectic and hypereutectic alloys due to their good strength-to-weight ratio, machinability, and remarkable wear resistance[8].

Tenekedjiev *et al.* noted that Si fibers in the Al matrix show characteristics of a composite material. This is one of the few cases in which reinforcing material has less density than matrix, as Al and Si have densities of $2.7gr/cm^3$ and $2.35/cm^3$, respectively. This unique property of Al-Si alloys makes it a good candidate for applications where light-weighting is needed [80] In equilibrium conditions, Al-Si alloys form a eutectic structure at 12.6 Si weight percent[10]. However, non-equilibrium conditions like a very high cooling rate ($10^3 – 10^8$ K/sec), often generated by a laser heat source, may result in a shift of eutectic point toward higher Si composition [11]. With increasing Si content, Al-Si alloys perform better in terms of mechanical properties like fracture toughness, hardness, and tensile strength. However, Si starts to nucleate in a polygonal form once it exceeds a certain threshold, which is also detrimental to the overall mechanical properties. So, a method that combines higher Si content and refinement in the Si particles might enable promising final properties for this alloy system. To that end, we employed laser surface remelting for this study. It has been reported that laser-processed alloys have ultra-fine microstructure, causing high strength, up to five times higher than alloys made by

conventional means [81]. Therefore, high Si content (>12.6 wt.%) Al-Si eutectic structures formed under non-equilibrium conditions may be a good alternative material for industry. Estimating the final dimensions of laser-processed material, in this case melt pool dimensions, with the help of spectral signals is particularly important since it provides us an in-situ results. Conventionally, the processed part needs to be prepared for SEM by mounting, polishing, and etching, then requires relatively expensive equipment as well as a trained user for characterizations. All that process takes around two days. Utilization of spectral signals as a process output reduces this time requirement drastically: to milliseconds. Moreover, the signal can be utilized as feedback for the laser process. Therefore, any desired final shape would be attainable in one step. This work aims to present a correlation between plasma signals and melt pool dimensions.

In this study, Al-20Si (wt. percent) arc-melted alloy was laser re-melted to understand the processing and microstructure relationships in Al-Si eutectics produced under the high cooling rate. Throughout these processes, the plasma signals generated by laser-material interaction were monitored. Optical emission spectral data in the range of 320 to 410 nm were collected as signal output, as this is where most of the metal plasma's emissions occur [13]. Then, these signals were processed via Smart Optical Manufacturing Systems (SOMS) software to characterize the microstructure and estimate the dimensions of the melt pool. Similar studies are available elsewhere[72], [73], [82].

3.1.3 Experimental Procedures

3.1.3.1 Materials Preparation

Arc-melted Al-20Si (wt.) alloy has been supplied from the Ames National Lab. The alloy was cut into small pieces (22.25mm in length, 17 mm in width, and 4.5 mm in thickness) and ground with 1200 grit SiC sandpaper to achieve a mirror-like surface on both faces. In order to increase the cooling rate, the alloy was fixed on top of a copper block using a paste, with a thermal conductivity of 73 W/mK. A disk laser (Trumpf HLD 4002) with a wavelength of 1030 nm was used to re-melt the surface of the material. During laser melting, argon was used as a shielding gas with a flow rate of 60 standard cubic feet per hour. The laser beam diameter was set to 0.6 mm and kept constant for all experiments which were repeated 2 times to be consistent. Other process parameters are given in Table 6. 1.

3.1.3.2 Microstructure Characterization

Microstructures of laser-scanned Al-Si samples were characterized using the Tescan MIRA3 FEG Scanning Electron Microscope (SEM) in secondary electron mode. The Al grains were inspected with electron back-scattered diffraction (EBSD) in the same SEM system. Samples were mounted in an epoxy resin. The mounted samples were ground, polished, and etched (etchant: Keller's Reagent). The composition within the melt pool was also captured in the SEM by utilizing TEAM™ EDS System and TEAM™ software. After capturing the SEM images, an external MATLAB script was used to analyze the minimum, maximum, median, and average sizes of the eutectic structures.

3.1.3.3 Emission Spectroscopy Signals Collection

Plasma induced by laser and material interaction was monitored and collected by a collimating lens. The collimator lens was focused 2 mm above the laser spot and mounted to the laser head (Figure 3.1). These signals were transferred to the SOMS model spectroscope with an

optical fiber cable. The spectroscope has 2048 CCD units and 10 milliseconds (ms) integration time. The spectroscope was connected to a computer and the further processing of these signals was performed.
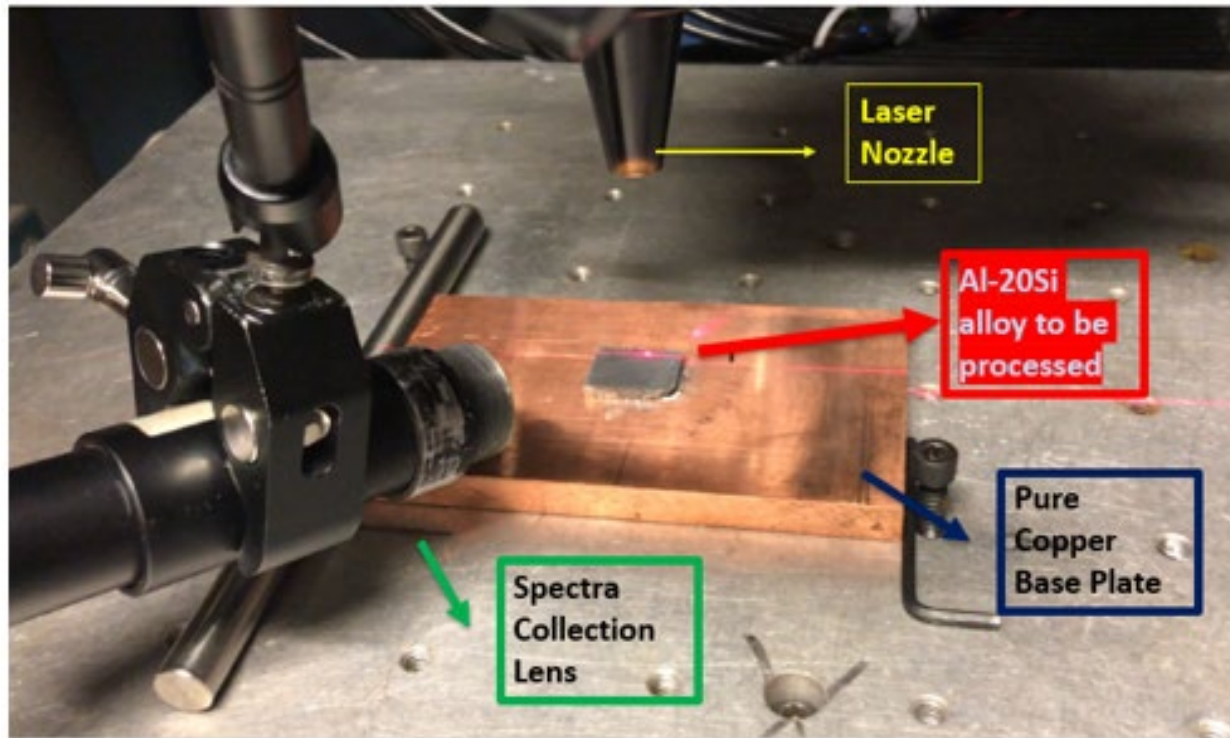
Figure 3.1 Experiment setup for laser processing and spectra signal collection.

Finally, the hardness of the base material and the laser re-melted zone was measured with the help of the Clark digital micro hardness tester (model CM-400AT). Since there was no significant variation in the final hardness under different loads, tests were performed under 25 grams of load to minimize indentation diagonals. The load duration was set to 15 seconds and results were read directly from the instrument.

3.1.4 Results and Discussion

3.1.4.1 Final Microstructure

Figure 3.2 depicts a cross-sectional view of the melt pool obtained in experiment number 5 (0.6 mm laser beam diameter, 1200 W laser power, and 160 mm/s laser scanning speed). The molten pool's semi-elliptical shape can be seen clearly. EBSD analysis of Al grains is also available in the following figure. While the grains are larger in the center of the melt pool, towards the perimeter they get refined. Here, the as-cast region's EBSD result can be disregarded due to high noise.
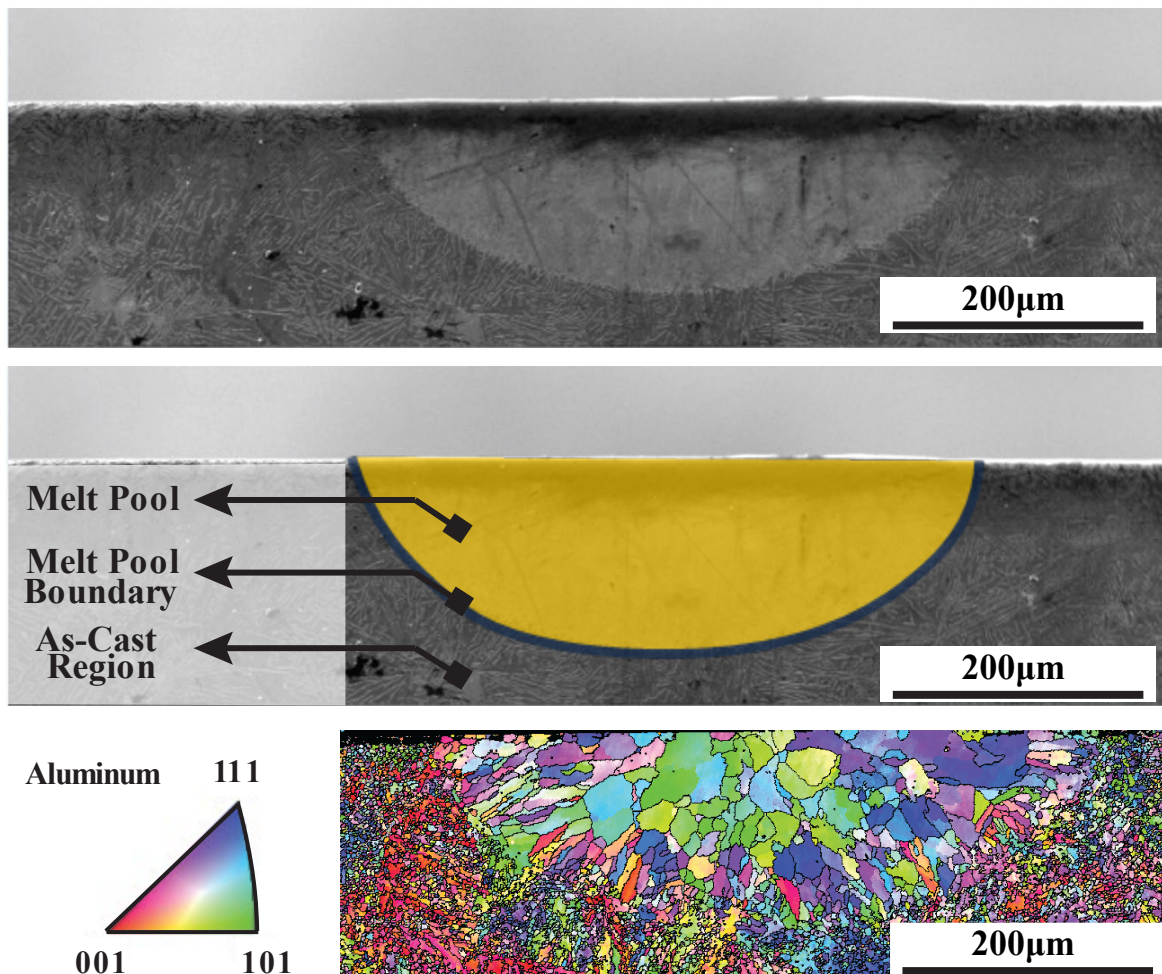
Figure 3.2 Cross-sectional view of the melt pool (Exp. 5) after etching.

To examine the melting and solidifying process more closely, experiment #2 was inspected thoroughly. For ease of characterization, the melt pool was partitioned into 11 different

zones along its depth (Figure 3.3). The image numbers and their depth values can be seen in

Table 3.1.
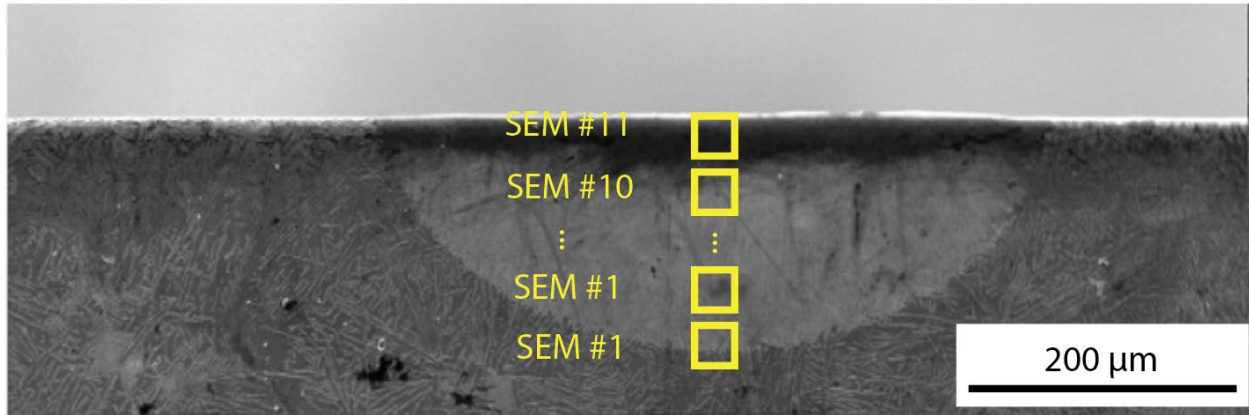
Figure 3.3 The melt pool of experiment #2 is divided into 11 zones. The depth of SEM #11 and SEM #1 were 19.45 µm and 213.95 µm, respectively.

While the as-cast zone contains acicular (needle-like) silicon in brighter tones, those

features are not available inside the melt pool as shown in more detail in Figure 3.4. In Figure

3.4, the transition zone between the boundaries of the molten zone and the unprocessed section

(as-cast alloy) is highlighted with a dashed line. Outside of the melt zone, silicon structures are

present on the order of 10 µm. However, much finer silicon structures in a fibrous eutectic form

in the melt pool are no bigger than 150 nm in diameter. Eutectic Al-Si zone and Al dendrites

(possibly containing Si precipitates[83]) were observed as well.
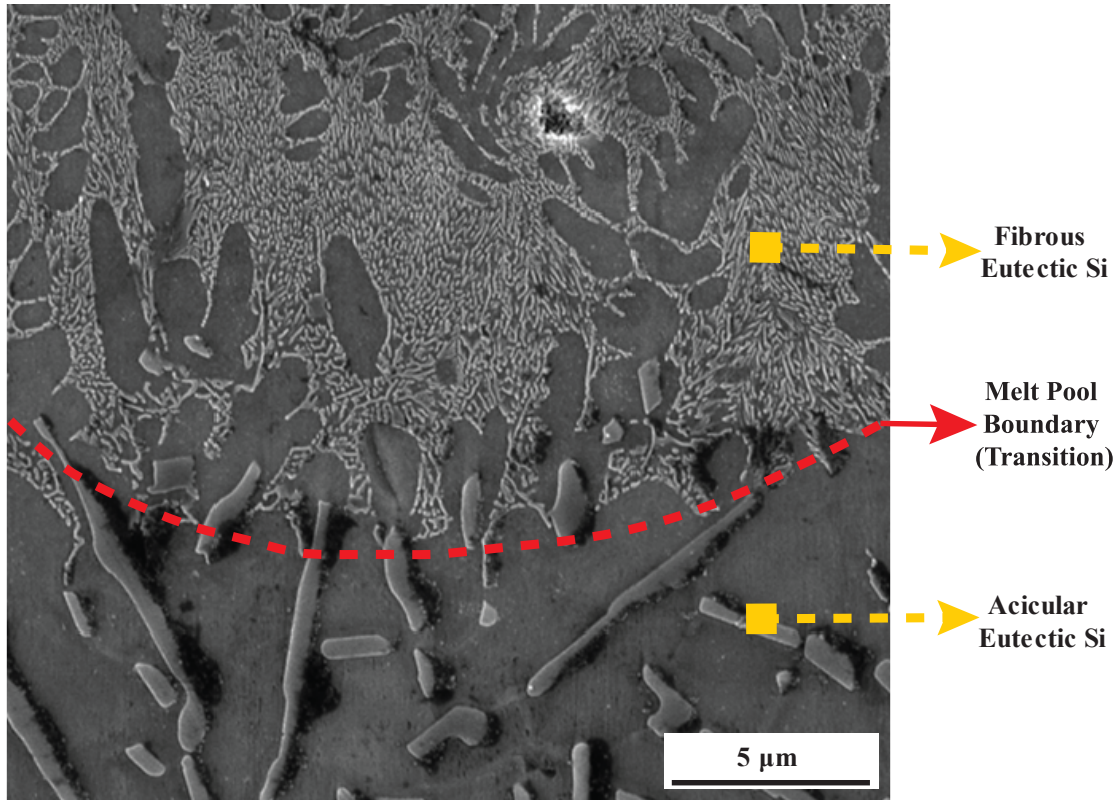
Figure 3.4 SEM image #1 shows the transition zone between the melt pool and the as-cast section of Al-Si alloy clearly. Different morphologies of eutectic Si are also illustrated as fibrous and acicular.

An external image processing script further analyzed the Al spacings and Si fiber diameters in the captured SEM images (1 to 11). The results of these calculations are listed in Table 6. 2 and Table 6. 3, for Al and Si, respectively.

3.1.4.2 Microstructure Refinement with Laser Remelting

It is apparent that Si fiber diameter and Al spacing between these have been reduced significantly after laser processing. This phenomenon can be attributed to heat history within the melt pool. As the solidification time decreases (or the cooling rate increases), there is less time for particles to nucleate. When these microstructure dimensions are studied further, it is possible to establish a relationship between depth from the surface and microstructure size due to the

cooling rate effect [84]. Figure 3.5 shows such a relationship. Here, the cooling rate was calculated using Rosenthal's equation given in Equation 3.2.
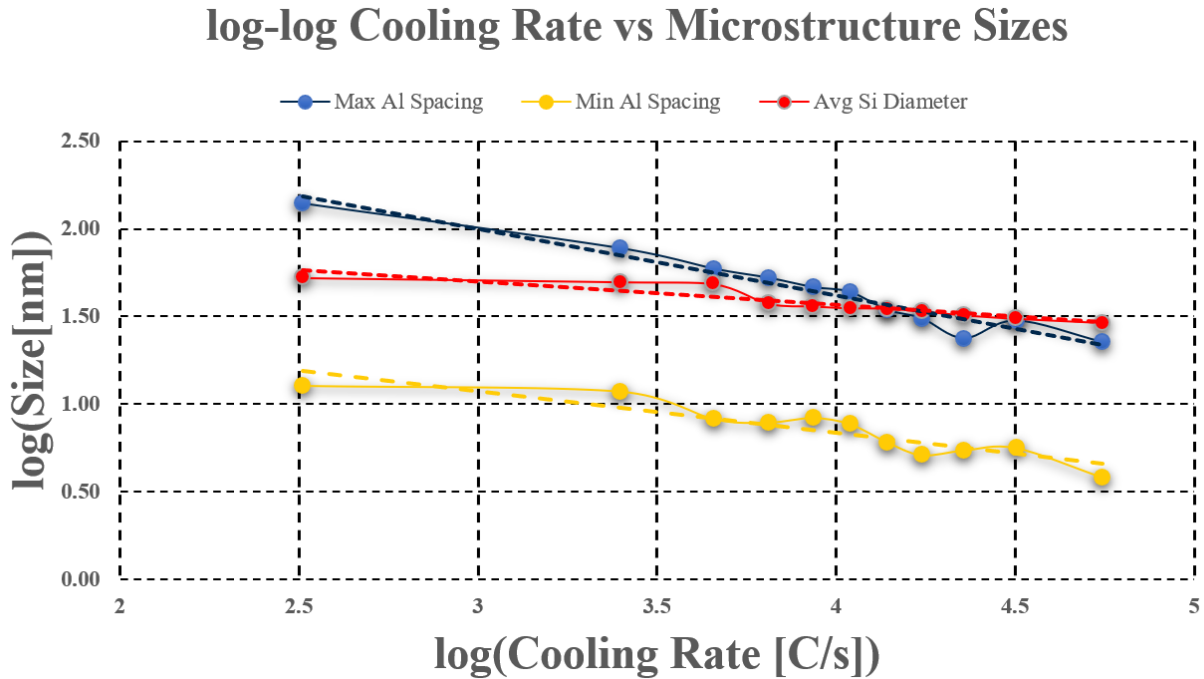
Figure 3.5 The relationship between CR and microstructure size on a logarithmic scale. Dashed lines indicate trendlines.

Although the statistics do not show a meaningful connection generally, in two points, this correlation is obvious: Mean Si fiber diameters with respect to depth, and maximum and minimum Al spacing, which can be seen in Figure 3.6. The curve-fitting equations and their corresponding R^2 values are given below:

- Max Al Spacing: $0.613x + 0.426$ ($R^2 = 0.71$)

- Min Al Spacing: $0.439x - 0.018$ ($R^2 = 0.82$)

- Avg Si Diameter: $0.231x + 1.116$ ($R^2 = 0.74$)

where x equals the logarithm of Depth (μm) to the base of 10.

Microstructure Size vs Depth
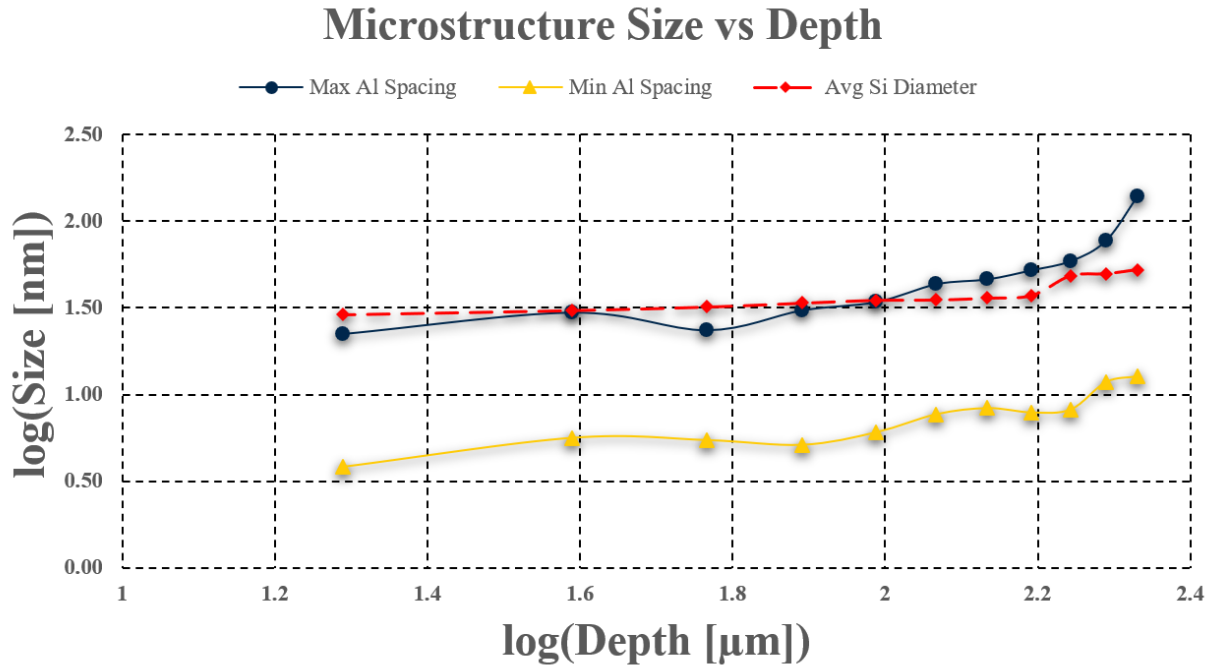
Figure 3.6 Microstructure size changes with changing depth. As depth increases, microstructures tend to be larger.

As Mazumder *et al.* studied, it was proved that microstructural refinement results in much greater material strength. While as-cast Al-33.2Cu (weight percent) alloy has 200-400 MPa yield strength, it rises up to 1100 MPa after laser processing[81]. While further studies are necessary to find out the compressive and/or tensile behavior of the laser-remelted Al-20Si, an increment in mechanical response is expected for our studies. These were reported in the literature [85], but the nano-mechanical response is pretty much dependent on the location from which the test specimen is prepared. It can be within a particular nano-eutectic colony, poly-crystalline nano-eutectics, or heterogeneous structure of Al dendrites and fibrinous Si eutectics.

3.1.4.3 Melt Pool Dimensions

The conducted experiments and their resultant melt pool sizes are presented in Table 3.1.

Table 3.1 Experiment numbers and corresponding melt pool dimensions in terms of with, depth, and ratio

Experiment Number	Energy Density (Joule / mm³)	Melt Pool Width (μm)	Melt Pool Depth (μm)	Melt Pool Ratio (Width / Depth)
1	2.934	689.07	277.15	2.49
2	1.467	600.27	214.52	2.80
3	0.978	556.59	189.19	2.94
4	0.734	540.78	179.77	3.01
5	0.550	501.90	156.03	3.22
6	0.489	482.44	146.33	3.30
7	1.834	636.75	236.34	2.69

Energy density for this table was calculated by means of Equation 3.1:

$$\frac{Power\ [W]}{Area\ x\ Scanning\ Sped\ [mm^3/s]}$$

(3.1)

There has been a strong correlation between energy density and melt pool dimensions (width and depth) when power inputs are similar. These relations are proven by very high R^2 values with the given power regression equations, both of them are greater than 99%.

| A | Melt Pool Width vs Energy Density | B | Melt Pool Depth vs Energy Density |
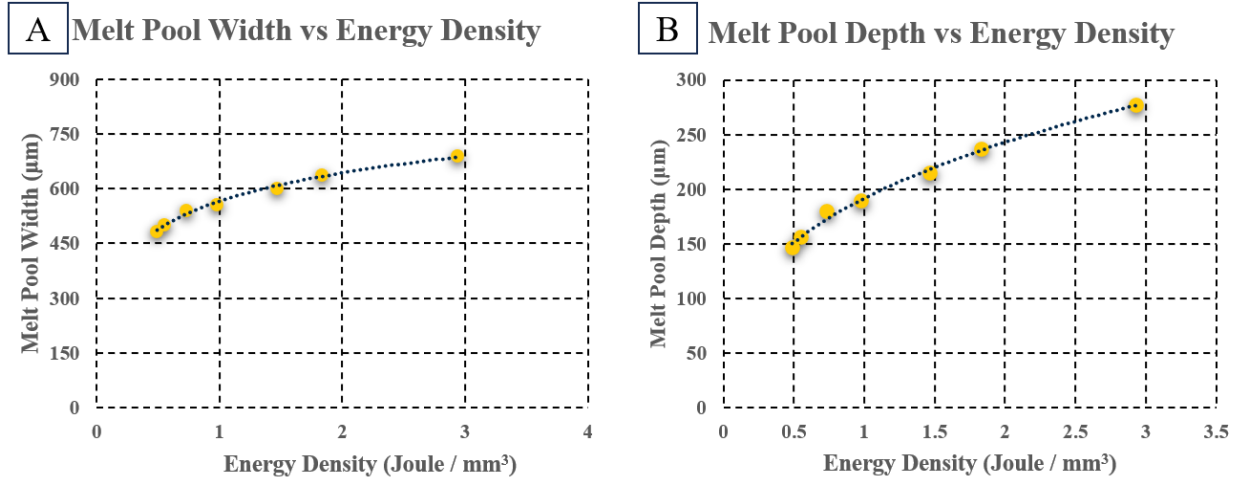
Figure 3.7 Regression fitting equations for the given data a) $561.95x^{0.193}$ and b) $191.5x^{0.3425}$

The regression analysis for the depth and width dimensions as a function of energy density results in high R^2 values. This information can be used for estimating the radius of the melt pool for the given material and has the potential to be expanded to other metal alloys. Rosenthal proposed this equation for simple estimation of melt pool dimension:

$$T - T_0 = \frac{\varepsilon q}{2\pi K} \exp\left[\frac{-v}{2\ \alpha}\ \xi\right] \cdot \frac{1}{R} \exp\left[\frac{-v}{2a}R\right] \tag{3.2}$$

where $R = (\ (half\ width)^2 + depth^2\ )^{0.5}$

Therefore, R (radius) can be expressed as a function of absorptivity, power, thermal conductivity, scanning speed, thermal diffusivity, and the temperature domain. This equation requires a numerical solution for R since it is primarily determined by width and depth. Instead, the equation from the regression fit in Figure 3.7 can be used for the R, thereby reducing the time for computation.

$$R' = \frac{\varepsilon * Q}{2 * \pi * K} \frac{1}{T - T_0} \exp[C * \xi] * \exp[C * R] \tag{3.3}$$

$$R = \sqrt{[(280.975x^{0.193})^2 + (191.5x^{0.3425})^2} * 10^{-6} \tag{3.4}$$

$$where, x \; is \; the \; energy \; density \left(\frac{J}{mm^3}\right) and \; C = -\frac{v}{2a}$$

Melt Pool Radius vs Energy Density
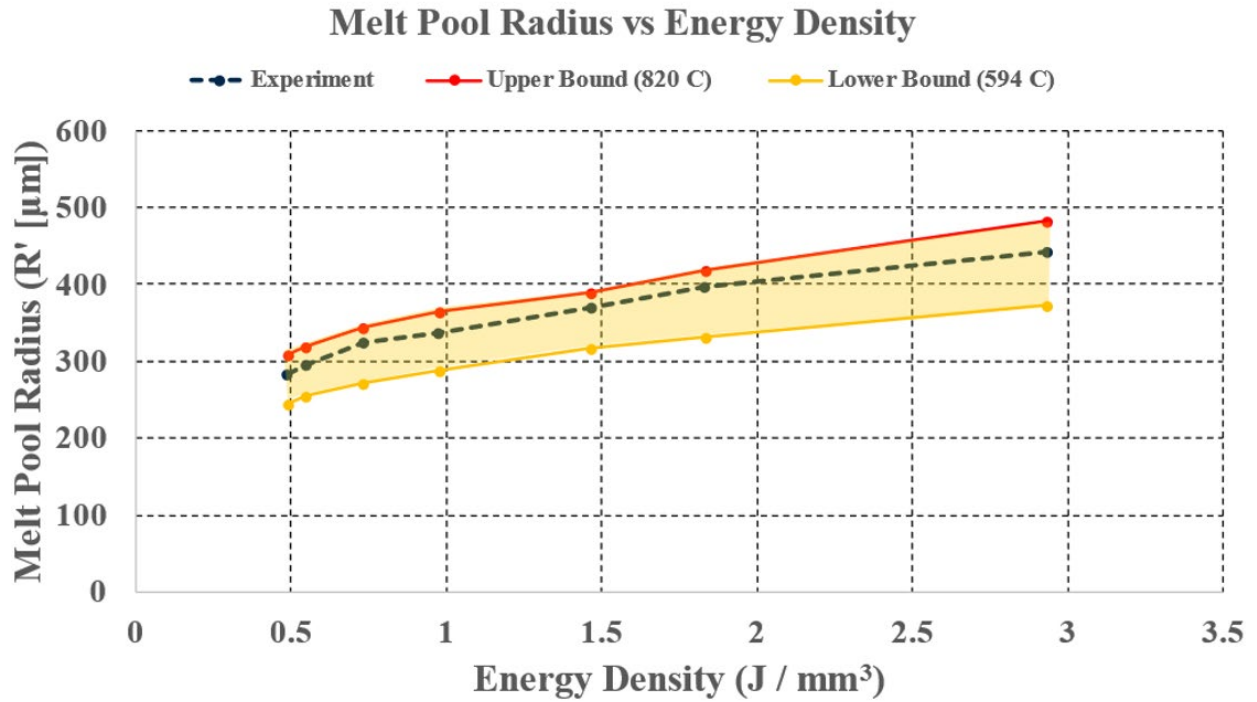
Figure 3.8 Radius changes with respect to energy density. It remains within the area of estimation.

Energy input and plasma intensity are reported to be proportional to plasma intensity calculated by the population of atoms in the upper state[72]. Therefore, having a closer look at melt pool dimensions (as they are almost perfectly correlated to energy density, shown in Figure 3.7 and spectral data may reveal a good connection. Also, it is worth noting that the cross-

sectional view inspected in the characterization of the melt pool in this study was captured from the beginning of laser-material interaction. While the total length of the scanned zone was 22.25mm, the cross-sectional SEM photo was obtained around 0.5mm and 1mm from the beginning. Thus, plasma signals from the first five frames (namely 0 - 50 ms) should be taken into account. The following figure (Figure 3.9) also shows the data and the regression fit.
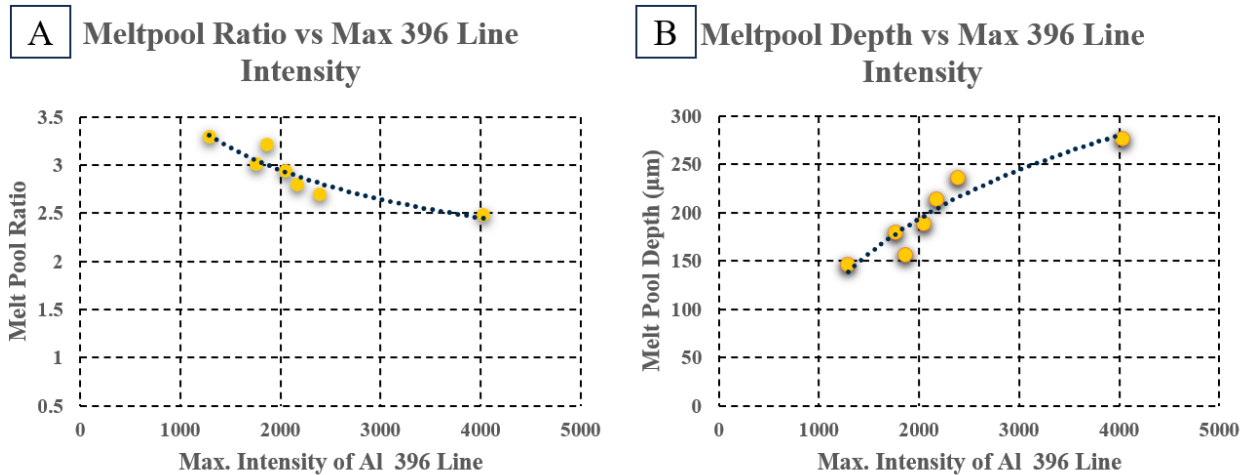
Figure 3.9 Both data are fitted into logarithmic regression equations, and these are like; a) $-0.759\ln(x) + 8.7269$ b) $124.89\ln(x) - 755.58$ and their R^2 values are 0.850 and 0.884, respectively. The melt pool ratio is defined as the ratio of width to depth of the melt pool.

To elaborate further, it looks like the plasma intensity from the process can be used to estimate the melt pool depth. Knowing the melt pool depth, the melt pool width can also be found as they are shown in good agreement. With that, the total laser-treated area can be projected in a matter of seconds. By just looking at the spectral responses from processes, a user has a chance to adjust the processing parameters (hatching, etc.) during the operation.

In the fully eutectic region, the composition was measured at around 17.55% Si (in wt.) for the melt pool of experiment #2. In equilibrium, the Al-Si binary system is expected to form a eutectic solidification at around 12.6Si weight percent. In this study, this has been found to be higher. As per the motivation of this work, an increment in the Si fraction within Alloy is

36

desirable due to its mechanical strength contribution. Moreover, this increment in the Si did not result in a big chuck of Si particles, which is also known for its detrimental effect on crack propagation. Achieving both objectives is possible with our laser surface remelting experiments. This is also in agreement with the microstructure size findings; having less Al spacing might result in a higher composition of Si alloy compared to the equilibrium eutectic composition. The electron dispersive x-ray spectroscopy (EDS) result can be seen in the following Figure 3.10.

Lsec: 50.0   10 Cnts   11.400 keV   Det: Octane Plus

Element	Weight %	Atomic %	Net Int.	Error %	Kratio	Z	A	F
AlK	82.45	83.02	4716.58	1.41	0.8161	0.9963	0.9914	1.0023
SiK	17.55	16.98	453.67	7.37	0.0817	1.0177	0.4576	1.0002

Figure 3.10 The EDS results from the eutectic region. Si content can be seen clearly as 17.55% (in wt).

The hardness of the material was measured for all experiments as well as the base material. In Figure 3.11, the first column from the left indicates the base material. It is apparent that laser surface remelting has increased the hardness by at least 50 %. Using DMD, Dinda *et al*. have reported that an ultrafine eutectic zone resulted in 108.2 HV [86]. In general, laser processing of Al-Si alloy seems to return a harder final material. This study demonstrates better refinement in the microstructure than laser additive manufacturing. Due to this fact, the Hall-patch effect contributes to the final mechanical property. It is also worth noting that the ultrafine

fully eutectic region within the melt pool resulted in a higher hardness value compared to the other sections. Therefore, further analyzing the material under nano mechanical testings (indentations, compression, or tensile), where the eutectic region can be selected more precisely, may reveal interesting results.

Hardness Variation Between Samples
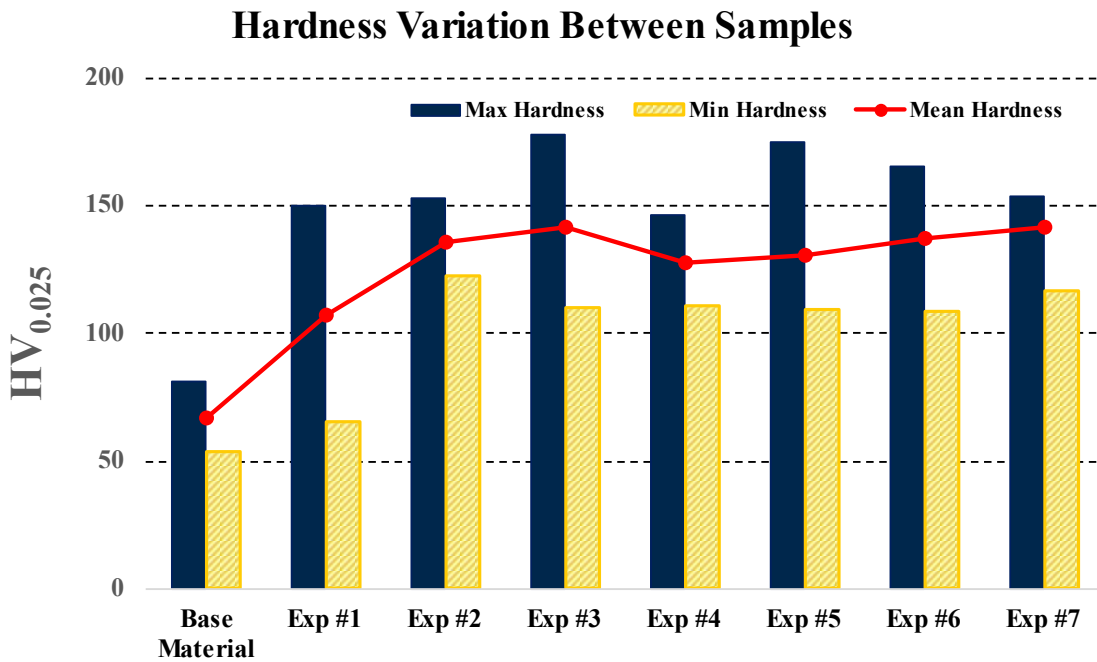
Figure 3.11 The change in the hardness as a result of laser surface remelting.

3.1.5 Conclusions

In the present study, it has been shown that there is a strong correlation between Al and Si microstructure size and their relative depth with respect to the surface of the melt pool.

- As the distance from the surface increases, the dimensions of the microstructure also increase. That implies the cooling rate on the surface is highest since it is the driving factor for microstructure formation.

- The composition of experiment #2 in the eutectic zone was found 17.55% Si in weight percent, which was thought to be a result of Al spacing refinement.

- Refinement in the Al-Si alloy microstructures increased the hardness significantly, up to two-fold.

- Melt pool dimensions and energy density showed an almost perfect relationship as the trend of their regression equations have R^2 value greater than 99%. Those measured dimensions can help calculate the new melt pool dimensions for any material, based on their thermo-physical properties and process conditions.

- Due to the nature of emission spectroscopy, an increase in the input energy (in this context, energy density) results in a considerable increase in the intensity of spectral emission. The relationship between melt pool dimensions and 396nm wavelength spectral intensity (x) is approximated with the following equations:

  - Melt Pool Width to Depth Ratio $= -0.759\ln(x) + 8.7269$ (R^2: 0.850)
  - Melt Pool Depth (μm) $= 124.89\ln(x) - 755.58$ (R^2: 0.884)

  Therefore, the relationship between the melt pool dimensions and spectral intensity could be easily used for real-time dimension prediction.

3.2 Effect of Cooling Rate on Nano-Eutectic Formation in Laser Surface Remelted and Rare Earth Modified Hypereutectic Al-20Si Alloys

3.2.1 Abstract

Laser Surface Remelting (LSR) was applied to arc-melted Al-20Si-0.2Sr, Al-20Si-0.2Ce, and Al-20Si hypereutectic alloys to refine microstructures. Experiments revealed that microstructures in the melt pool varied from fully eutectic to a mixture of Al dendrites and inter-dendritic eutectic. We calculated cooling rates using the Eagar-Tsai model and correlated cooling rates with characteristic microstructures, revealing that cooling rate on the order of 10^4 K/s could lead to maximized fully eutectic microstructure morphology. Due to rapid solidification, the Si composition in the LSR eutectic was measured at 18.2 wt. %, higher than the equilibrium eutectic composition of 12.6 wt. %Si. As compared to Al-20Si, Ce addition had no significant effect on the volume fraction of the fully eutectic structure but refined Si fibers to approximately 30 nm in diameter. Sr addition did not further refine the diameter of eutectic Si fibers as compared to Al-20Si but increased the volume fraction of the fully eutectic microstructure morphology. The refinement ratio (φ) of the Si fiber diameter from the bottom of the melt pool to the surface for the three alloys is similar, around 28%. The established correlation between the cooling rate and the size and morphology of the microstructure within the melt pool will enable tailoring of the microstructure in laser processed as well as deposited alloys for high strength and plasticity.

3.2.2 Introduction

Aluminum (Al) and Silicon (Si) are the 2nd and 3rd most abundant elements in the Earth's crust[17]. Still, these elements lag behind steel in terms of production and use due to steel's unmatched strength and cost-effectiveness. However, there has been an effort to switch from steels to Al alloys[18] for structural [19] and tribological applications[20]. The higher strength-to-weight ratio of Al-Si alloys makes it a good candidate for industries interested in lightweighting[21]. In addition, Al-Si alloys exhibit good weldability, castability, corrosion resistance, wear resistance, and high thermal conductivity [22], and Al-Si alloys promise good recyclability. To fully take advantage of the harder Si phase, more attention was gradually moved from hypo-eutectic (<12.6 wt.% Si) to hypereutectic Al-Si alloys[23], [24]. However, Si tends to nucleate as large flakes in hypereutectic Al-Si alloys, significantly increasing the propensity for crack formation. Therefore, methods to refine and control the morphology and distribution of Si in Al-Si alloys are an area of active investigation.

Many ways have been developed to refine primary and eutectic Si particles. For conventional casting, refinement starts with stirring of the alloy melt, originally done mechanically and nowadays performed electromagnetically[25] or via ultrasonic treatment[26]. Chemical modification of the molten liquid has been examined to hinder Si segregation, by the addition of Na [27], [28]and P[29], [30]. Likewise, chemical modification by rare earth elements microalloying is studied for Ce[31], [32], Sr[33], Y[34], La [35], Eu[36], [37], Yb[38] and Nd [39]. Chemical modification often leads to thermodynamically favorable phases other than primary Silicon, thereby reducing the degree of Si segregation. However, the excess addition of rare earth elements leads to the formation of intermetallic phases that can be detrimental to the ductility and toughness of the alloy [40]. Melt spinning [41], thin film deposition [42], and gas

atomization[43] have also been used for micro to nanoscale research and applications for refined Si phases. Another method for Al-Si alloy refinement is laser surface remelting (LSR)[44]–[46]. The technique involves scanning a high-power laser across a polished surface. The laser quickly heats the surface of the alloy above the liquidus temperature, forming a shallow melt pool. Due to the high thermal conductivity of the Al alloy and fast laser scan speed, the trailing end of the melt pool solidifies with estimated cooling rates up to 10^6 K/s [47]. If excimer lasers are used, cooling rates estimated from measured cell spacing could be up to 10^9 K/s [48]. Cooling rates are dependent on many process parameters such as laser power and laser scanning speed. There has been research on chemical, mechanical, and high energy beam (laser or electron beam) modifications as well as their combination[49].

Although LSR leads to microstructure refinement, the microstructure within the melt pool can vary from fully eutectic to hypoeutectic (mixture of primary Al dendrite and eutectic) with fine Si precipitates eventually forming in the Al dendrites[50]. In this work, the effect of LSR process parameters and rare earth elements, Cerium (Ce) and Strontium (Sr), on the microstructure in the melt pool of Al-20Si alloys was studied, in particular, to correlate the cooling rate with the microstructure, specifically with the volume fraction of the fully eutectic regions in the melt pool as well as the size of eutectic Si particles. This combinatory effect of LSR and rare earth element alloying of Ce or Sr has not been investigated in prior literature, and is not correlated quantitatively with the cooling rate. For LSR, the laser power was varied in a range that caused melting within a thin layer at the surface. The cooling rates for these experiments were estimated using the Eagar-Tsai model[51] with backward-fitting. A correlation between the cooling rate and the size and morphology (eutectic versus hypoeutectic) of the

microstructure within the melt pool will enable the tailoring of the microstructure in laser-processed and printed alloys for high strength and plasticity.

3.2.3 Materials and Methods

Arc-melted Al-20Si, Al-20Si-0.2 wt.% Sr, and Al-20Si-0.2 wt.% Ce alloys were procured from the Materials Preparation Center, Ames National Lab. The compositions of as-received alloys were verified via energy-dispersive X-ray spectroscopy (EDS) in a Scanning Electron Microscope (SEM). Small rectangular blocks, 4 mm thick and 20 mm long, were cut for LSR. The top and bottom surfaces of these blocks were polished to 3 μm surface roughness to ensure consistent melt pool geometry during LSR. The samples were affixed to a commercially pure copper heat sink with thermal paste (73 W/mK) to enhance the heat transfer rate. The top surfaces of the blocks were not coated with absorbent material in order to mitigate the formation of extraneous phases and to make this approach leaner for future applications.

LSR parameters were selected to encompass a large range of power densities. For this reason, Taguchi's method of experimental design was followed. With that, easy comparison of analyzed outputs such as the area of fully eutectic regions, the area fraction of fully eutectic regions relative to the whole melt pool, melt pool width, melt pool depth, and cooling rates of the processed material were achieved. Laser beam diameter ranged from 0.4 mm to 2 mm, laser scan speed ranged from 25.4 mm/s to 177.8 mm/s and laser power was varied from 175 W to 3000 W (Figure 3.12). The lowest laser power just melts the surface of the samples while the highest laser power is close to the laser cutting threshold. The full list of LSR experimental parameters in Taguchi method format is shown in Table 6. 4. As we have three alloys and eighteen sets of LSR parameters, a total of 54 samples will be tested in the initial assay. The laser used in this study is Trumpf HLD 4002 Disk laser (Yb:YAG) with 1030 nm wavelength.
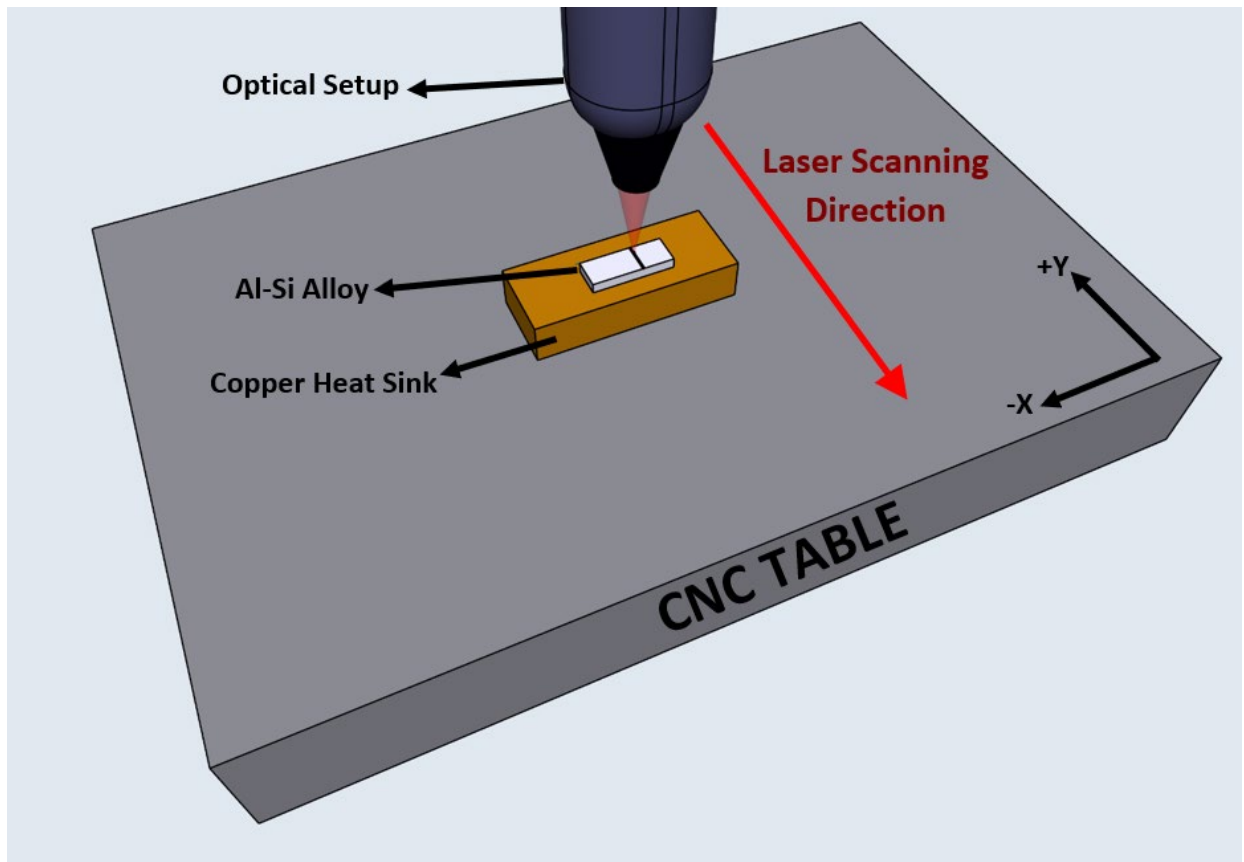
Figure 3.12 Schematic of the experiment setup.

Post LSR, the samples were polished and characterized using SEM (Tescan MIRA3) and EDS (TeamTM). SEM characterization was used to measure the diameter and spacing of silicon fibers and measure corresponding microstructure morphologies within the melt pool. Figure 3.13 shows an example. Within the melt pool (a), the SEM-observed microstructure can be primary Al + eutectic (b) or fully eutectic with nano-fibrous Si (c), even though the nominal composition corresponds to hypereutectic based on an equilibrium phase diagram. Outside of the melt pool, the coarse Si flake eutectic morphology (a and d) is observed with isolated primary Si particles. However, for this study, refinements in the primary Si particles were not taken into account. (e) and (f) schematically show the observed distributions of different microstructure morphologies. In an effort to correlate the cooling rate with a given microstructure morphology, the area

fraction of fully regular eutectic colonies in the melt pool was measured. For consistency, only the prominent fully regular eutectic colonies (arbitrarily defined as greater than 5 µm by 5 µm) were considered in the measurement of fully regular eutectic morphology fraction within the melt pool. In addition to the microstructure, compositions of specific areas were also collected via EDS (20 kV) after the identification of the microstructures of interest.
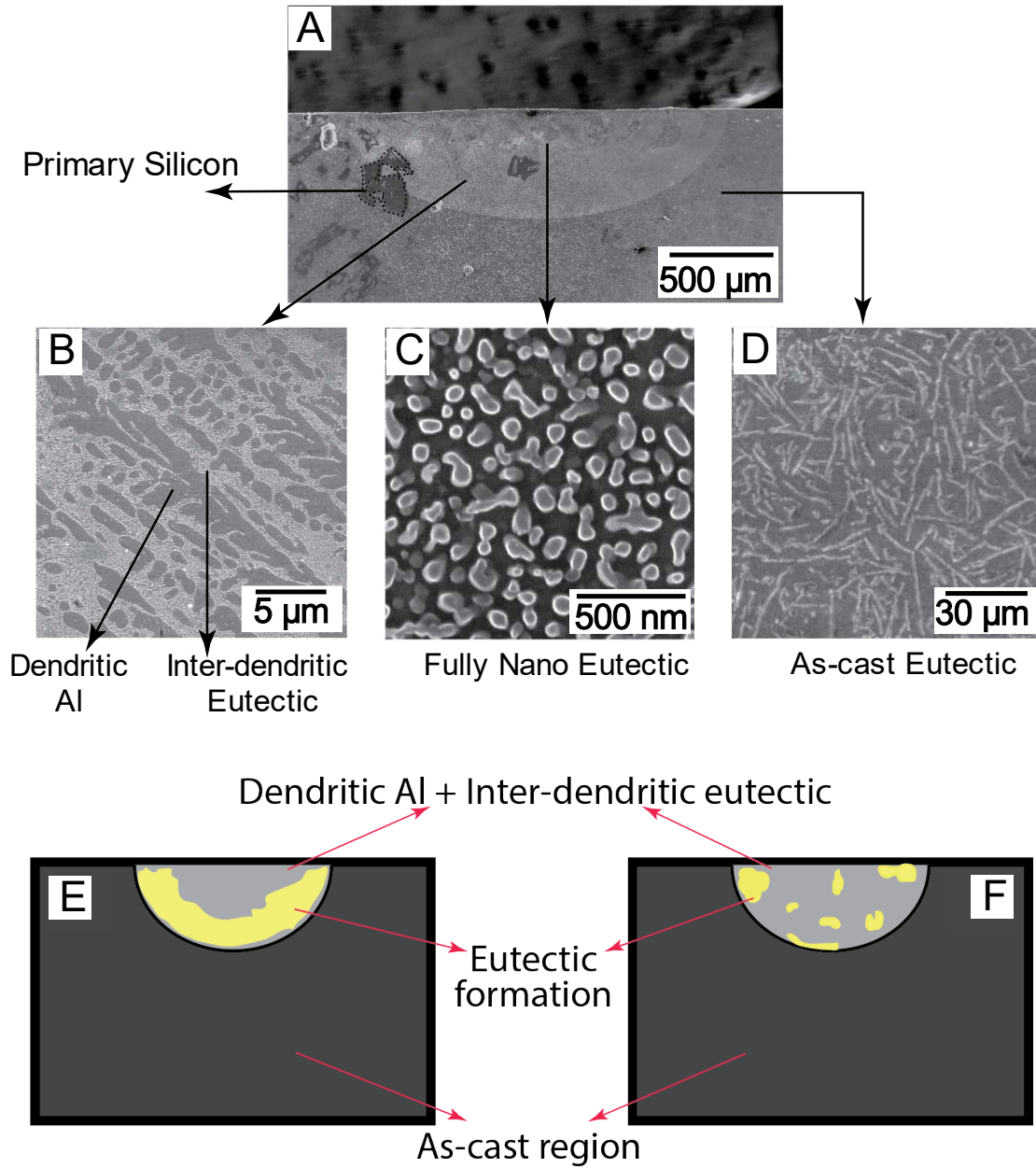
Figure 3.13 Microstructures of LSR Al-20Si alloys under SEM (A) and a schematic. The microstructure quantification reported corresponds to (B): Al dendrite formation and interdendritic eutectic structure with fibrous Si in the LSR region. (C): Fully eutectic colony within LSR region, with fibrous Si. (D): As-cast flake eutectic. Schematic of the eutectic structures observed within the melt pools. (E) continuous and discernable fully eutectic regions; (F) random, inter-dendritic eutectic regions within primary Al dendrites with pockets of fully eutectic regions.

After measuring and identifying the set of LSR parameters that yield the highest fully eutectic area relative to the whole melt pool, the second set of samples was made to verify

whether the results were representative and reproducible. The additional samples were also characterized in different cross-sections along the scanning path (shown schematically in Figure 3.14 a-b) to examine whether the eutectic formation is stable and consistent along the entire path.
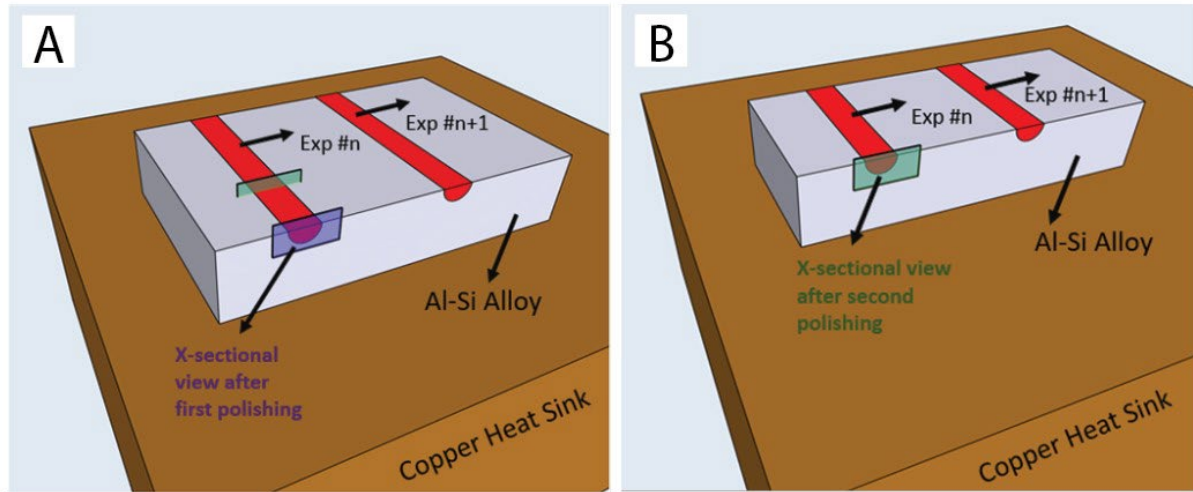
Figure 3.14 Schematic illustration of the cross-sectional microstructure characterization of the melt pools. Here the purple plane (A) was characterized first, and then the block was ground again and polished to get the green surface (B). The approximate distance between the purple and green plane is 100 μm.

3.2.4 Results and Discussion

3.2.4.1 Eutectic area within the melt pool

Table 6. 5 in the Appendix gives the fully eutectic area percentages for all eighteen sets of LSR parameters for each Al-20Si alloy. Those results are summarized in Table 3.2 below. LSR parameter sets 1, 2, 3, 11, 17, and 18 were identified as those with the highest eutectic area percentages. Those experiments were then repeated three additional times with each sample sectioned and characterized two times. This resulted in 6 additional characterizations per Al-20Si alloy for each repeated LSR parameter set. The results of these additional characterizations as well as the originals are displayed in Figure 3.15

Table 3.2 Summary of eutectic formation for the initial set of LSR experiments. The Al-20Si-0.2Ce samples has noticeably lower eutectic area percentages compared to Al-20Si-0.2Sr and Al-20Si.

Laser Spot Diameter (in mm)	Average Fully Eutectic Area Percentage for Al-20Si-0.2Sr	Average Fully Eutectic Area Percentage for Al-20Si-0.2Ce	Average Fully Eutectic Percentage for Al-20Si
0.4	24.93%	7.60%	17.62%
2	16.21%	14.06%	20.83%
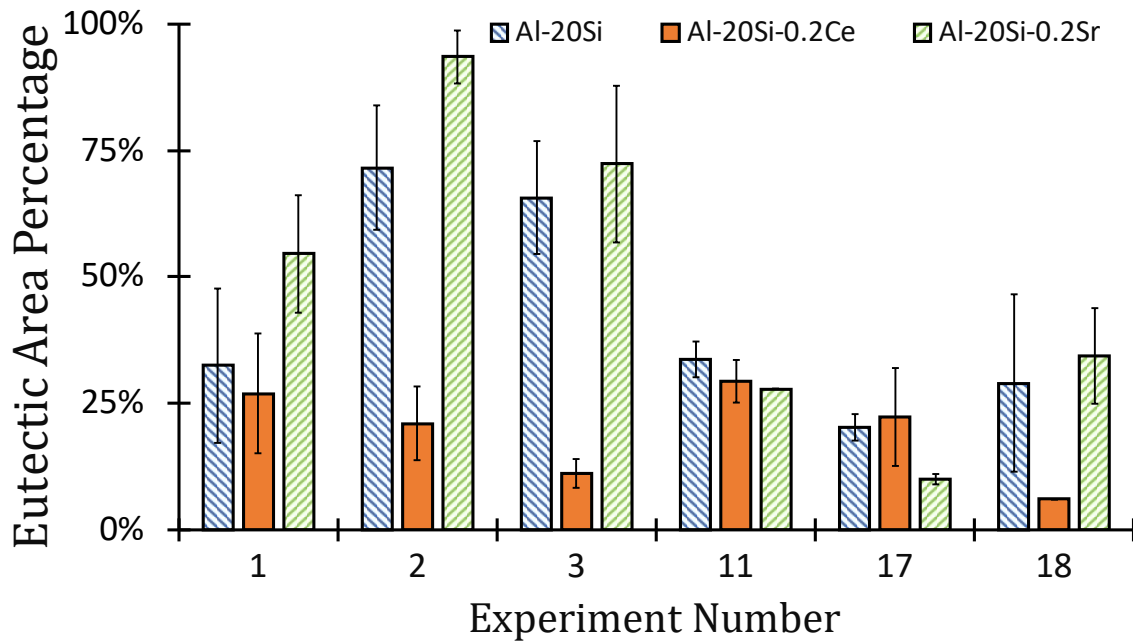
Figure 3.15 Summary of Eutectic Formation Percentage. Errors are represented in 1 standard deviation.

As can be seen in Figure 3.15, Ce addition on average results in a lower amount of eutectic area formation compared to Al-20Si and Al-20Si-0.2Sr. SEM characterization of the Al-20Si-0.2Ce samples shows an abundance of Al dendrites and implies that Ce micro-alloying enhances the extent of hypo-eutectic microstructure in the hypereutectic composition alloy

(Figure 3.16). Therefore, a future study of Al-Si-0.2Ce alloys with higher Si content could prove
fruitful.
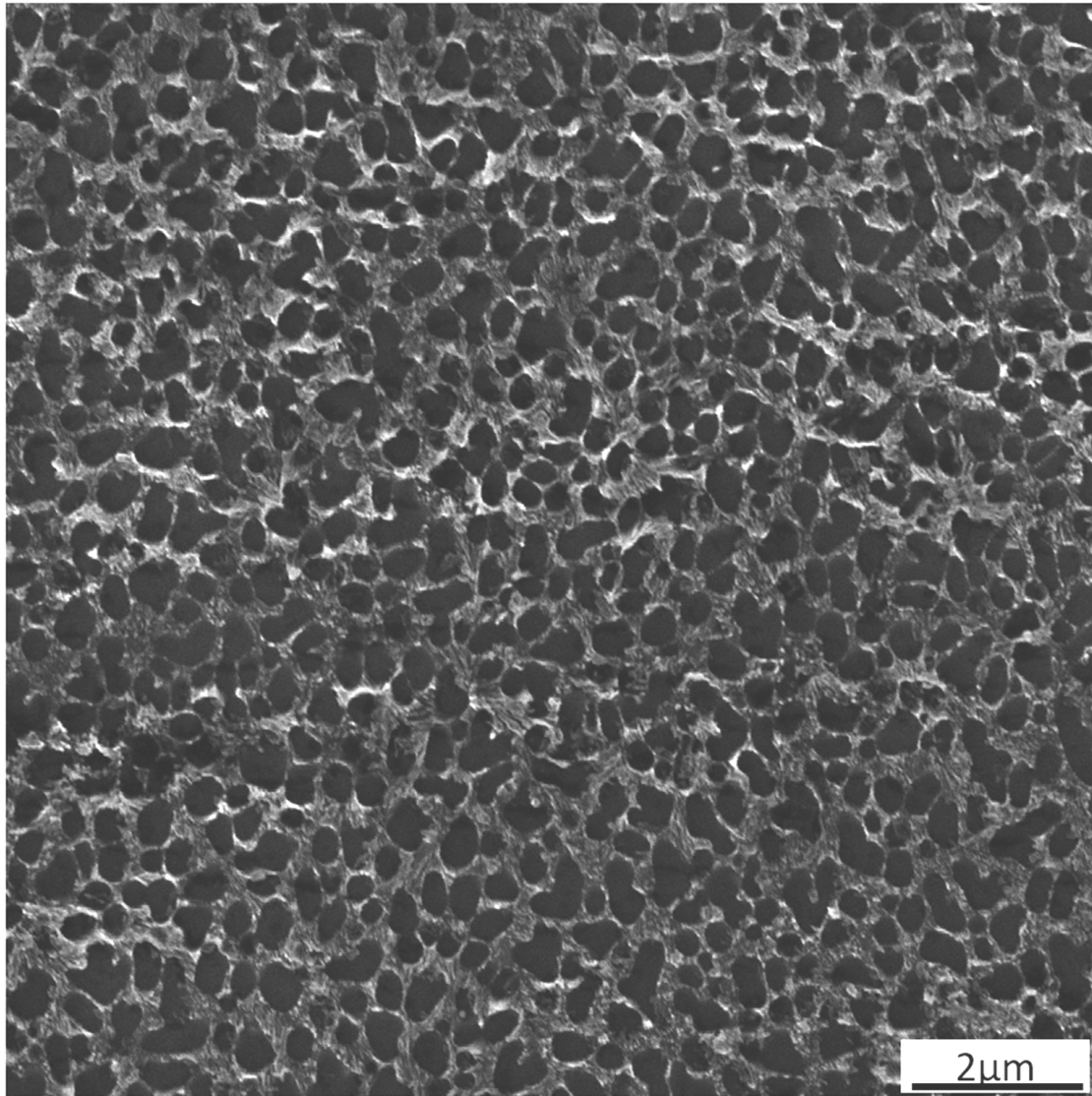
Figure 3.16 Hypoeutectic-like dendritic and interdendritic eutectic structure from Experiment #5 with Ce addition.

The EDS measurement of LSR parameter set 1 applied to Al-20Si, showed
approximately 18.2 wt. % Si within the eutectic region at the peripheral of the melt pool. It is
measured at 15.9% Si for Al-20Si-0.2Ce and 17.5% for Al-20Si-0.1Sr. Under equilibrium
cooling conditions, the Al-Si eutectic structure should be 12.6 wt. % Si. The measured Si

concentration in the eutectic structure indicates that the cooling rates achieved by LSR lead to substantial coupled zone growth driven by large undercooling[5]. As such, LSR allows for the synthesis of Al-Si eutectic structures supersaturated in Si and beyond that achievable by conventional means. While the 11th, 17th, and 18th LSR parameter set experiments show lower eutectic area formation compared to that of the 1st, 2nd, and 3rd, this is due to the former being processed with larger beam diameters (see Table 6. 5)

3.2.4.2 Silicon fiber refinement within the melt pool

Every sample was characterized via SEM to quantify Si fibers within the eutectic regions. First, cross-sectional cuts of the scanned lines for all alloys were prepared for SEM. Upon detection of contiguous (Figure 3.13 E, rather than F) and large (view field greater than 5 μm by 5 μm) eutectic area, five SEM captures, in equal spacing between the top and bottom of the area, were taken and measured for its constituent microstructures. At least 100 measurements of the diameter and the spacing of Si fibers were performed per image using ImageJ[87]. The diameter and spacing of Si fibers were measured with cylindrical projection in mind (Figure 3.17 D).
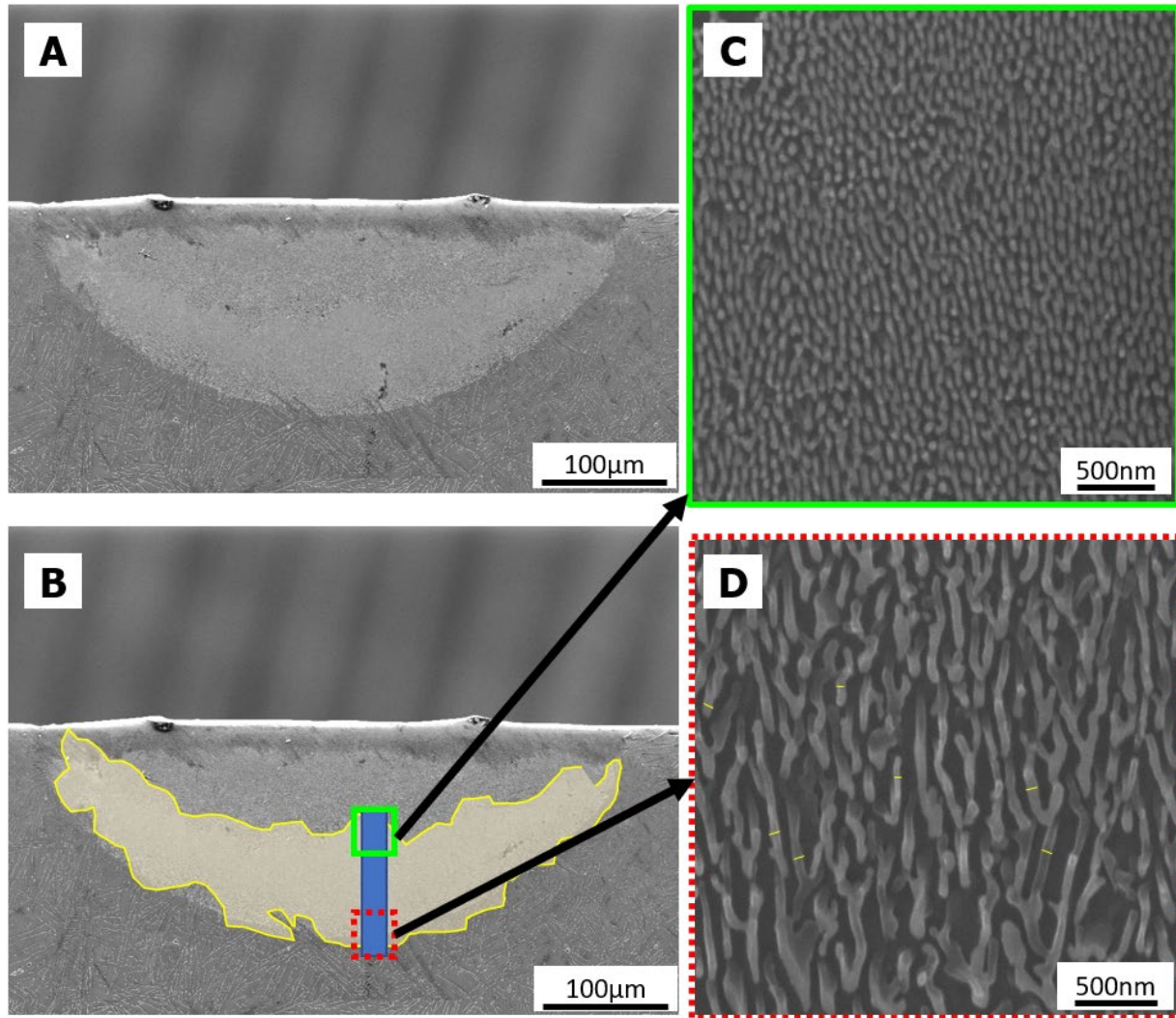
Figure 3.17 Regular eutectic formation and microstructure measurements at different depths. (A) Cross section of melt pool after LSR. (B) The same melt pool cross-section with a highlighted yellow region denoting the area of melt pool with fully eutectic microstructure, (C) and (D) are Si fibers from the top and the bottom of the eutectic area, respectively. Linear interception with cylindrical projection can be seen in the yellow bands in (D) (Al-20Si Exp#1). This figure shows how the total of 72 (18x3 original and 6x3 replications) experiments were characterized.

Measurements follow the linear intercept method with cylindrical projection. To further validate the microstructure size, the cross-sectional melt pool was processed with a focused ion beam (FIB), as chemical etching on the surface could alter the microstructure and potentially introduce errors in the measurements. The FIB etched surface was then inspected under high-resolution SEM (Helios 650) with a confocal lens. The FIB was applied to a eutectic region at

the bottom of the melt pool of experiment #1. The regional measurements showed a similar

result for Al-20Si (Figure 3.18), so it is assumed to be consistent with the linear intercept

method.
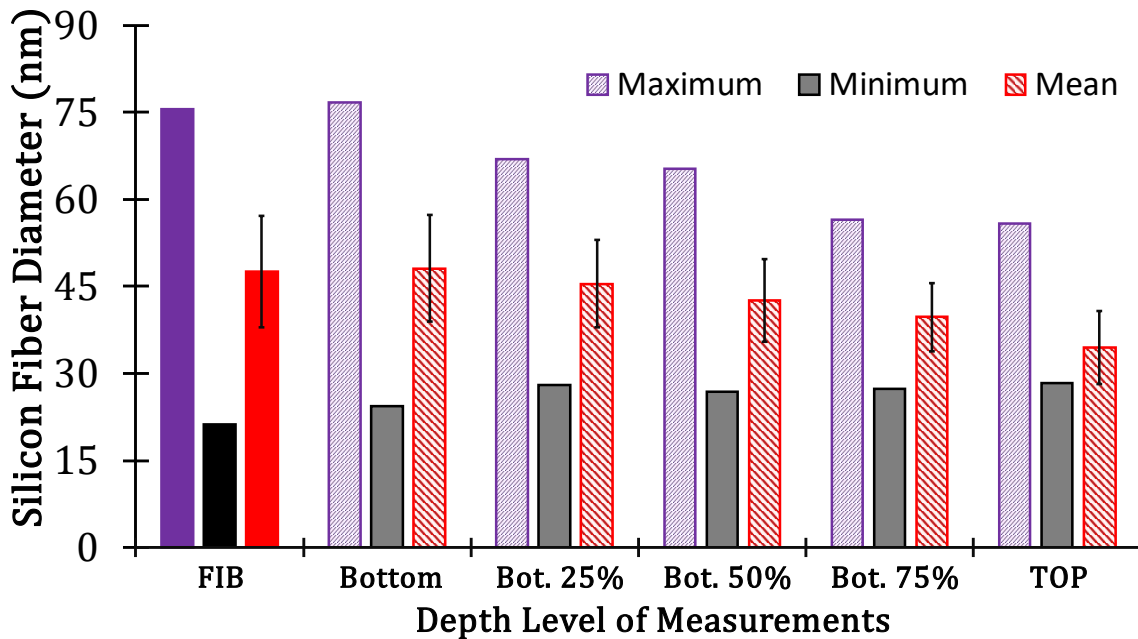
Figure 3.18 Graph for FIB/SEM comparison. FIB etched regions, which were illustrated in solid fillings on the left-most side, were measured at least 100 times for different fibers. The data shown here is from the experiment set 1 Al-20Si.

To evaluate the influence of Sr and Ce addition on the microstructure, a side-by-side

comparison of eutectic silicon fibers is given in Figure 3.19. The general trend in these three

alloys is that microstructure coarsens descending from the top surface of the melt pool and is

consistent with previous observations [5], [12], [50], [51]. This observation proved that this trend

is also valid for regular eutectic formations. Surprisingly, the Al-20Si-0.2Ce alloys had lower

eutectic volume fractions but improved silicon fiber refinement compared to Al-20Si-0.2Sr and
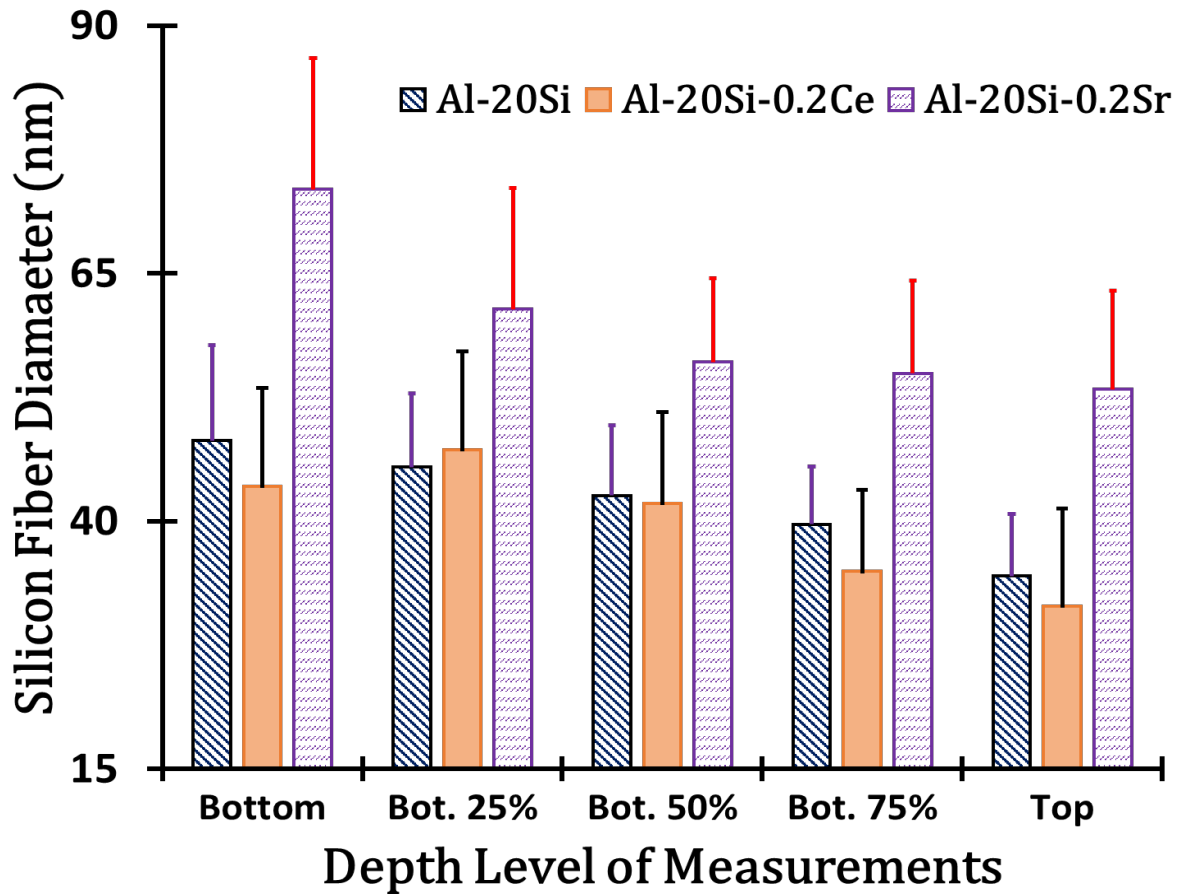
Al-20Si.

Figure 3.19 General overview of Si fiber refinement for the three alloys. Errors are represented in 1 standard deviation. Refinement level (ϕ) is calculated to be 28.4% for Al-20Si, 27.7% for Al-20Si-0.2Ce, and 27.5% for Al-20Si-0.2Sr.

Rare earth element addition to the Al-Si binary system has long been an area of investigation. Still, the mechanism behind the micro-alloying of rare earth element modifications, namely refinement of Si phases and coupled zone transitions, has not been fully understood[88]. It can be speculated that, since the heat history within the melt pool is similar, the undercooling amounts caused by micro-alloying elements are different. The other modifying factor of micro-alloying is dispersed intermetallic nucleants. When it comes to the nucleants, atom probe tomography, and high-resolution transmission electron microscopy characterization for these sets of experiments will likely enhance the understanding of non-equilibrium phase

formation, whether it arises from grain boundary solute rejection due to undercooling or from the

nucleants themselves.

The refinement level(φ), a quotient of measured average fiber size at the surface

(λSurface) and at the bottom (λBottom) of the melt pool, was found to be almost identical for all

of the samples at 28%. In laser processing, heat flows outward from the center of the melt pool,

while the solidification direction is normal to the melt pool interface pointing inwards towards

the center[89]. The difference in the thermal history is thought to be the root cause of this

refinement difference.

$$\varphi = 100 * \left(1 - \frac{\lambda_{Surface}}{\lambda_{Bottom}}\right) \tag{3.5}$$

3.2.4.3 Cooling rate in the melt pools

Application of LSR to samples on the order of a few centimeters long occurs in under a

second. For that reason, it is often acceptable to use conduction-based heat transfer models or

dendrite arm spacing models to analyze the thermal history in the remelted region[63]. Other

comprehensive multi-physics models are too computationally expensive and less applicable due

to their long run times, taking up to a couple of days to complete.

Of the many conduction-based models available, Rosenthal's approach has been studied

extensively. However, it assumes the laser heat source is an infinitesimally small point. This

introduces a major flaw: the temperature goes to infinity as the radius goes to zero (right under

the laser beam). The Eagar-Tsai model, on the other hand, is an advanced derivation of the

Rosenthal equation. The model accounts for thermal conduction but excludes interfacial energy

change and convection (Equation 3.6). While the list of symbols was provided in Table 6. 6, a

more detailed explanation can be found elsewhere[51]. The Eagar-Tsai approach assumes a

Gaussian intensity profile for the laser beam whereas the Rosenthal equation assumes a point

source. Thus, the former more accurately estimates cooling rates. Thermo-physical properties of

the Al-20Si alloys were assumed to be independent of temperature and calculated using the rule

of mixtures for Al and Si. The rare earth alloying elements were excluded from those

calculations. Therefore, the calculated cooling rates will be equal for the three different alloys

when all other LSR parameters are held constant.

$$\theta = \frac{n}{\sqrt{2\pi}} \int_0^{\frac{v^2 t}{2a}} d\tau * \frac{\tau^{-0.5}}{\tau + u^2} * e^{-\frac{\xi^2 + \psi^2 + 2\xi\tau + \tau^2}{2\tau + 2u^2} - \frac{\zeta^2}{2\tau}} \qquad (3.6)$$

Laser beam diameter and actual laser power output were measured manually. This affects

the n and u terms in Equation 3.6 (q and σ term in the more generic form, respectively). In order

to fit these parameters exactly, the depth and width of the melt pool were obtained via SEM

captures. Additionally, melt pool depth and width might vary within the laser entrance and exit

regions due to a lack of conduction bodies (Figure 3.20). Therefore, those regions will not be

considered when fitting the Eagar-Tsai approach. The coefficient of variant for these width and

depth ratios were found to be around 3 to 5 percent, implying a very accurate parameter.

Adjustments of n and u terms were performed until simulated melt pool dimensions matched that

of SEM captures. Upon completion of model fitting, the temperature profile is assumed to be

representative of experiments and can be used for calculating cooling rates.
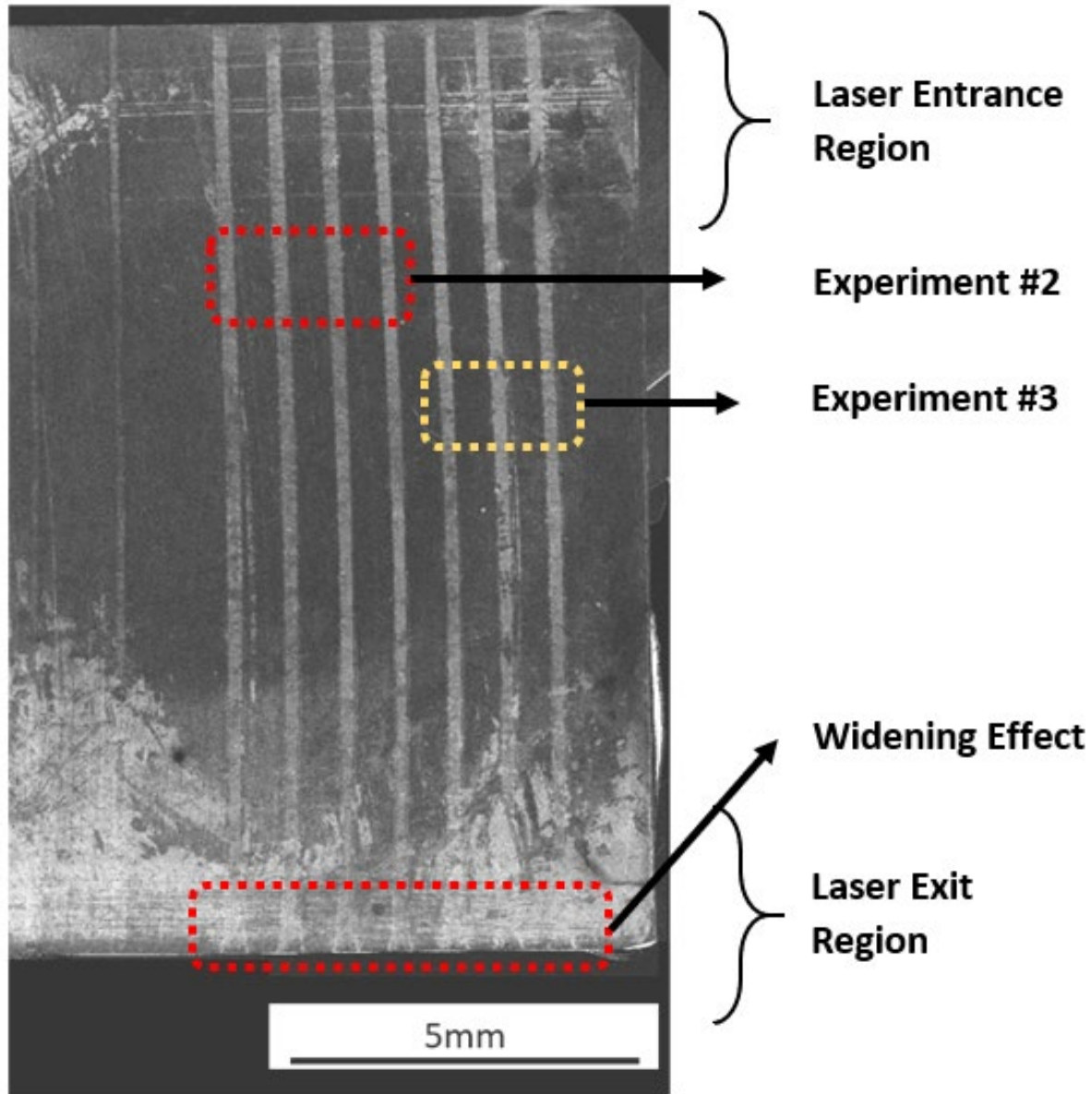
Figure 3.20 Entrance Exit SEM – Ce addition #2 and #3

Solutions to Equation 3.6 require numerical integration across a discretized domain with a uniform grid spacing of 50 μm. We set our domain to be 2 mm by 1 mm (yz cross section) with laser scanning along the x-axis. Thermophysical properties can be found elsewhere[90]. As the Eagar-Tsai approach can solve for the current temperature profile of our 2D cross-section at any arbitrary time post t = 0 s, we select t = 2 s as our calculation start time. This calculation start

time is chosen such that for the three tested laser scan speeds, a steady-state melt pool would

have developed. At t = 2 s, we then select a 2D YZ cross-section such that the center point of the

laser lies on the chosen plane. The temperature profile is then solved across 10 timesteps of 0.01

ms each. Once the temperature history is solved, cooling rates may be calculated from the

difference in calculated temperatures across a given timestep. Equation 3.7 calculates the cooling

rate and Table 3.3 gives the cooling rates for LSR parameter sets 1, 2, 3, 6, 9, 11, 13, 15, and 17.

$$\frac{dT^n}{dt} = \frac{T^n - T^{n-1}}{t^n - t^{n-1}} \tag{3.7}$$

Table 3.3 Cooling rate calculations and average eutectic formation comparison table

Experiment #	Cooling Rate (K/s)	Average Eutectic Formation	Std Dev for Eutectic Formation
1	1.80×10^4	37.98%	12.89%
2	6.78×10^4	62.00%	8.28%
3	4.15×10^4	49.67%	9.86%
11	1.16×10^4	30.24%	3.86%
17	9.30×10^4	17.52%	4.40%
18	7.74×10^4	23.12%	13.47%
6	1.57×10^5	11.43%	15.13%
9	2.09×10^5	10.92%	12.61%
13	8.15×10^5	7.13%	6.51%
15	1.12×10^5	7.64%	8.60%
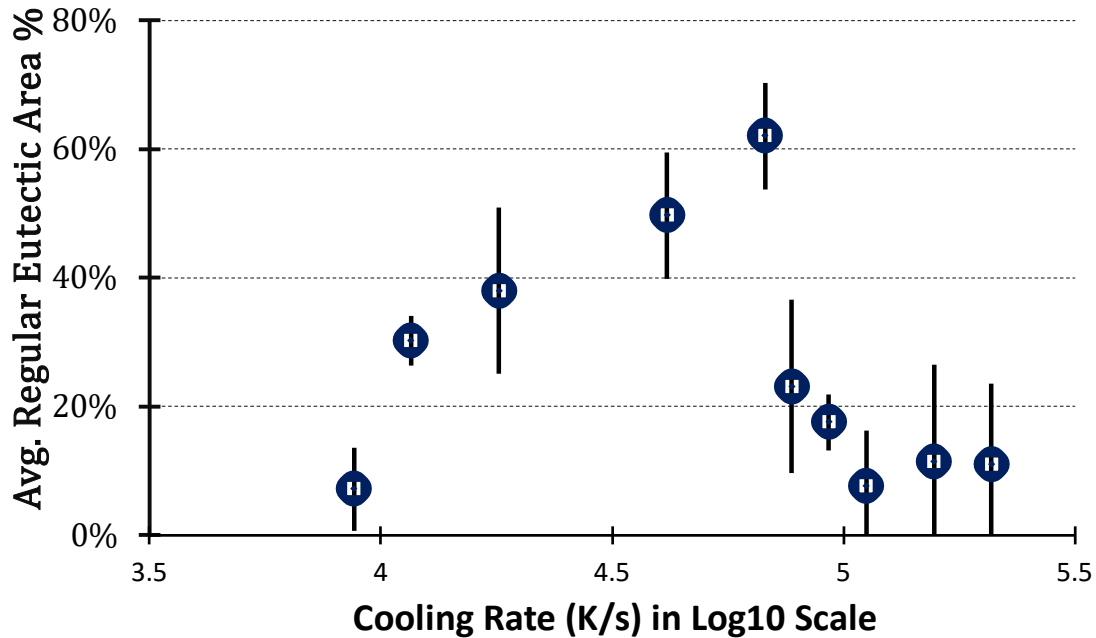
Figure 3.21 Cooling rates and fully eutectic area percentages relative to the total melt pool area. Errors are represented in 1 standard deviation.

Figure 3.1 suggests that there exists an optimal cooling rate for achieving above-average eutectic area formation within the melt pool on the order of 10^4 K/s. Cooling rates above and below this optimal value resulted in smaller eutectic area formation and higher standard deviations. In future studies, this information may be used to guide the LSR of Al-Si alloys targeting specific eutectic area percentages for selected mechanical properties. The cooling rate by itself falls short in explaining why the eutectic area formation percentage differs. Therefore, we inspect in detail the effect of the following kinetic variables: G (thermal gradient), V (solidification velocity), and ΔT (undercooling). Hearn *et al*. demonstrated that the thermal gradient can be calculated if the cooling rate and solidification velocity are known[91]. The cooling rate may be calculated with Equation 3.6. Calculations using the aforementioned model on eutectic microstructure grain size from our LSR experiments yielded solidification velocities generally within 10% of their respective laser scan speeds. At high cooling rates, the

solidification velocity can approach but never exceed the laser scan speed, therefore we substitute the laser scan speed for the solidification velocity in calculating G. G is then calculated via Equation 3.7:

$$CR \left[\frac{K}{s}\right] = V \left[\frac{m}{s}\right] * G \left[\frac{K}{m}\right] \tag{3.7}$$

Undercooling occurs due to the nucleation energy required for phase transformation. At higher undercoolings, the large deviation from the equilibrium phase transformation temperature can change the resulting microstructure. Khan and Elliott studied the effect of undercooling on the growth mode of Si and identified a certain threshold for the transition from equilibrium faceted growth to non-equilibrium fibrous or globular growth[92]. The kinetically modified undercooling in this study, ΔT_k, was calculated via Equation 3.8. The results are listed in Table 3.4 and shown in Figure 3.22, respectively:

$$\Delta T_k = 0.67 * V^{0.5} \left[\frac{\mu m}{s}\right] * G^{0.2} \left[\frac{K}{cm}\right] \tag{3.8}$$

Table 3.4 Calculated kinetic parameters

Experiment #	LOG10 Scale Cooling Rate (K/s)	Vmax (mm/s)	G (K/mm)	Calc. Undercooling ΔT_k (K)
1	4.3	25.4	708.7	18.1
2	4.8	25.4	2667.3	13.9
3	4.6	25.4	1634.4	15.3
6	5.2	101.6	1542.8	31.0
9	5.3	177.8	1174.2	43.4
11	4.1	25.4	457.2	19.8
13	3.9	101.6	86.1	55.3
15	5.0	101.6	1102.4	33.2
17	5.0	177.8	523.2	51.0
18	4.9	177.8	435.1	52.9
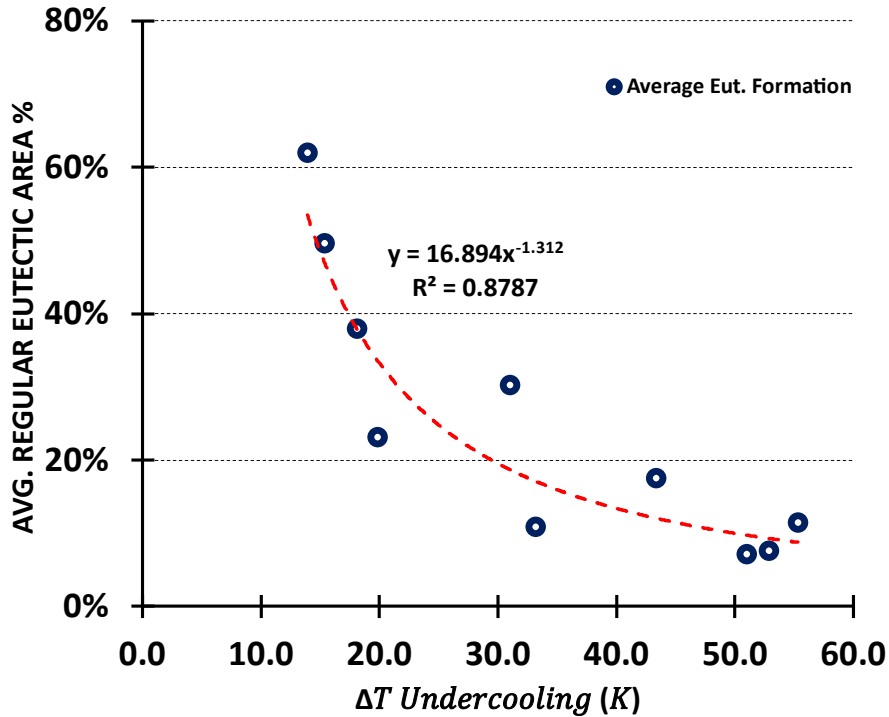
Figure 3.22 The average eutectic area is plotted against undercooling. The red dashed line shows that the eutectic area percentage correlates to undercooling with good agreement (R^2=0.88). This is an empirical power fit (y = $16.894x^{-1.312}$) and is intended to show the downward trend to the reader.

Pierantoni *et al*. performed numerous LSR experiments on Al-Si alloys for a range of Si concentrations[5]. They corroborate our finding that solidification velocity approaches the laser scan speed at high cooling rates and that there exists a relation between the degree of undercooling and the different microstructure growth rates. In this study, many different heat cycles were tested to induce a variety of cooling rates and, by extension, different undercoolings. LSR experiments by Lien *et al*. at four laser scan speeds and their resulting metastable liquidus curve extensions are plotted on the Al-Si equilibrium phase diagram in their study[65]. As the degree of undercooling increased, favorable microstructure formation shifted from equiaxed primary Si + fibrous eutectic to fibrous eutectic, and finally to Al dendrites + interdendritic eutectic. Additionally, increased solidification velocities constrain fibrous eutectic formation to a

narrow temperature range. This is in very good agreement with the calculated undercooling (Table 3.4). Thus, if higher eutectic area percentages are desired, the undercooling amount must be high enough to mitigate primary Si formation, but not so large that we exceed the fibrous eutectic to Al dendrite + interdendritic fine eutectic threshold. The ideal range of undercooling for obtaining high fibrous eutectic volume is calculated to be less than 20K.

3.2.5 Conclusions

- Microstructures in the melt pools in the laser surface remelted arc-cast hypereutectic Al-20Si, Al-20Si-0.2Sr and Al-20Si-0.2Ce alloys comprised of mixtures of fully eutectic and hypoeutectic (primary Al dendrites and inter-dendritic eutectic). Eutectic regions in LSR Al-20Si alloy contain approximately 18 wt. % Si, which is higher than the equilibrium eutectic composition.

- The Si fibers in the eutectic microstructures of LSR Al-20Si alloys have been reduced from a few microns in as-cast to less than 50 nanometers with rapid solidification and rare earth modification. Minimum average silicon fiber sizes in Al-20Si-0.2Ce were observed to be 35±8nm.

- Si fibers in the regular eutectic structure were found to be more refined towards the top of the melt pool.

- The volume fraction of the fully eutectic morphology in the melt pool depends on the cooling rate. Cooling rates for different experiments were calculated using the Eagar-Tsai approach and 10^4 K/s was found to be the optimal value to maximize the volume fraction of the fully eutectic morphology in the melt pool.

- The average area percentage of fully eutectic colonies in the melt pool in the investigated Al-20Si, Al-20Si-0.2Sr and Al-20Si-0.2Ce alloys decreases from ≈60% to ≈10% with increasing undercooling, ΔT, from ≈10 K to ≈50 K.

3.3 Microstructural evolution and hardness of rapidly solidified hypereutectic Al-Si surface layers by laser remelting

3.3.1 Introduction

The use of high silicon substance Al-Si alloys in the automobile, aerospace, and transport industries has been constantly increasing due to their excellent mechanical, tribological, and casting properties[52], [53]. However, when the silicon content exceeds 20 wt%, the alloys suffer from a deterioration of other mechanical properties due to the formation of massive and angular silicon particles with sharp edges, which act as crack initiation sites and significantly reduce fatigue life. Therefore, to meet the growing demands in automotive, transport, aerospace, marine, aeronautical, and missile technology; the size and morphology of the silicon phase must be refined and modified as the finer primary silicon crystals generally result in improved mechanical properties, such as toughness and ductility[54].

Refinement of the eutectic Si can be achieved by controlling the nucleation and growth of the silicon phase mainly by chemical methods and rapid solidification. The chemical modification involves the addition of some modifier elements, in trace levels, such as sodium[93], [94], strontium[95], [96], and rare earth metals [97], [98]. Na and Sr are well accepted as a eutectic Si modifier, which effectively modifies the morphology of eutectic Si from flake- like to fibrous at a level of a few hundred parts per million. Shina *et al*. [96] have shown that the addition of Sr, as a master alloy, to Al-10.5%Si-2.0%Cu alloy, transformed the morphology of the eutectic Si from coarse acicular shape to a lamellar and a fibrous one, as the amount of Sr increased. Knuutinen *et al*. [97] have studied the effect of Ba, Ca, Y, and Yb on 356.0 alloys, indicating that all additions promote alteration in the eutectic and growth modes. Ba and Ca led to a good modification of Si into a fine fibrous silicon structure, while Yb and Ca

addition and eutectic Si were refined to a smaller size, but still maintained a plate-like morphology. Nogeta *et al*. [98] have studied the effects of different concentrations of individual additions of rare earth metals (La, Ce, Pr, Nd, Sm, Eu, Gd, Tb, Dy, Ho, Er, Tm, Yb, and Lu) on eutectic modification in Al-10 wt.%Si and showed that all of the rare earth elements caused a depression of the eutectic growth temperature, but only Eu modified the eutectic silicon to a fibrous morphology with different responses of each element.

For the hypereutectic Al-Si alloys, where the microstructure consists of coarse, angular, and irregular shapes of the primary Si immersed in Al-Si eutectic, the phosphorus (P) proved to be an effective modifier and refiner of primary Si particles but not for the eutectic Si [55]. Wu *et al*. [56] have reported that the addition of phosphorus to the Al-20 wt.%Si alloy with a controlled temperature and holding time has led to a reduction of the size of the primary silicon to 20 μm due to the formation of primary Al particles, which acted as heterogeneous nucleation agent on the solid primary Al particles, which promotes the modification and refinement of the primary Si without affecting the eutectic Si morphology. A combination of P with other elements was also investigated to refine the primary and the eutectic Si. Faraji *et al*. [57] have demonstrated that (P + Sr) was effective to some extent in improving the strength and ductility but the size of the primary silicon crystals did not reach the nanoscale size. Li *et al*. [99] have demonstrated that the morphology of primary Si was refined from coarse irregular star-like and plate- like shape to fine block-like when the addition contents of Y increased to 0.8%. The average size of primary Si reduced from 89 μm to 33 μm. Xia *et al*. [100] have reported that the addition of erbium (0.5%Er) refined the primary Si from 94 μm to 33 μm and the morphology transfers from coarse star-like and polygonal shape to a fine blocky shape. A similar result was obtained by the addition of Er to 05%[60]. However, when the level of rare earth Er was up to 0.8%, the primary

and eutectic Si phases became coarser. It is clear from the above-mentioned research that modification of hypereutectic Al-Si alloys by chemical additions is not efficient in reducing the size of the primary Si to a micron- scale or nano-size, nor does it produce a desirable shape. Besides, there are a lot of negatives resulting from the chemical agents, such as evaporation, and oxidation during services. Qian *et al*. [61] and Liao *et al*. [62] have reported that Sr modifier increases the porosity level and deteriorates the performance of the castings.

Rapid solidification methods, such as melt spinning [3], powder atomization [4], and laser melting [50], [63], [64], [66], [101], [102] proved to be effective approaches for the refinement of the Si phase. The high-cooling rates associated with these processes, which may reach 10^5 to 10^7 °C/s play a large role in the size of the critical nuclei, and subsequently, the effective number of nuclei that will ultimately produce fine-grained structures. Chaus *et al*. [69] have recently shown that rapid quenching technology resulted in significant grain refinement of the eutectic constituents (α (Al) + Si), as well as primary silicon, which gave rise to better tensile and fracture properties compared to that of the conventionally cast Al-18%Si-2%Cu alloy. Xu *et al*. [3] obtained a 40 μm thick melt-spun ribbon by using a single roller melt- spinning technique of the Al-20 wt. %Si alloy and reported a drastic change in the morphology of the primary Si to fine block-shape with a significant reduction in the size to 2 μm. Kalay *et al*. [4] have studied gas-atomized Al-Si powders of different compositions (15, 18, 25, and 50 wt. %Si), and showed that as the droplet size decreased, the structure became much finer. The primary silicon in Al-50 wt. %Si alloy continued to form even at the smallest droplet sizes (25 μm) with sizes ranging from 2 to 5 μm, the Al-25 wt. %Si showed a predominantly eutectic state with a few primary Si while Al-18 wt. %Si, and Al- 15 wt. %Si showed dendritic and eutectic structures. Laser surface treatment of hypereutectic Al-Si alloys has been studied by several investigators, who showed a

reduction of the primary Si to 10 μm, and the formation of fibrous eutectic Si. Bhowmik *et al*. [102] have recently developed Al-50 wt.%Si laser-clad on Al 7075 substrate and found local heterogeneity in the composition and the structure with the single-clad layer due to different cooling rates. Three phases, namely primary Si of size, Al-Si eutectic, and α-Al dendrites were obtained with an increase in the solubility of Si in Al. Recently, Abboud and Mazumder [64] have produced a series of Al-Si layers on a commercially pure Al substrate with compositions 35, 50, and 60 wt.% and showed a great refinement in all the micro- structural constituents and increased hardness and the highest cooling rates did not suppress the formation of the primary Si but reduced the sizes to 2 μm and increased the amount of the nano-fibrous eutectic. Lien *et al*. [83] reported a high density of nano-twinned ultrafine Si in hypereutectic Al-Si alloy by laser surface remelting of Al-20 wt.%Si alloy.

It appears from the above-mentioned review that there is an increased interest in the high-silicon content of Al-Si alloys due to their outstanding mechanical properties, especially after the modification. Therefore, to increase the engineering and industrial applications of these alloys, the size, and the morphology of silicon crystals should be refined to a minimum value. The present investigation is an attempt to use the laser melting and remelting technique, at controlled laser processing parameters, for two purposes. First, to fabricate high silicon Al-Si alloyed layers by laser melting at a fixed laser power density and scan speed. The second is to remelt the produced layers at a fast scan speed with relatively low power levels to refine the silicon phase to a nano-sized. The other objective of the study is to measure the nano-indentation hardness in different areas of the eutectic region and correlate the hardness value with the resulting eutectic spacing. The long-term objective of this research is to create a surface layer

rich in nano- sized silicon crystals on the aluminum surface, which improves its wear resistance [103].

3.3.2 Materials and sample preparation

3.3.2.1 Preparation of the Al-Si Layer

A commercial purity aluminum (CP Al) plate of 50 mm long x 25 mm wide x 6 mm thick, and silicon powder, of 325 mesh, and 99.9% purity have been used to prepare the alloyed layers using conventional laser alloying technique [64]. Four slots were made, two of which are 0.3 mm deep, and the other two 0.35 mm deep were prepared along the length of the aluminum plate by a machining process. The slot's width was kept constant at 1 mm. The reason for preparing slots of different depths is to obtain different silicon ratios after the laser melting. The slot dimensions together with laser processing para- meters were chosen based on experience and previous experimental research by Abboud and Mazumder [64]. Silicon powder was inserted and compacted in the grooved aluminum plate until the slot gap was filled and the extra powder was removed. Great care was taken to ensure the uniformity of the silicon powder distribution in the designated spaces before the laser treatment. This method was chosen due to the difficulty of feeding the silicon powder into the feeder, as well as the powder jam, which hinders its regular flow.

3.3.2.2 Fabrication and remelting of the Al-Si track layer

A solid-state Nd-YAG (HLD 4002) disk laser operated at 600–2000 W with a 2 mm beam diameter was used to produce the Al-Si alloyed track layers and for overlapping remelting treatments. The Al-Si alloyed layers were prepared by irradiating the laser beam onto the surface of a commercial purity Al substrate, which contains silicon powder to a specific depth. In this

experiment, the laser head was stationary while the Al substrate was moving. The relative movement between the Al substrate and the stationary laser head was controlled by a computerized table moving in three perpendicular directions (X-Y-Z). The movement in X-direction was used to control the scanning speed while in Z direction is used to change the laser beam diameter. The first experiment was designed to fabricate the Al-Si tracklayers of 40 mm length using a laser power of 2000 W and at a scanning speed of 10 mm/s, followed by a remelting process at a constant traverse speed of 180 mm/s and different laser powers (1000, 800, and 600 W). Two tracklayers, 1A (two remelts) and 2A (four remelts) were selected for study and analysis. Table 3.5 illustrates the various processing parameters used in the fabrication and remelting treatments of the tracklayers 1A and 2A. Before performing any remelting experiments, the top surface of the alloyed track was ground, polished, cleaned, and slightly etched. The processes of melting and remelting were conducted within an inert controlled atmosphere to avoid oxidation during melting and solidification.

Table 3.5 Processing parameters used in the alloy fabrication and remelting treatments. The laser beam diameter was kept constant at 2 mm.

Tracklayer No	Laser Treatment	Power (W)	Speed (mm/s)	Si Powder Thickness (mm)
1A	Fabrication	2000	10	0.30
	Remelting	2000	180	--
	Remelting	1000	180	--
2A	Fabrication	2000	10	0.35
	Remelting	2000	180	--
	Remelting	1000	180	--
	Remelting	800	180	--
	Remelting	600	180	--

3.3.2.3 Microstructure characterization

After the first laser melting and remelting experiments were done, transverse sections were cut, cold mounted, ground on 400, 600, 1200, and 2000 grit SiC paper then polished with a 3 µm and fine polished with 0.3 µm. The samples were cleaned and etched with Keller's reagent (containing 95 ml of H_2O, 2.5 ml of HNO_3, 1.5 ml of HCl, and 1.0 ml of HF) for 3 s, rinsed with water, and then dried. The composition and the microstructure of the alloyed zones were examined by scanning electron microscopy (TESCAN MIRA3 FEG SEM) equipped with an energy-dispersive spectrometry (EDS) detector and transmission electron microscopy (JEOL 2010 F AEM). Thin foils were prepared by cutting a slice 0.3 mm thick parallel to the laser scan and further ground to 100 µm. A punching tool was used to obtain a 3 mm diameter foil. The

sample was mechanically polished and finally thinned by a Gatan Precision Ion Polishing System where low-angle and low-current polishing conditions were used in conjunction with a liquid nitrogen cold stage. The electron microscopy and nanoindentation experiments were conducted at the Michigan Center for Materials Characterization (MC)[2] at the University of Michigan.

3.3.2.4 Nanoindentation hardness

The nanoindentation hardness and elastic modulus of the eutectic region of tracklayer A-1, which exhibited different spacings, were measured at different locations. The indentation hardness experiment was carried out at room temperature employing a Bruker TI-950 Triboindenter equipped with a diamond tip of a three-sided Berkovich probe. The indenter was employed to measure with a peak load of 1mN a quasistatic trapezoidal loading function (5 s load and 2 s unload hold time) and an indentation depth of 200 nm. The reported data is an average of at least three indents in each zone. Measurements were carried out on the transverse section, which was mechanically polished to 0.3 μm finished, and cleaned with ethanol.

3.3.3 Results

3.3.3.1 Tracklayer – 1A

General shape and dimension of tracklayer 1A
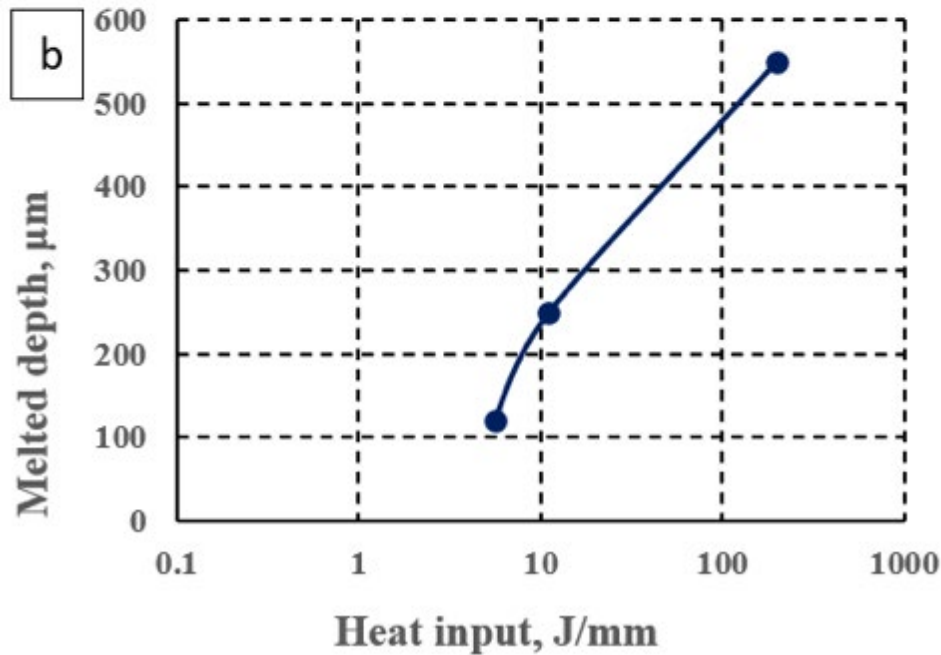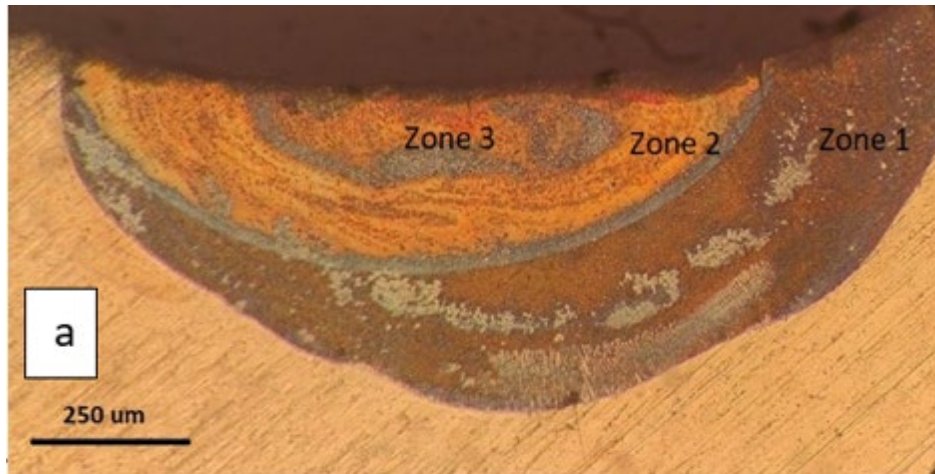
Figure 3.23 a Cross-section of the laser-fabricated Al-Si alloyed layer (tracklayer 1A) and laser remelted at different heat inputs. b variation of the remelted depth with the heat input

Figure 3.23 a Cross-section of the laser-fabricated Al-Si alloyed layer (tracklayer 1A) and laser remelted at different heat inputs. b variation of the remelted depth with the heat input(a) shows a typical transverse section of the laser fabricated Al-Si alloyed layer (tracklayer-1A), which is processed at a power (P) 2000 W, a beam diameter (bd) 2 mm, and scanning speed (v) 10 mm/s. After the completion of the first melt to synthesize the alloy, it was remelted twice at a traverse speed of 180 mm/s, and the laser powers 2000 W and 1000 W, respectively. The as-

fabricated alloyed zone, before it remelted, had a conduction-limited shape of a total depth of

0.55 mm and a width of 1.4 mm (Figure 1(a)). It is apparent from the figure that all the silicon

powder has melted and dissolved in the molten aluminum forming a heterogenous Al-Si alloy

but with a fine structure (Figure 3.23(a), zone 1). The primary Si particles tend to segregate and

cluster at the center and the edge of the melted zone. However, when remelting was performed at

a faster speed and less power, the structure became much finer with less heterogeneity due to the

rapid remelting process. The depths of the remelted zones (2 and 3) were 250 and 120 µm at

powers of 2000 W and 1000 W, respectively. Figure 3.23 (a) also showed a narrow dendritic

region at the interface between the base metal and the melted zone 1, which are interpreted as α-

Al dendrites. Also, the interfaces between the melted zone 1 and the melted zones 2 and 3

showed an agglomeration of fine silicon particles that coexisted with near eutectic and

hypoeutectic structures. The upper part of the third melted zone showed the influence of the

convectional fluid flow, which led to the formation of Si-rich and Si-poor zones and pushed the

silicon particles toward the top and the edges of the melted zone. It is important to mention here

that segregation and clustering of the silicon crystals are very common in a conventional cast and

even the rapidly cooled hypereutectic Al-Si alloys due to the lower density of the Si particles and

the strong convectional fluid flow, which arises from the temperature gradient and other

solidification parameters. Figure 3.23 (b) illustrates the decrease of the remelted depth with

reducing laser power (or decreasing the heat input), which is equal to the (P/v, J/mm). As the

heat input reduces, the depth decreases, and thus the cooling rate increases. Figure 3.23 (b)

indicated that the melted depth decreased linearly with the decrease in the heat input and when

the heat input reached a minimum value of 5.55 J/mm, the depth decreased rapidly reaching 120

μm. Due to the smallest melted depth of the third zone, it is expected that the cooling rate will be the highest compared to the first and second melted zones and will display the finest structure.

Composition analysis

EDS analysis was performed at different locations in different zones in the Al-Si alloyed layer, and it was found that the silicon content in the lower part, where the microstructure exhibited a dendritic structure, was slightly lower than that in the other part of the alloyed layer (see Figure 3.23 (a)). The silicon content near the interface was 17.6 wt. %Si, while it was 20 wt. %Si in the eutectic region excluding the Si particles and 24 wt. %Si in the region, which showed clustering of Si crystal and the matrix (Figure 3.24(a)). Similar values were obtained in zones 2 and 3 (Figure 3.24 (b,c)). The average composition of the alloyed layer was found to be 25 wt. %Si. The results of the EDS analysis of the eutectic region showed an increase in the silicon content of the eutectic concentration to 20 wt. %Si in zone 1 and 22 wt. %Si in zone 2 and 24 wt.% in zone 3 (Figure 3.24 (c)). These values are much higher than those reported in the Al-Si diagram (12.6 wt. %Si). This indicates that as the melted depth became smaller, the cooling rate increased, pushing the eutectic point towards a higher silicon content as reported by Zhao *et al*. [67] in an earlier study on Al- 20 wt. %Si and by Abboud and Mazumder [63] on Al-17 and 20 wt. %Si alloys.
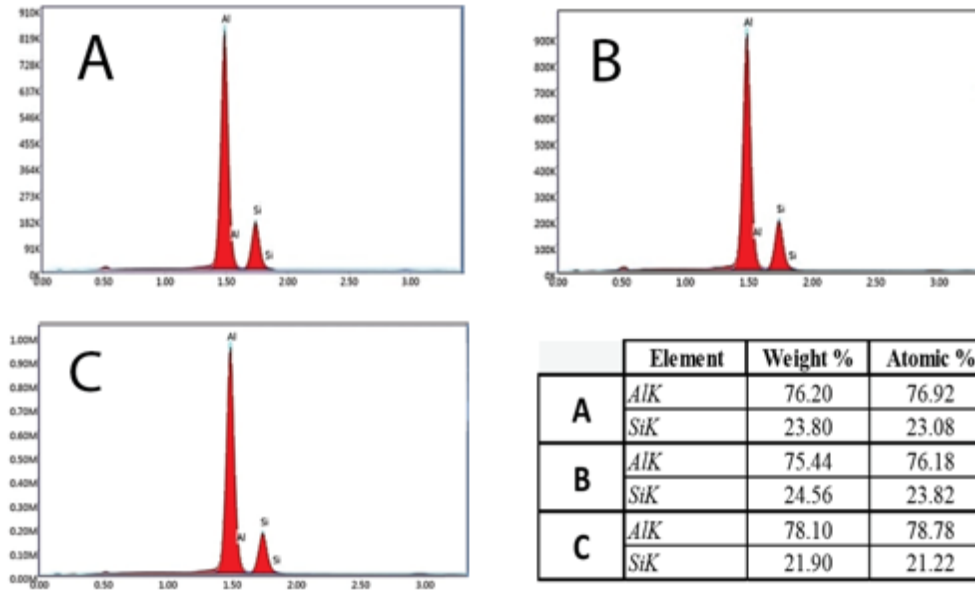
Figure 3.24 EDS-spectrum at different locations in the melted zone: (a & b) area analysis includes the eutectic region and few Si particles in the melted zone 1, (c) eutectic region in remelted zone 2

Microstructural analysis

The microstructure of zone 1 in Figure 3.23 (a), which is processed at 2000 W and 10 mm/ s, exhibits a hypoeutectic structure in the lower part, becoming fully eutectic and hypereutectic above the interface. The refined structure, consisting of α-Al dendrites and Al-Si eutectic occupies a volume of approximately 80% of the remelted zone, while the rest is a dispersion of the isolated primary silicon phase (Figure 3.25(a)). The primary Si crystals are distinguished by their complex and irregular shape with many side branches and with sizes ranging between 3 and 5 μm, while the eutectic structure shows a fibrous morphology with an average spacing of 75 nm (Figure 3.25). The microstructure of zone 2, which was processed at the scanning speed (180 mm/s) is much finer than that shown in zone 1 and consists of relatively finer primary Si crystals of size about 2 μm with columnar dendrites radiating around and near the primary Si, and a significant increase in the eutectic colonies of a spacing ranging between 30 and 50 nm (Figure 3.25 (c,d)). The major difference between the microstructures of zone 1

and zone 2 apart from the refinement, is the decrease in the volume fraction of the α-Al dendrites in the matrix with an increasing amount of the eutectic colonies (Figure 3.25 (a,c)). Furthermore, the primary Si crystals are found to be partially surrounded by the α-Al phase with many eutectics' colonies grown directly from it (Figure 3.25 (c)).
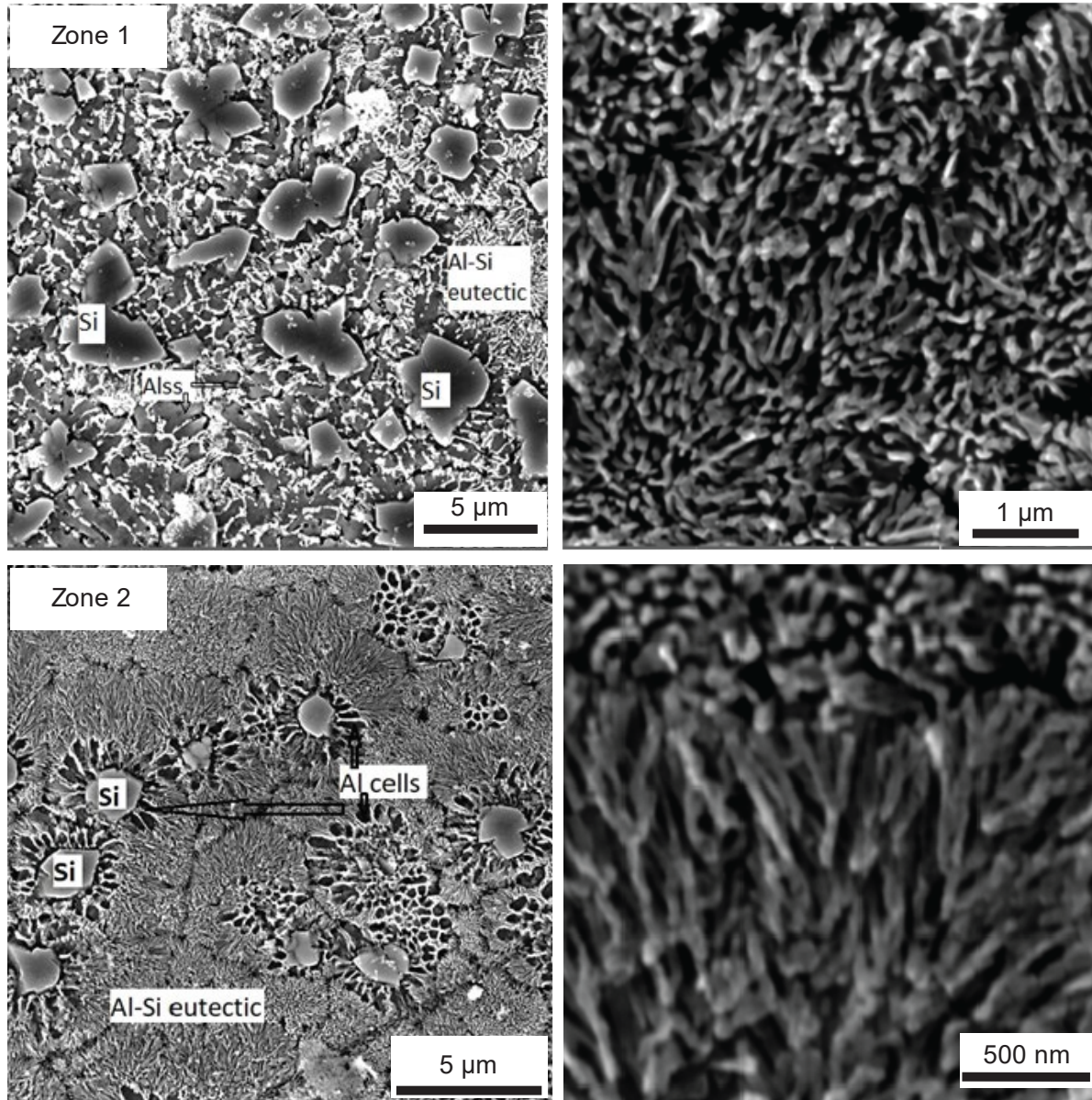
Figure 3.25 SEM micrographs were taken at different locations in the laser-remelted zone of the Al-25wt%Si layer showing the primary Si crystals, α-Al dendrites, and Al-Si fibrous eutectic. a and b were taken from the lower part of zone 1 (2000W, 10 mm/s). c and d were taken from the upper region of zone 2.
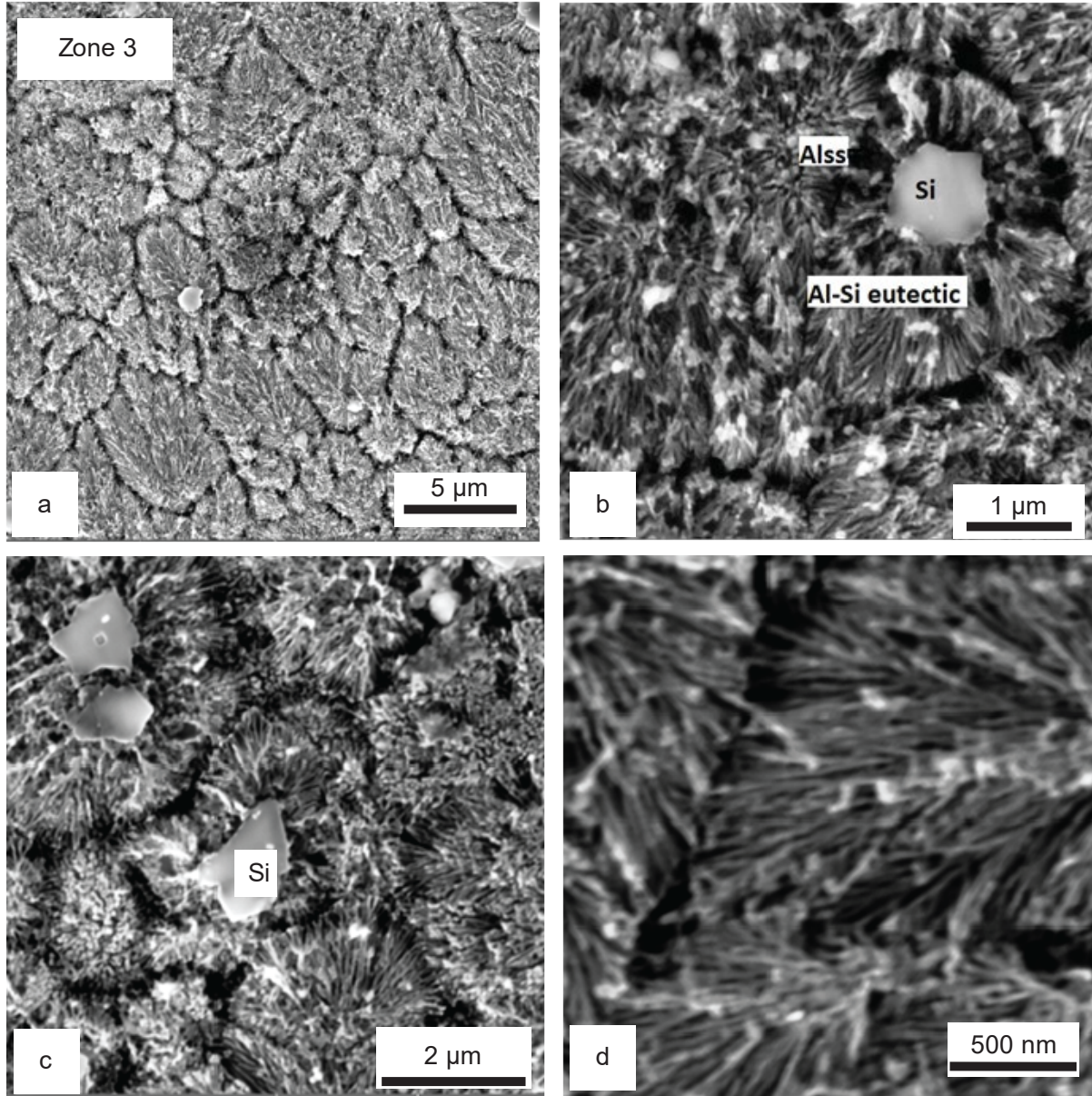
Figure 3.26 SEM micrographs were taken at different locations in the laser remelted zone of Al-25wt%Si layer processed at (1000W and 180 mm/s) showing sub-micron primary-Si crystals, few α-Al dendrites, and a high proportion of the Al-Si eutectic. d SEM micrograph showed nanofibrous Al-Si eutectic

To achieve further refinement of the microstructural constituents of the Al-25 wt.% layer, a second remelting treatment was performed, but at 1000 W and 180 mm/s. The resulting solidified zone was 125 μm deep. The average size of the primary Si flakes was reduced to ≤ 1.5

μm (Figure 3.26(a-c)). As the primary silicon became smaller, its morphology changed from star-like to blocky and granular with a slight tendency to branch laterally. On the other side, the Al-Si eutectic was modified and showed an interwoven fibrous structure of spacing ranging between 20 and 30 nm. Most of the eutectic silicon fibers grew from the vicinity of the primary Si crystals and spread randomly in different directions (Figure 3.26(d)).

Nanoindentation hardness

Nanoindentation hardness (NIH) was measured at different locations in the remelted zone of the Al-25 wt.%Si alloyed layer including the fully eutectic and the hypereutectic regions, and the resulting indentation hardness was correlated with the eutectic spacing (λ). The result showed that the indentation hardness of the transverse section of the remelted Al-25 wt.%Si alloyed layer was 1.75, 2.55, and 3.15 GPa, which corresponds to the eutectic spacing, λ, of 50, 35, and 20 nm, respectively. It is clear that as the heat input decreases, the melt depth becomes smaller and cooled rapidly so as a result, the eutectic spacing λ decreases, and the nanoindentation hardness increases. The maximum value obtained was 3.15 GPa at the top of zone 3, which displayed the finest structure with λ, as small as 20 nm. However, some regions in the upper part of zone 3 showed high values ranging between 5.4 and 6.4 GPa. It is expected that the presence of nano-sized primary Si contributed to the high hardness value considering that the indentation of the primary silicon alone is approximately 10 GPa. The effect of the increased nanoindentation hardness (H) with a decrease in the eutectic spacing (λ) is presented in Figure 3.27. An empirical relationship followed this formula, $H = K (\lambda)-n$ where H is the hardness in GPa and λ is the average spacing in nm, K and n are constants dependent on the composition of the alloy. In the present work, the value of the constant n is approximately 0.6, while the constant K is 20 ± 1 for

Al-25 wt. %Si. The general trend of increased strength in ultra- fine laser melted Al-Si fibrous eutectic is consistent with earlier studies by Lien *et al*.[65].
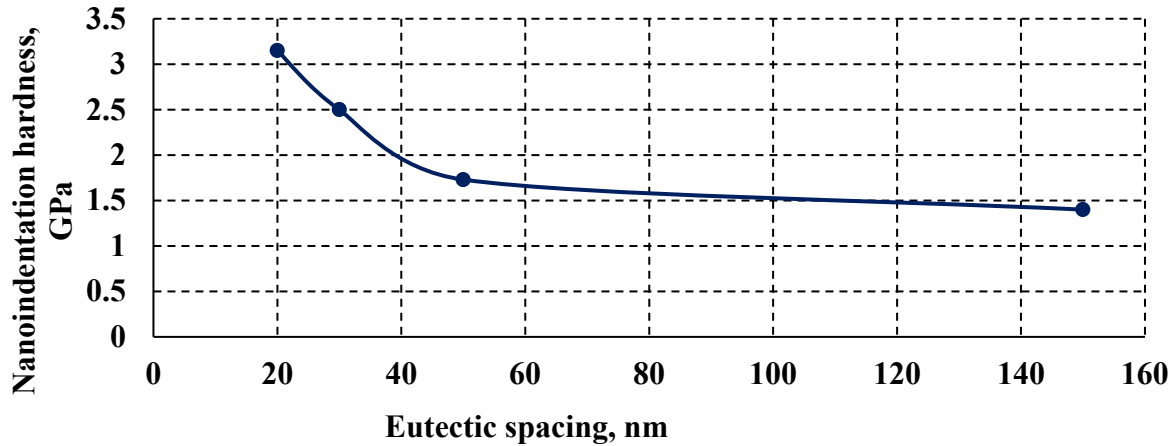
Figure 3.27 Nanoindentation hardness as a function of eutectic spacing, measured in different locations of the transverse section of Al-25wt.%Si alloyed layer.

3.3.3.2 Tracklayer 2-A

Microstructural characterization

A cross-section of the tracklayer 2A, which was fabricated at a power 2000 W and a speed of 10 mm/s and remelted at 180 mm/s, is presented in Figure 3.28(a). It is apparent from the figure that both zones 1 and 2 showed a high percentage and conglomeration of the primary Si phase in the center of the melted zone while at the edges, the concentration was lower. EDS analysis at different locations in zone 1 and zone 2, showed a silicon content in the Si-poor region ranging between 22 and 25 wt.%Si while in the Si-rich region ranged between 29 and 33 wt.% (Figure 3.28 (b)). Based on the optical micrograph, SEM images, and the EDS results, the average content of silicon was estimated to be approximately 30 wt.% Si, which is higher than the 1A tracklayer. Microstructure analysis of the two zones showed a typical hypereutectic structure consisting of a star-like primary Si phase, a high proportion of aluminum dendrites, and

Al-Si eutectic. The average size of the primary Si in the melted zones 1 and 2, were 7 μm and 4 μm, respectively. The resulting structure and the very small size of the primary Si were due to the high cooling rate associated with laser melting. Furthermore, the obtained sizes are much finer than those obtained by the conventional casting process, which was in the range of 50–100 μm and much closer to those obtained using the rapid solidification technique (2–10 μm) that was reported by [4], [41].

To achieve further refinement of the primary Si crystals to the nanoscale level, the surface of the Al-30 wt.%Si alloyed layer (tracklayer 2A) was subjected to several overlapping laser remelting at a fast speed of 180 mm/s and powers of 1000, 800, and 600 W, respectively. A typical cross-section and a top view of the remelted surface layer are shown in Figure 3.29(a, b), respectively. Figure 3.29 (b) showed the segregation of very fine primary Si near the top surface in all the remelted zones. More details about the microstructure of each zone are presented in the following Figure 3.30, Figure 3.31, and Figure 3.32. Figure 3.30 showed the microstructure of zone 2, which was remelted at 2000 W and showed a fine hypereutectic structure consisting of primary Si crystals of sizes ranging from 2 to 3 μm, embedded in a hypoeutectic matrix containing α-Al dendrites and Al-Si eutectic. Figure 3.31 (a,b) presents the microstructure of zone 3, which was remelted at 1000 W and showed a further refinement of the microstructural constituent as the size of the primary Si crystals was reduced to 1–2 μm and increased in the proportion of the eutectic structure. Zone 3 marks the beginning of the formation of a modified eutectic resembling a fur-like shape (Figure 3.31 (b)) emerging from the pre-existing primary Si crystals and branching out. Figure 3.32 (a-d) shows the microstructure of zone 4, which is remelted at the lowest power 800 W, and experienced the highest cooling rate. There was a significant increase in the quantity of the modified eutectic and a decrease in the

amount of α-Al dendrites around the primary Si and within the matrix. Furthermore, the sizes of

the primary Si crystals were refined to 1 μm, while the eutectic spacing was reduced to less than

20 nm.
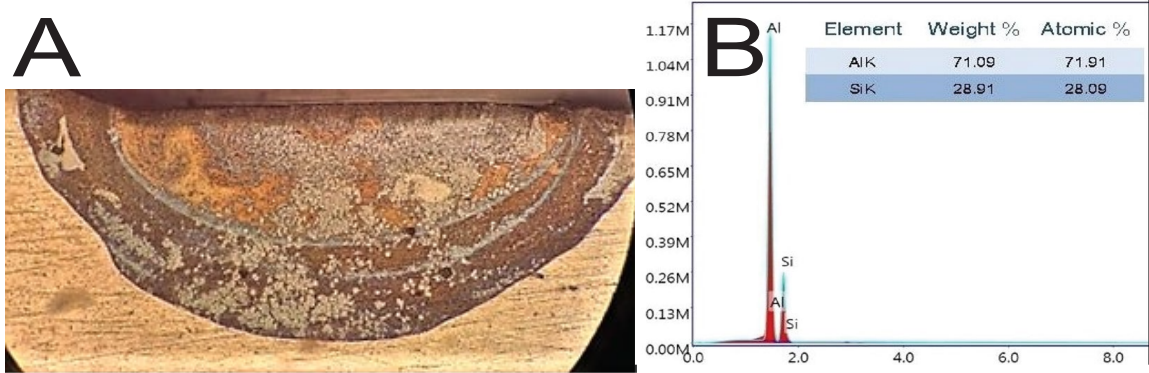
Figure 3.28 a Cross-section of track layer (2A) fabricated at 2000W, 10 mm/s and remelted at 180 mm/s. b EDS spectrum taken from the center of the upper remelted zone.
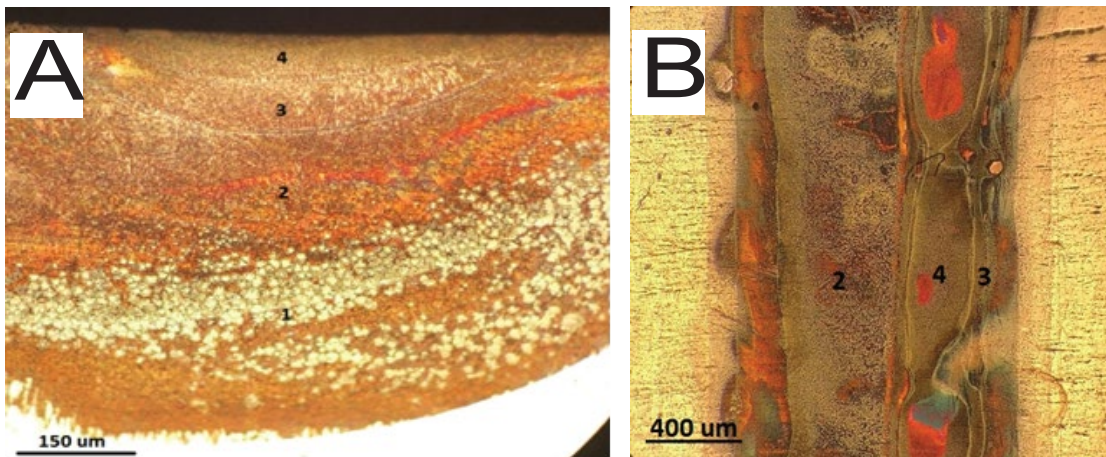
Figure 3.29 a Transverse section, b top view of the tracklayer (Al-30wt.%Si), showed the laser remelted zones at different parameters, remelted zones 2, 3, and 4 were processed at scanning speed 180 mm/s and powers 2000W, 1000W, and 800W, respectively
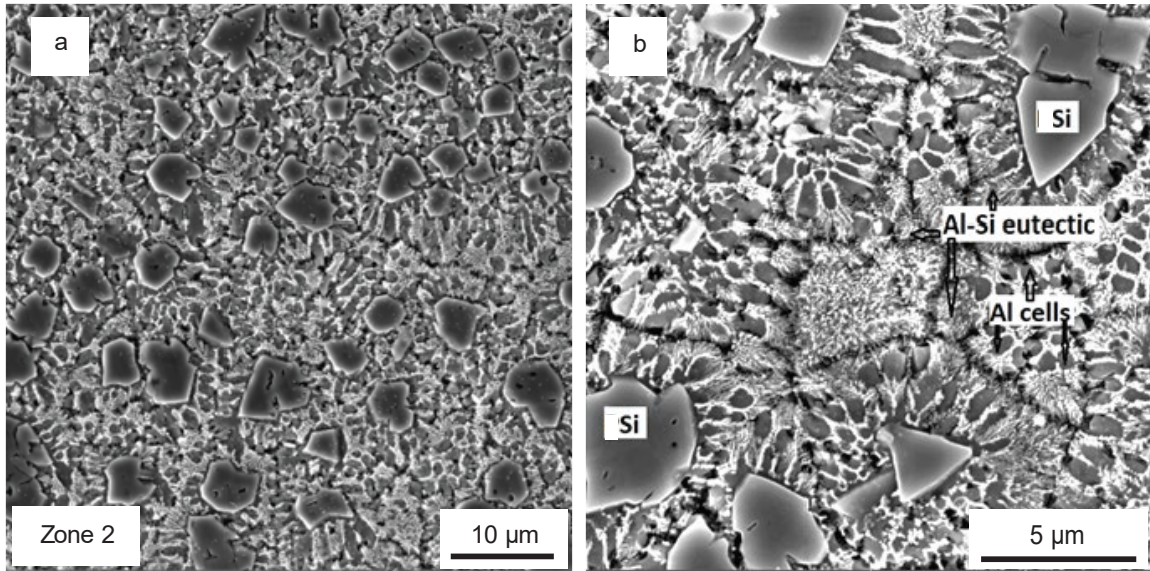
Figure 3.30 a SEM micrograph showed the microstructure Al-30wt.%Si layer (zone 2), which was remelted 2000W and 180 mm/s. b Enlargement of Figure 8a illustrated the primary Si, α-Al, and Al-Si eutectic
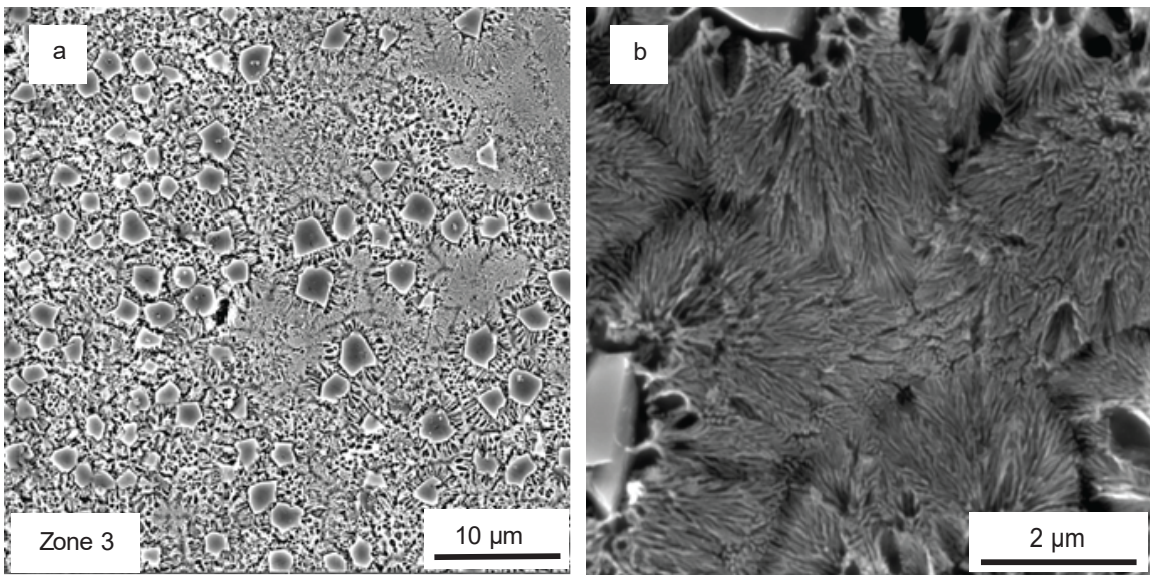
Figure 3.31 a SEM micrograph showed the microstructure Al-30wt.%Si layer (remelted zone 3), which was remelted 1000W and 180 mm/s. b Enlargement of Fig.9a showing a fine eutectic and primary Si.
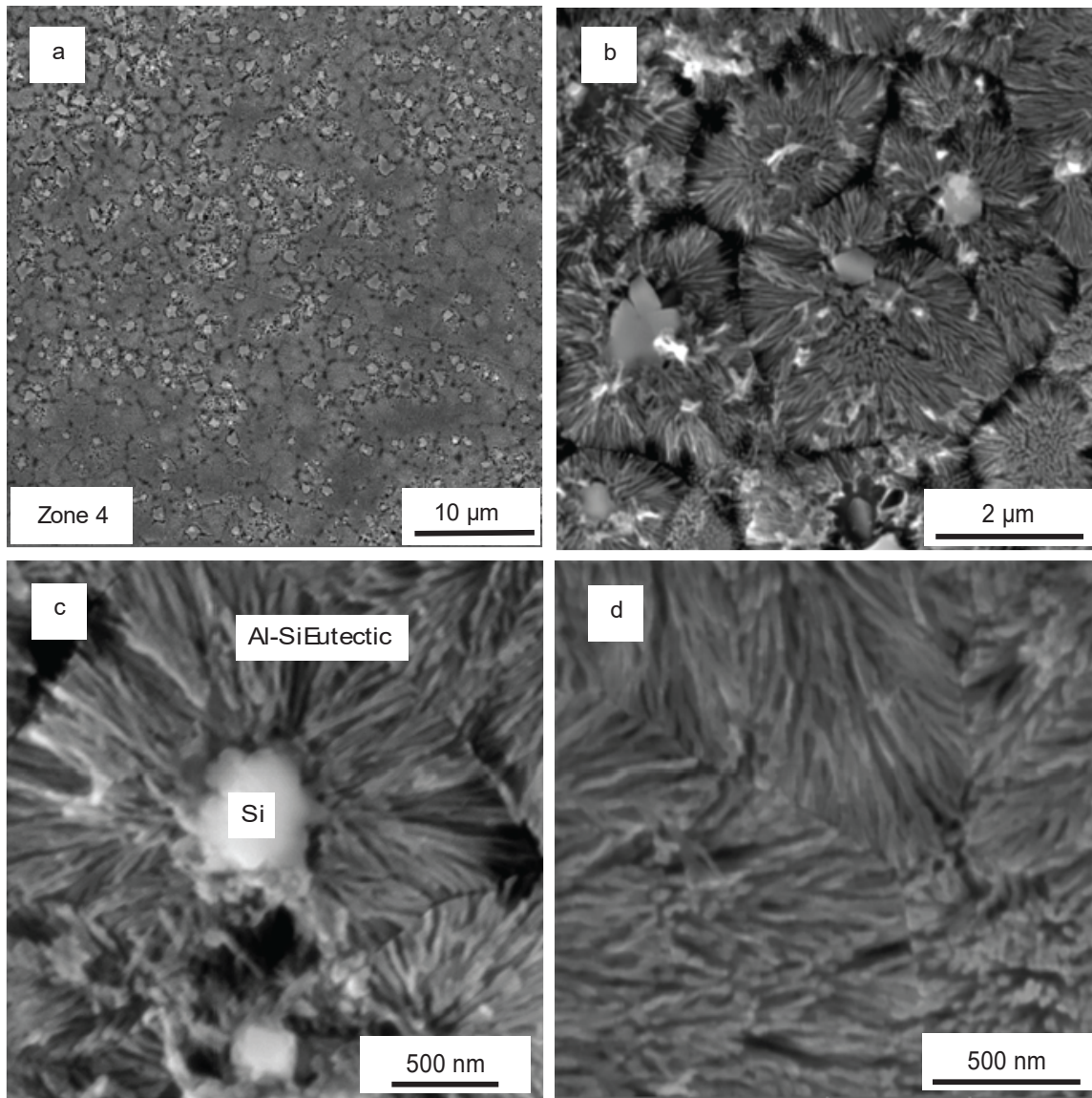
Figure 3.32 a-d SEM micrographs showed the microstructure of remelted zone 4 of the Al-30wt.%Si layer at different magnifications. The tracklayer, which was remelted at the lowest power (800W) and fast speed (180 mm/s) showed a decrease in the quantity and the sizes of the primary silicon crystals and a dramatic increase in the quantity of the nanofibrous eutectic.

TEM analysis

TEM study at different regions in the remelted Al-30 wt. %Si layer showed that the primary silicon crystals and the eutectic silicon contained a high density of parallel twins, while the α-Al phase contains dislocations and ultrafine twinned particles (Figure 3.33(a-d)). The twins in the primary Si crystals were parallel and had different directions with spacings ranging

84

between 5 and 20 nm (Figure 3.33 (b)). The eutectic silicon exhibits different morphologies. Figure 3.34(a,b) shows worm-like Si particles of different lengths nucleated and growing in the α-Al cells/dendrites in addition to the nano-sized Si crystals, which precipitated during cooling to room temperature. Figure 3.35(a,b) shows Al-Si eutectic silicon of nanosized fibrous morphology. It is apparent from the figure that as the laser remelt power is reduced, the eutectic size and spacing become much finer. The fibrous eutectic in zone 4, which experienced the highest cooling rate showed the smallest spacing of approximately 10 to 15 nm. TEM examination revealed a high density of parallel twins extended along the length of the silicon fiber (Figure 3.33(b)). This observation supported the twin plane re-entrant edge (TPRE) theory that the formation of twins accelerates the growth of the eutectic silicon since silicon growth occurs more readily at the re-entrant edge [2].
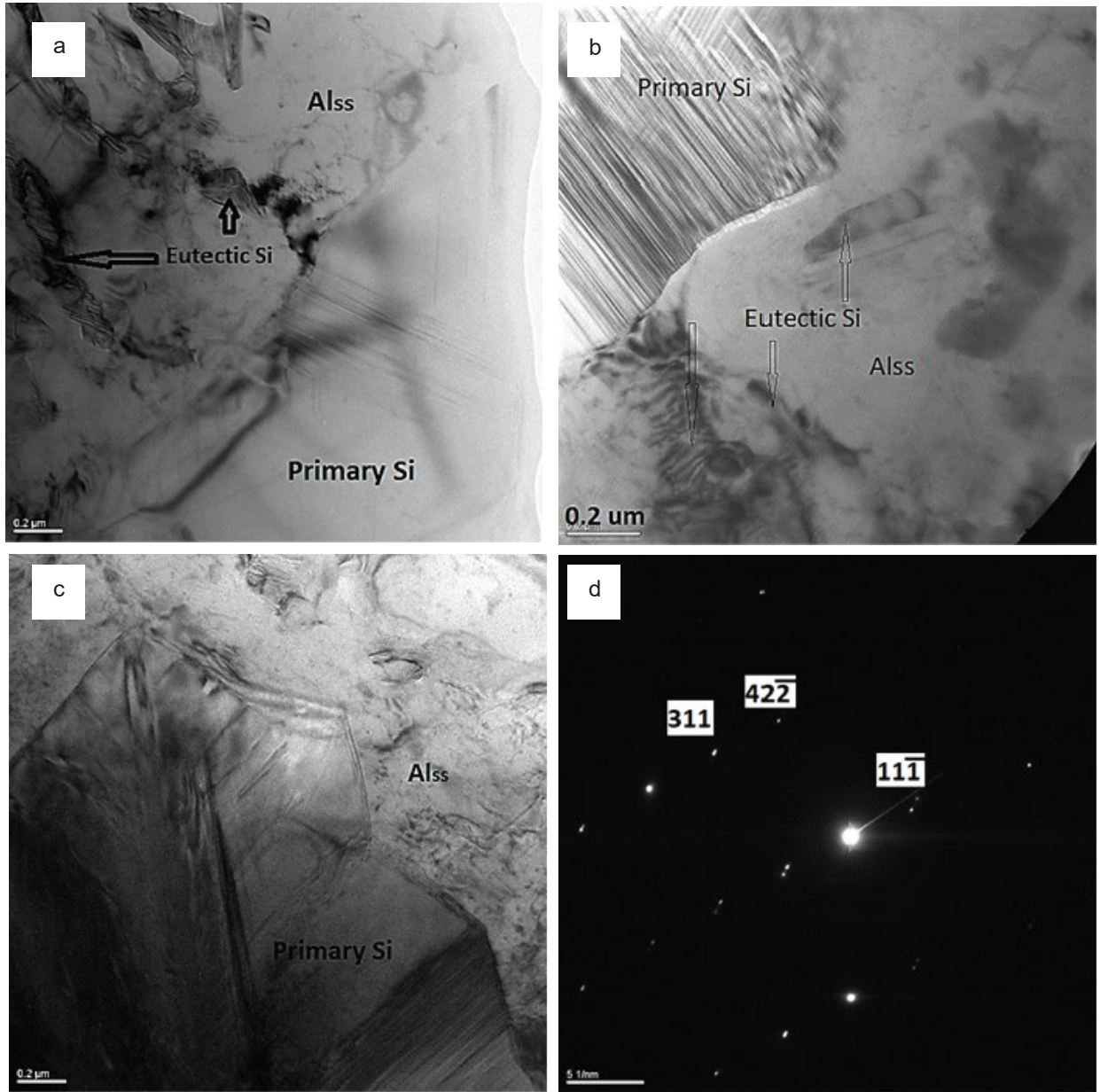
Figure 3.33 a-c TEM micrographs were taken from the least cooled Al-30wt.%Si alloyed layer (zone 2) showing primary Si crystals contain multiple twins, eutectic Si, and α-Al. d SADP was taken from primary silicon, which is shown in Figure11b, zone axis is [121]. The spot splitting is consistent with internal twinning.
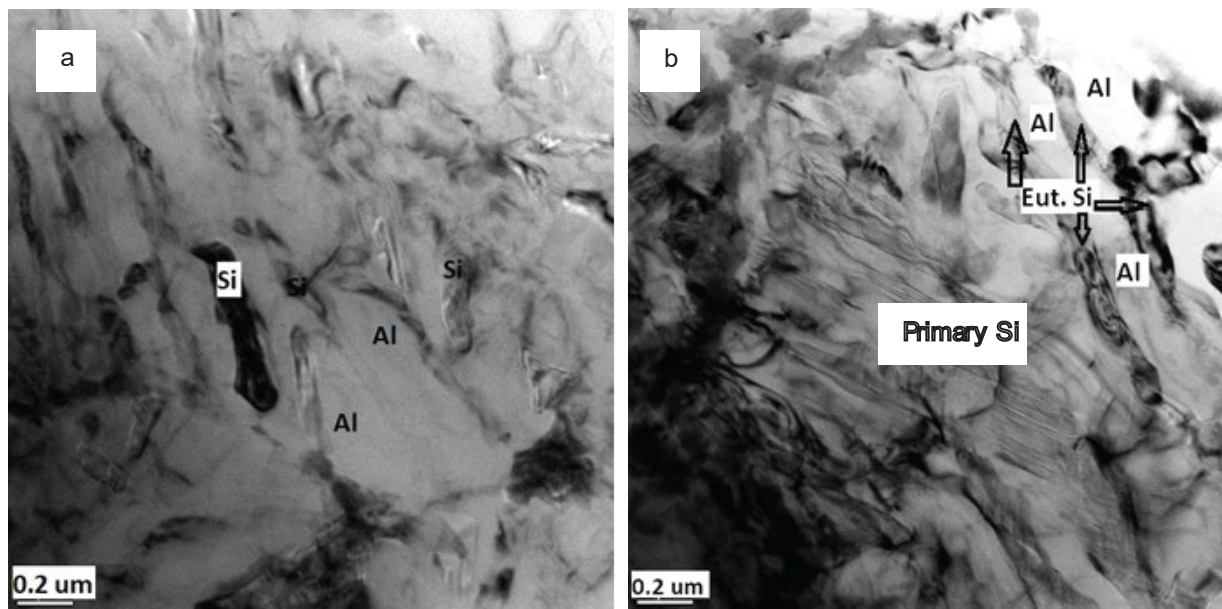
Figure 3.34 a-b TEM micrographs were taken from the Al-30wt.%Si alloyed layer, laser remelted at a scan speed of 180 mm/s, and power 2000W (zone 2 in Fig.7) showing worm-like silicon particles of different lengths within the α-Al cells or dendrites.
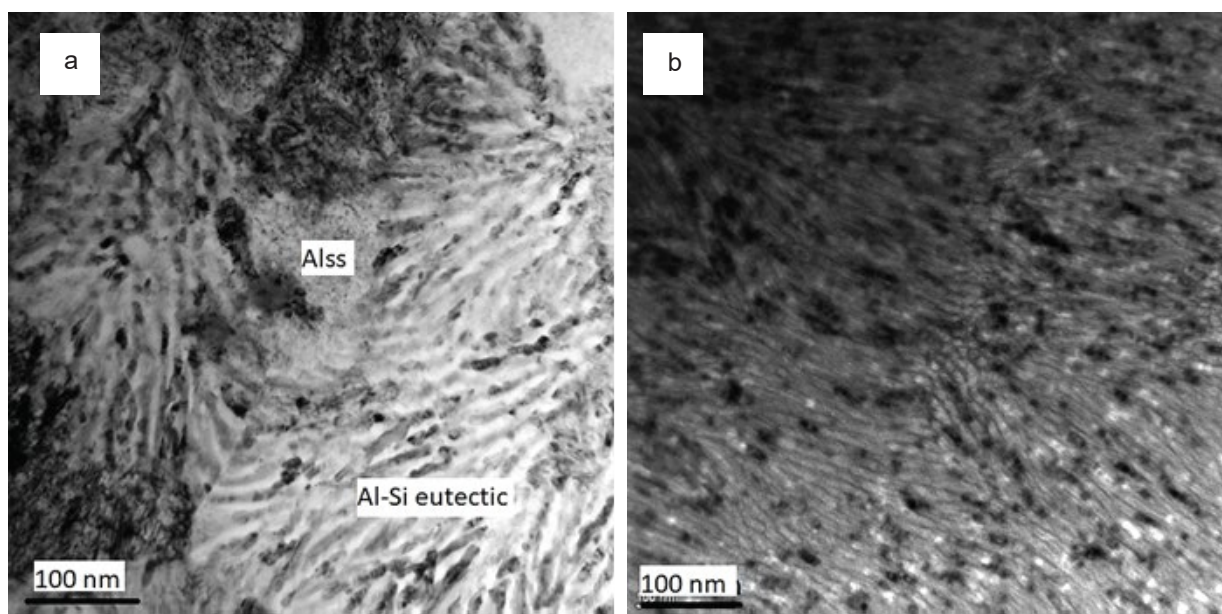
Figure 3.35 TEM micrographs show the nanosized fibrous Al-Si eutectic in Al-30wt.%Si alloyed layer laser remelted at a scan speed of 180 mm/s and powers, a 1000W (zone 3, Fig.7). b 800W (zone 4, Fig.7). As the laser power is reduced, the Al-Si eutectic becomes much finer.

3.3.3.3 Cooling Rate

It is known that in laser melting at different heat inputs, as the melted depth decreases, the cooling rate increases, which, in turn, leads to a large undercooling in the smallest depth and produces a fast growth rate. In this study, the cooling rate for Al-Si alloyed layers was calculated using what is known as the Eagar-Tsai approach, which is based on the Rosenthal model [51], [104]. The model is based on conduction and considers the laser heat input as a Gaussian area, which is more realistic than the point-input approach. Thermo-physical properties of the Al-Si alloys were kept constant and calculated through the mixing of mass percent for different alloys. The solution for the Rosenthal equation is only possible with numerical integration. Additionally, discretization of an area of interest (in other words, laser material interaction region) is a must. These requirements increase the computation significantly. Therefore, it was submitted to a workstation after defining the boundary conditions, and input values are thermophysical properties of Al and Si [90] and laser processing parameters. To reduce the computation time, the discretized matrix was solved 10 times, each of which with 0.01 ms time increment. Upon completion, heat history and time steps were used for cooling rate calculations. Results are shown in Table 3.6

Table 3.6 The overall effect of the laser rapid remelting at different powers or heat inputs (P/v) on the melted depths, average cooling rates, Si sizes, and eutectic spacings of the Al-25wt.%Si and Al-30wt.%Si alloyed layers.

Laser track layer	Laser processing parameters			Location	Remelted depth µm	Average cooling rate °C/s	Si size µm	Spacing λ, nm
	Power W	Speed mm/s	Heat input J/mm					
1A Al-25Si	2000	10	200	Zone 1	500	4.5×10^3	6-8	50
	2000	180	11.11	Zone 2	250	6.9×10^4	3-5	30
	1000	180	5.5	Zone 3	150	7.1×10^4	1-2	20
2A Al-30Si	2000	10	200	Zone 1	600	4.6×10^3	3-6	150
	2000	180	11.11	Zone 2	300	7.1×10^4	2-3	50
	1000	180	5.5	Zone 3	150	7.6×10^4	1-3	25
	800	180	4.45	Zone 4	70	9.0×10^4	0.5-2	10
	600	180	Partial melting	-----	---		---	-----

Figure 3.36(a,b) showed clearly that increasing the cooling rate caused a great reduction in the sizes of the primary Si and the eutectic spacing to a nanoscale. Although the two curves have the same trend, the decrease in the eutectic spacing is much steeper, especially at the highest cooling rate. This can be seen more clearly in the TEM micro-graphs in Figure 3.35(b), which showed a significant decrease in the eutectic spacing to approximately 10–15 nm at the highest cooling rate.
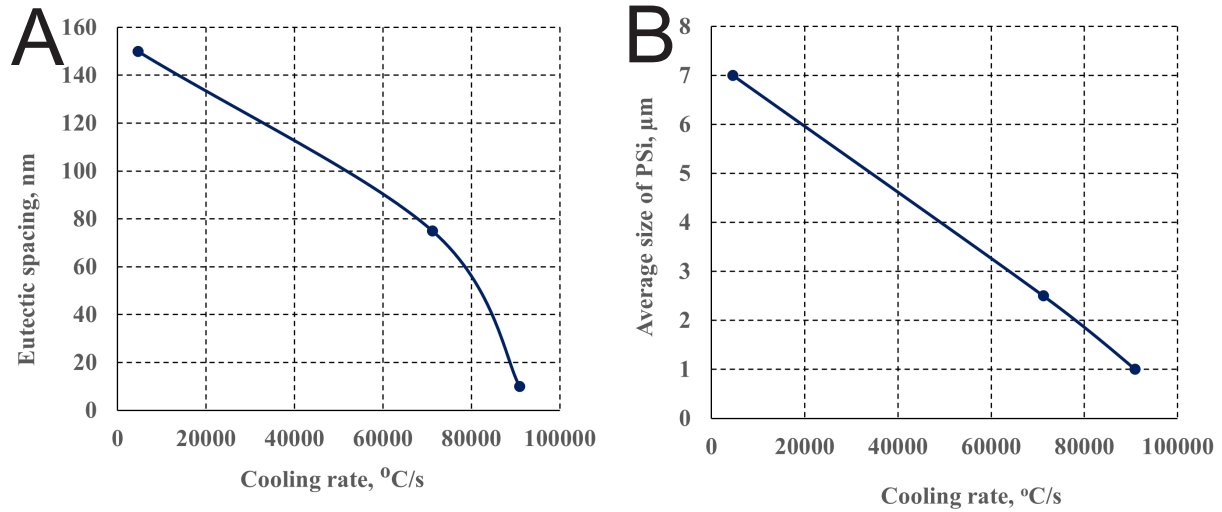
Figure 3.36 A Variation of the eutectic spacing with cooling rate, B variation of the primary silicon size with the cooling rate for Al-30wt.%Si alloyed layer laser remelted at different heat inputs.

3.3.4 Discussion

Results of the laser rapid remelting of the Al-25 wt. %Si and 30 wt. %Si alloyed layers, which were processed at relatively lower laser powers and a higher scan speed, showed the potency of the cooling rate not only in the refining of the silicon size but also in reducing the quantity of the primary Si crystals, decreasing the amount of the aluminum dendrites, and also triggering the eutectic Si to nucleate heterogeneously from the primary silicon phase and branched out of it. Furthermore, the increase of the cooling rate caused a shift in the eutectic composition towards a high silicon content reaching 20 wt. %Si or slightly more, which is far more than the value reported in the Al-Si equilibrium-phase diagram (12.6 wt. %Si). In the present results, the microstructure of the fabricated and the remelted layers are hypereutectic and consistent with the Al-Si phase diagram, but with great refinement in the scale of all the phases (primary Si, α-Al, and eutectic Si). Solidification of Al-25 and 30 wt. %Si alloyed layers at cooling rates commences with the nucleation of the primary Si nucleus. Once the Si nuclei form, it grows by rejecting aluminum atoms and accumulating them around the vicinity of the silicon

90

crystals, causing undercooling in the surrounding area and leading to the nucleation and growth of the aluminum dendrites around the primary Si. Upon further cooling, the aluminum dendrite continues to nucleate and grow rapidly by rejecting Si atoms on both sides of the dendrite. When the temperature reached the eutectic, the remaining liquid solidified forming an Al-Si fibrous eutectic. The final solidified microstructure contains a high amount of aluminum dendrites, which upon further cooling to room temperature, begins with the precipitation of nano-sized silicon particles. The solidification path will follow this sequence, L → primary Si. + L, L → primary Si + (Al around the primary Si) + L, L → primary Si + Alden. + L, L → primary Si + Al + Eutectic. (Al+Si). Due to the high thermal conductivity of the Al phase as compared to the Si and the slow growth of the silicon phase, the eutectic is formed by nucleation of the Al phase first, which forces the silicon atom to occupy the space between the Al dendrites. However, under a very rapid cooling condition, as in the case of the remelting of the Al-25 and 30 wt. %Si layers at the fastest speed and low heat input, the highest cooling rate led to a reduction in the amount of aluminum that formed around the primary Si crystals, which acted as a nucleus for the growth of the eutectic aluminum phase and this will trigger the eutectic silicon to grow quickly upon the underlying solidified zone of primary Si + eutectic and spread massively in different directions forming a radiant rose.

On the other side, observations by the TEM micrographs at higher magnification demonstrate that most of the primary silicon contains parallel and multiple twins, which have a major contribution to the rapid growth of the eutectic silicon. These results are consistent with the TPRE mechanism [2], which indicates that twins influence the growth and cause the branching and twisting of the Si fibers. The formation of heavily twinned Si fibers is reported by many researchers. Nogita *et al*. [47] have reported higher twin densities in the modified than the

91

unmodified alloy and twins catalyze crystal growth leading to the formation of complex and more faceted morphology. Another factor that made the silicon phase twin easily is the low stacking fault formation energy of the silicon [105].

3.3.5 Conclusions

(1) Hypereutectic Al-%Si alloyed layers with nanoscale structures were fabricated on the surface of a commercially pure aluminum substrate by laser melting technique at controlled laser processing parameters.

(2) The average silicon contents of the produced Al-Si layers were 25 wt.% and 30 wt. %Si and the microstructure was heterogeneous and composed of clustering of primary Si with a size ranging from 5 μm to 7 μm, supersaturated α-Al cells/ dendrites, and fibrous Al-Si eutectic.

(3) By laser rapid remelting technique utilizing a fast scan speed (180 mm/s) and low powers (800 W), a greater structural refinement was achieved as the size of the primary silicon particles was reduced to less than 1 μm as well as the fibrous eutectic spacings were decreased to approximately 10–15 nm.

(4) The great impact of the cooling rate is not limited to the refinement of the silicon phase and a reduction in the eutectic spacing but rather in the great reduction in the quantity of the α-Al dendrites and increased the proportion of the nanofibrous eutectic substantially. It also triggered the Si eutectic to grow rapidly adjacent to the primary Si templates and spread massively throughout the melted zone.

(5) The nanoindentation hardness was inversely proportional to the Al-Si fibrous eutectic spacing, λ, reaching 3.15 GPa at the spacing of 10–15 nm.

(6) Transmission electron microscopy revealed different Si morphologies, such as block-like primary Si, worm-like Si at the boundaries of the α-Al cells, and nanoscale fibrous eutectic Si, which were internally nano-twinned.

Chapter 4 In-situ Characterization of Laser-Processed Materials

4.1 In-situ characterization of tensile behaviour of laser rapid solidified Al-Si heterogeneous microstructures

Chapter 3 elucidates the Aluminum-Silicon (Al-Si) alloys and underscores advancements in their characteristics through Laser Surface Remelting (LSR). LSR is known to significantly enhance the strength of materials [65], while concurrently inducing the formation of varied grains possessing diverse Silicon fiber orientations and structures. Notably, the mechanical attributes of bulk samples can be approximated through the analysis of numerous grains. However, in the context of material compromised by LSR processes, the characteristics are predominantly dependent on the individual grains.

The reason resides in the fact that LSR is active exclusively within a limited area, often smaller than the laser beam diameter, rendering its scalability beyond the scope of this dissertation. Thus, it becomes critically pertinent to investigate the mechanical responses exhibited by an area composed of selectively chosen grains. Such a study will unravel the intrinsic potential of laser surface remelted alloys and could potentially attract researchers' attention to exploring the processes and applications involving specific alloys.

Prior research, such as that undertaken by Gu *et al*., has scrutinized the fracture mechanisms associated with 100nm rods, utilizing in-situ methodologies [106]. Additionally, research by Ye *et al*. encompassed in situ compression testing of pillars with diameters ranging between 200 and 1600 nm [107]. Borkowski *et al* suggested a way to test single-crystals via in-

situ testings [108]. Numerous other tests such as single-point bending tests, three-point bending tests, and four-point double-clamped bending test specimens were prepared using Focused Ion Beam (FIB), the tests of which were then carried out concurrently with real-time observations [109]. Elevated temperature tensile tests, in excess of 1700 degrees Celsius, were performed on ceramic matrix composite materials, with the observations recorded using micro computed tomography (μCT) scans [110].

The execution of in-situ mechanical examinations, specifically those targeting select areas within a sample, necessitates the employment of electron microscope observations. This requirement stems from the simultaneous occurrence of material deformation during the testing procedure. The preparation of the material, tailored to the stipulated dimensions, is carried out utilizing a Focused Ion Beam (FIB).

The collaborative nature of this study involved participation from a partner based at the University of Nebraska-Lincoln, and the materials employed were produced at the University of Michigan by the proprietor of this dissertation. The methodology applied in this experimental process is comprehensively described in existing literature [85]. The results of this investigation are subsequently presented in the following section.
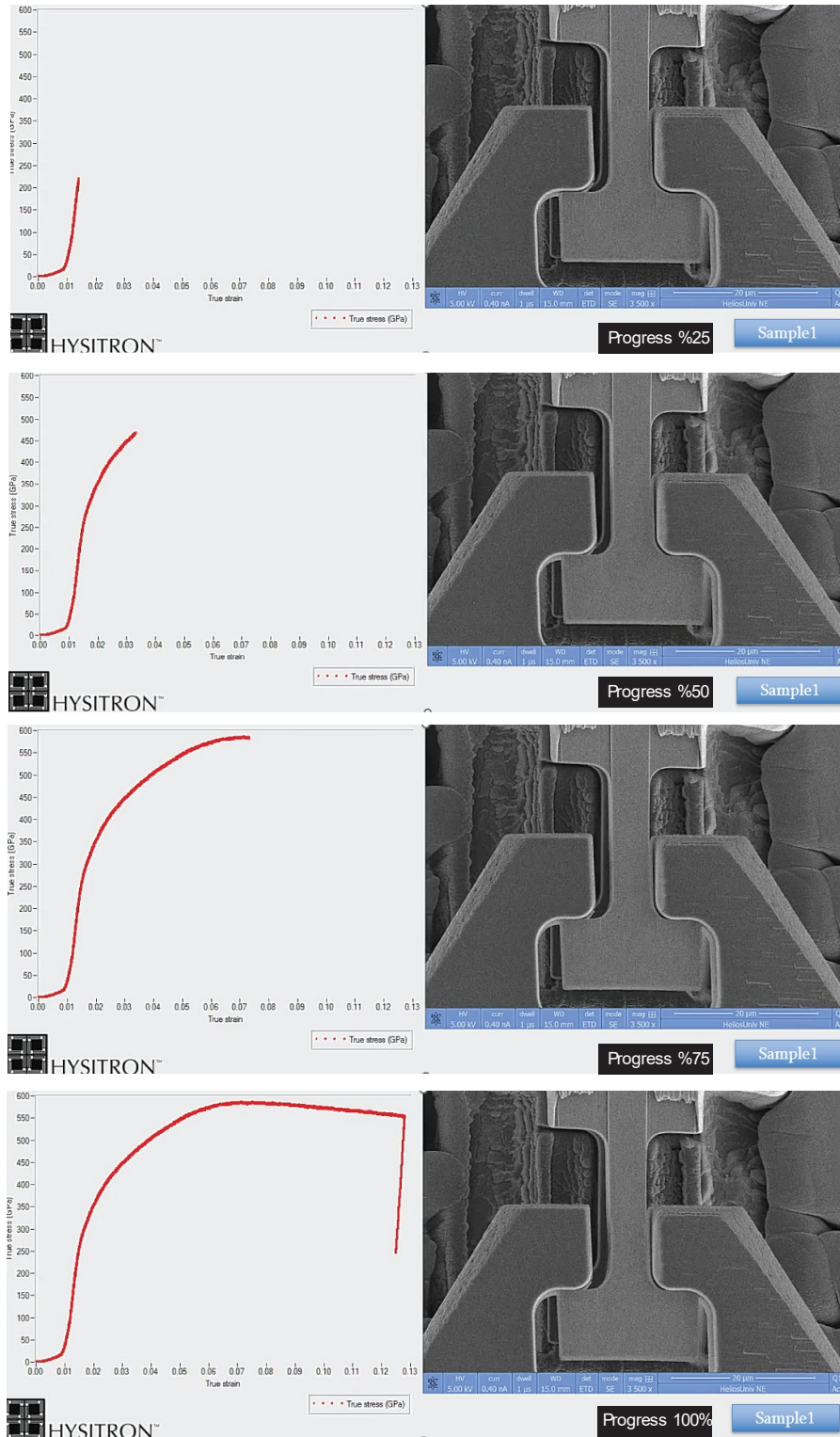
Figure 4.1 The temporal advancement of the in-situ tensile test is furnished across four distinct time intervals. Notably, this testing procedure abstains from inducing failure, enhancing the capacity for in-depth deformation examination[85].
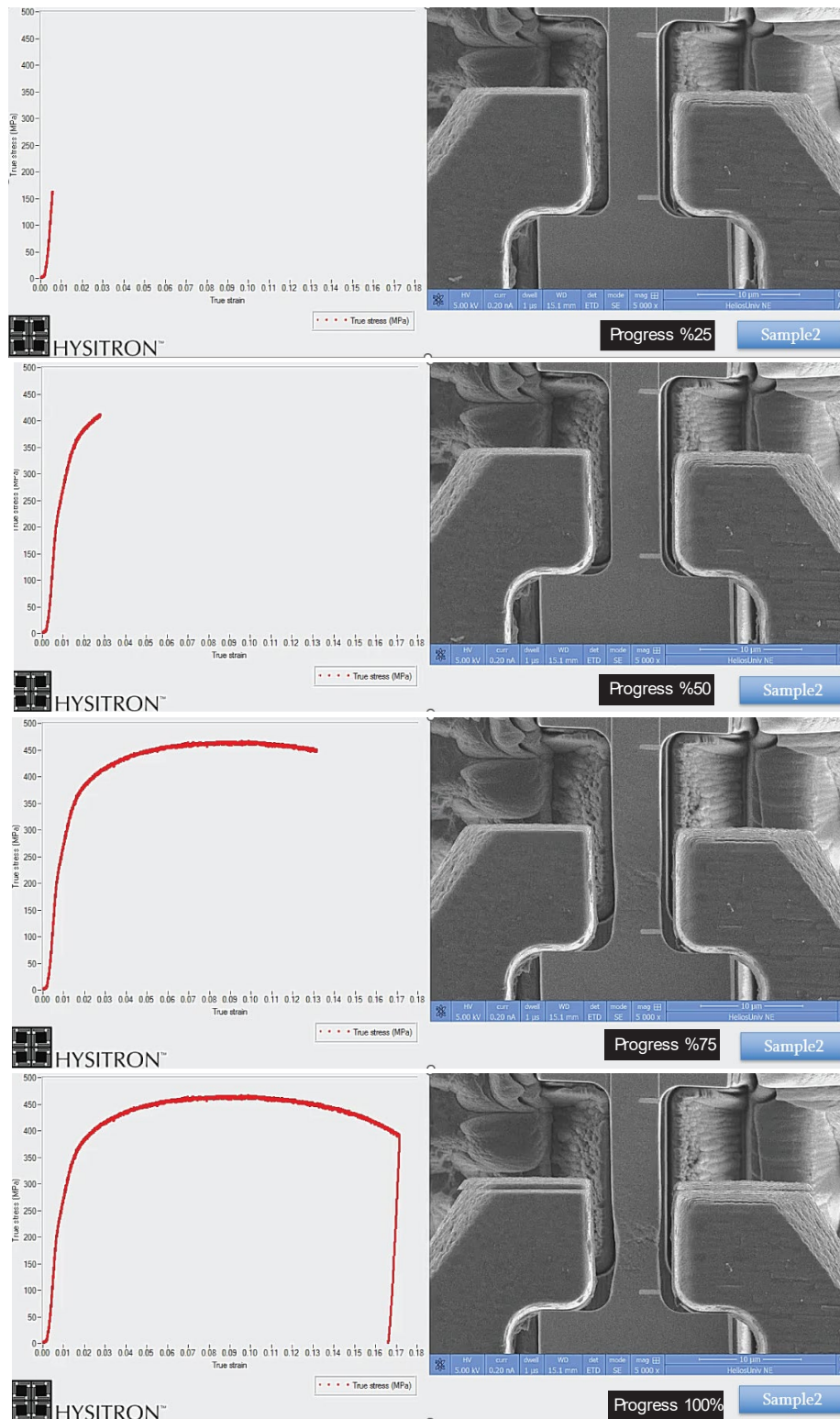
Figure 4.2 The in-situ tensile test was executed in a sequential manner, with experimental data documented at four different time increments. However, in this particular testing scenario, the experimental specimen was subjected to conditions designed to induce failure, lending crucial insights into its mechanical characteristics and failure mechanisms[85].
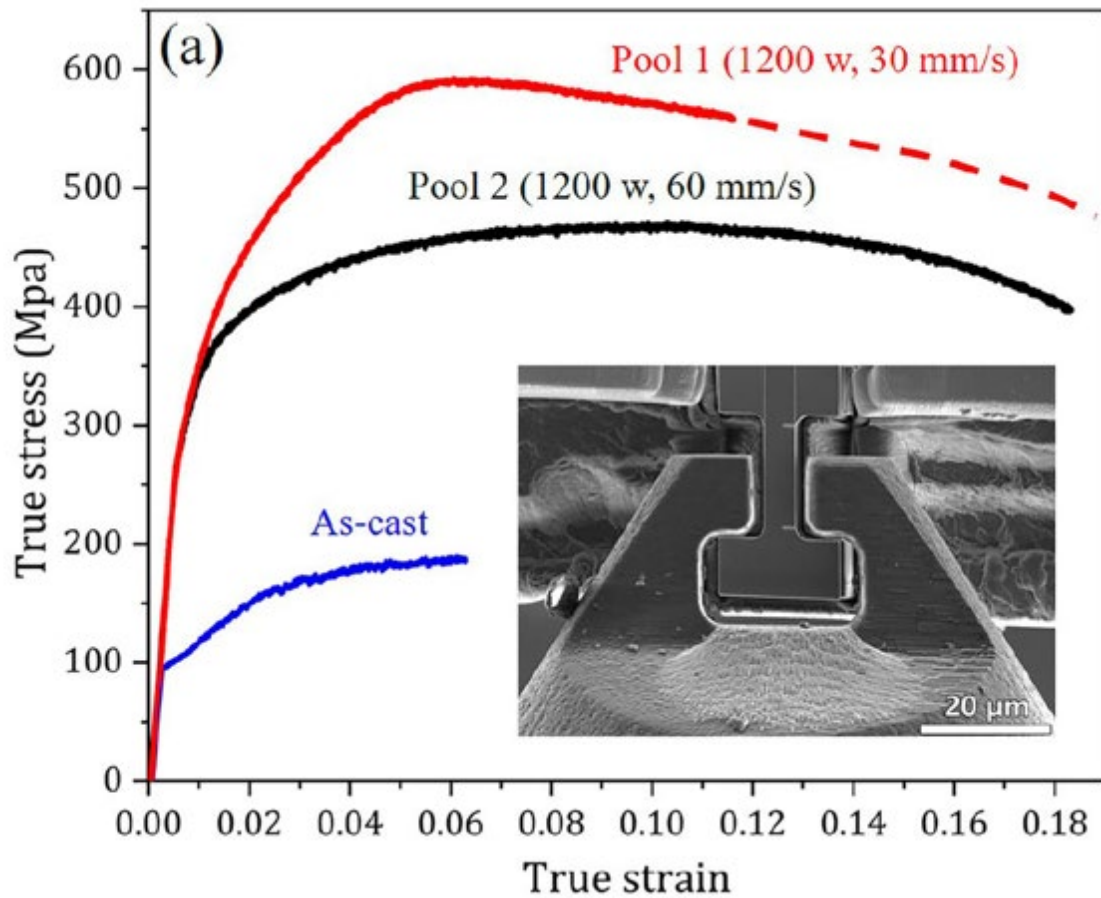
Figure 4.3 A summary of the comparison of Test1, Test2, and the as-cast region is shown[85].

The aforementioned figure serves as a reliable benchmark for evaluating the influences of Laser Surface Remelting (LSR). An enhanced level of performance is observed in the tested specimens within the laser-affected zone, as compared to their counterparts prepared from the as-cast region. This superior performance is evident across yield strength, elongation, and toughness variables.

It is pertinent to mention that within the materials science domain, strength and elongation typically exhibit a trade-off relationship. An augmentation in one usually compromises the other, suggesting an inherently inverse correlation. The simultaneous enhancement of both these properties is distinctly atypical and is highly advantageous toward the enrichment of material quality and utility. Therefore, this novel observation infers significant implications for material science and engineering.

4.2 In situ optical emission spectra and μCT fast quality analysis of DMD

4.2.1 Introduction

Originating in the 1980s, metal additive manufacturing, despite its persisting designation as an emergent technology, has made significant strides in the field of manufacturing sciences. Excellent materials research apparatus, a great way of prototyping, and outstanding design realization are the three fundamental points of that new method. However, its capabilities have been hindered by some problems; huge initial investment[111], the requirement of high-skilled human sources, and slow throughput time. The latter brings about quality assurance problems as well. Destructive tests become unaffordable and non-destructive tests are limited due to their nature[112].

Directed Metal Deposition (DMD) is known as a subbranch of metal additive manufacturing. Compared to the most common technique, powder bed fusion; it provides some flexibility in build rate and mixing of the powder in different amounts during the printing process. Also, due to its requirement for a gantry system to move the deposition head in the build envelope, it is possible to add on some instruments to supplement the production, especially the monitoring systems. Examples would be optical emission spectroscopes, contact

(thermocouples) or non-contact (pyrometers) temperature sensors, high-speed cameras, metrology sensors, and even secondary machining heads.

Optical spectroscopy incorporates different techniques to study the interaction of matter with light. We consider two processes occurring when a light beam interacts with a sample: absorption or emission. Various information about the sample target material can be obtained by analyzing the amount of light absorbed or emitted. The type of interaction between the light and the sample depends on the wavelength and intensity of light and how the light beam affects the atoms (or molecules) in the sample. A brief illustration of the absorption and emission processes in atoms is given in Figure 4.4 below. Since all of the atoms have unique ionization energy, the absorption or emission from them can be used for identification, like a fingerprint of a certain element.
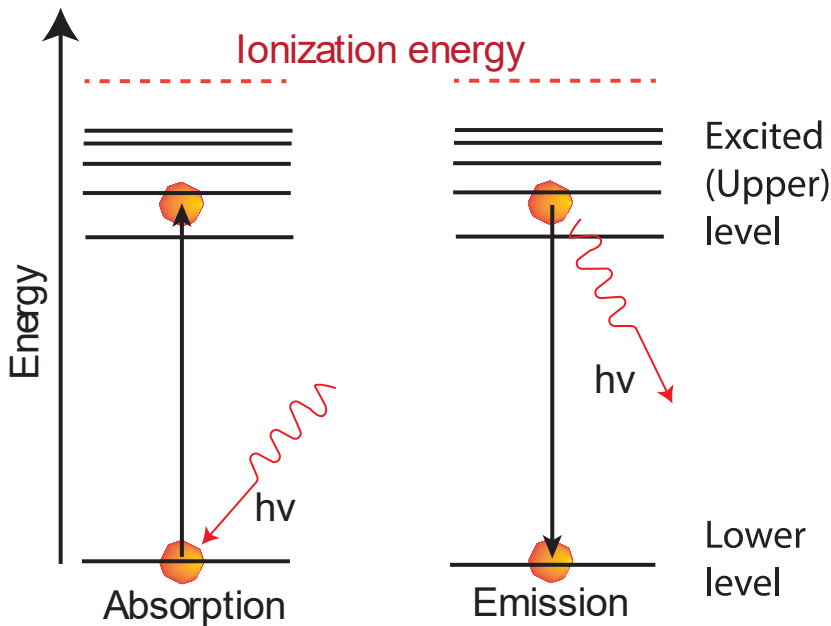
Figure 4.4 The concept of absorption and emission of a photon

Essentially, the emission spectrum is an outcome of the interaction between lasers and matter. In the Direct Metal Deposition (DMD) process, plasma formation takes place

approximately 2-5mm above the deposition surface. Although plasma is essentially a by-product, it can provide useful information when observed and analyzed. Song and Mazumder investigated the composition of chromium and iron, with varying mixture ratios. Then, these mixtures were deposited utilizing DMD, powered by a CO_2 laser. The data from these spectrum signals was used in creating a calibration curve. In 2010, they reported the calibration curve for the aforementioned elements and their 2012 research took it a step further by identifying the final chromium (Cr) percentage in the deposition of H13 tool steel [71], [72]. More recently, Wang and his team conducted research on another commercial steel called AlSl4140, where they meticulously examined the line intensity analyses of iron (Fe) and chromium (Cr).

Mazumder *et al* studied the line intensity ratios for Ti-Fe, Ni-Al, Ni-Ti, Fe-Cr, and Ni-Fe. To get rid of the baseplate's effect, they deposited 5 layers of these mixtures, and the data collection was not started until the beginning of the third layer. While the line intensity ratio for an element is linear with the increasing/decreasing composition ratio, the deviations were observed when there was a phase change. This is important because the final property of the material is also dependent on the phase change. Additionally, phase change may occur within the same composition. So, it could be insensitive to any composition measurement technique in optical emission spectroscopy. [73]

In this work, we first identified the parameter sets to be deposited. Then, the plasma was observed for optical emission spectra with the help of the SOMS toolbox and software. After the metal printing, ex-situ microcomputed tomography (μCT) data was collected for the deposited beads. The revealed pores from these images were correlated with the signals with different wavelengths and different time steps. Their respective relationships are presented in the

following sections. The correlation is aimed to be quite fast (depending on CPU power, but less than 10 milliseconds) at the expense of rudimental signal processing.

4.2.2 Material and Methods

4.2.2.1 Powder

Al 7075 powders were supplied by a vendor for this experiment. Upon receiving, it was inspected under SEM to validate the specifications. In this specific example, we aimed to use a mixture of spherical and non-spherical powders, because we wanted to induce some defects in the final deposition to inspect them later. Here sphericity is obtained by height to width ratio of individual powder. While the aspect ratio is different than the value of 1, it shows a non-spherical characteristic. Figures below are for better explanations:
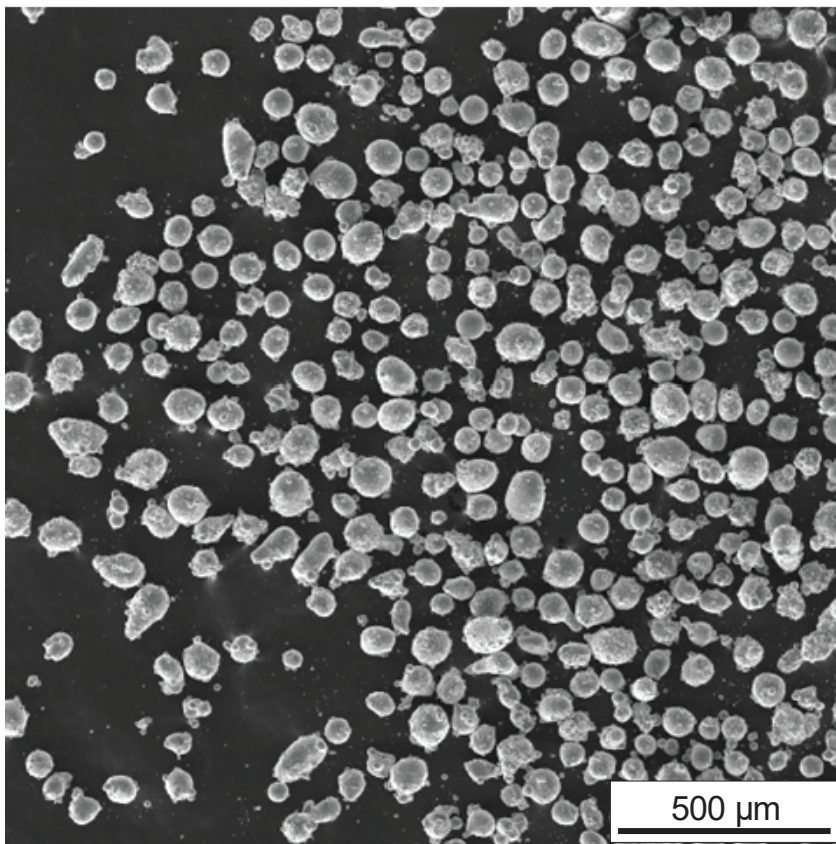
Figure 4.5 Al 7075 powder under SEM. Non-spherical and satellite features can be observed.
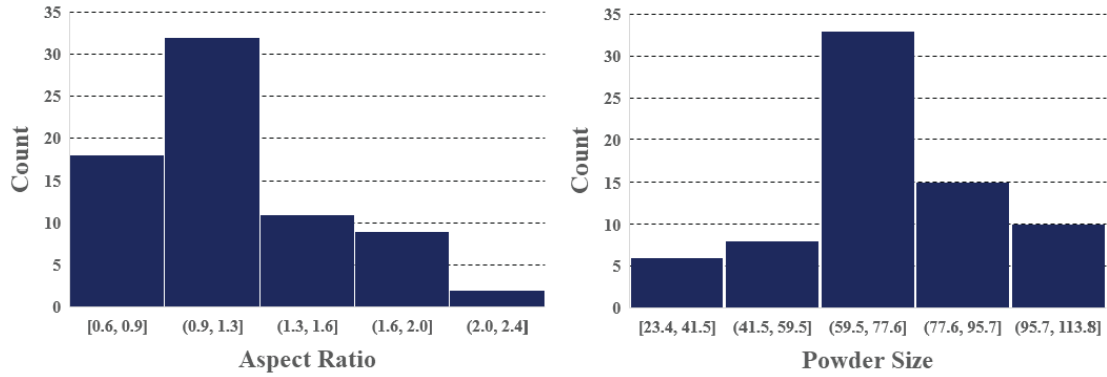
Figure 4.6 Al 7075 powder aspect size (width to depth ratio) and powder size distribution

4.2.2.2 DMD setup

Metal deposition experiments were carried out at the University of Michigan's Claim lab. Using the existing knowledge of metal additive manufacturing, the experiment parameters were identified carefully so it would return both good quality and bad quality parts. The final shape is a single line to reduce the complexity of the analysis (Figure 4.7). Metal deposition experiments were done using our custom-made DMD system. The specifications of the overall system can be found below.
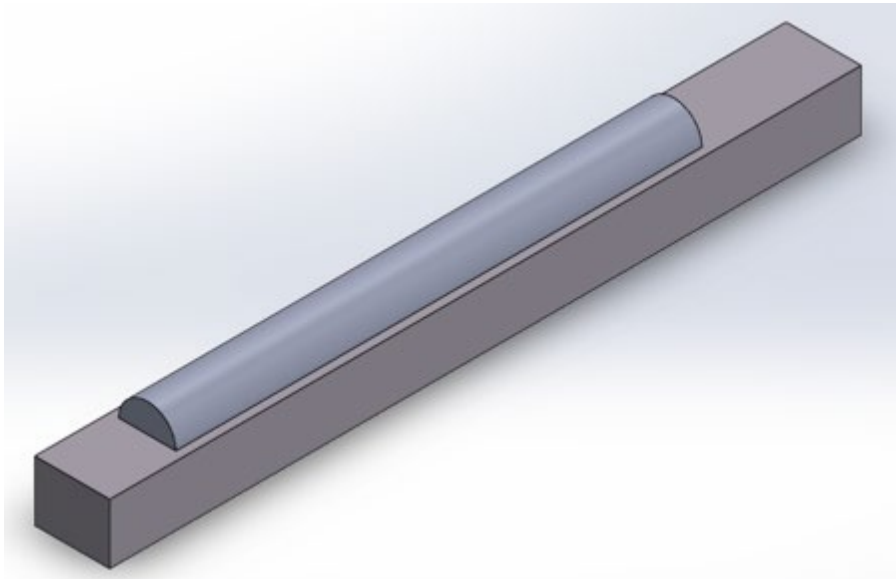
Figure 4.7 Illustration of a DMD strip

- **Laser**:

  - Trumpf HLD 4002

  - 4000 W maximum power

  - Yb:YAG – 1030 nm

  - BPP 8mm.mrad

  - Effective laser diameter range: 0.6-1.5 mm (0.02 – 0.06 inches)

- **Powder Deposition**

  - 3 Different powder cannisters

  - Adjustable DC motor shaft driven

  - Usage of delivery gas to enhance powder flow

- **Gas**

  - Adjustable shielding gas

  - Adjustable delivery gas

  - Adjustable purging gas to protect optics

- **CNC Machine:**

  - Build Volume

    - Width: 30 cm ($\approx$ 12 inches)

    - Depth: 20 cm ($\approx$ 8 inches)

    - Height: 10 cm ($\approx$ 4 inches)

  - Deposition speed range: 1-5 mm/s (0.05-0.2 ips)

- **Attachable External Sensos**:

  - High speed CCD camera

  - Optical emission spectra collector

- o Pyrometer

- o Thermocouple

- **Control Environment**:

  - o National Instruments USB6343

  - o Windows Desktop
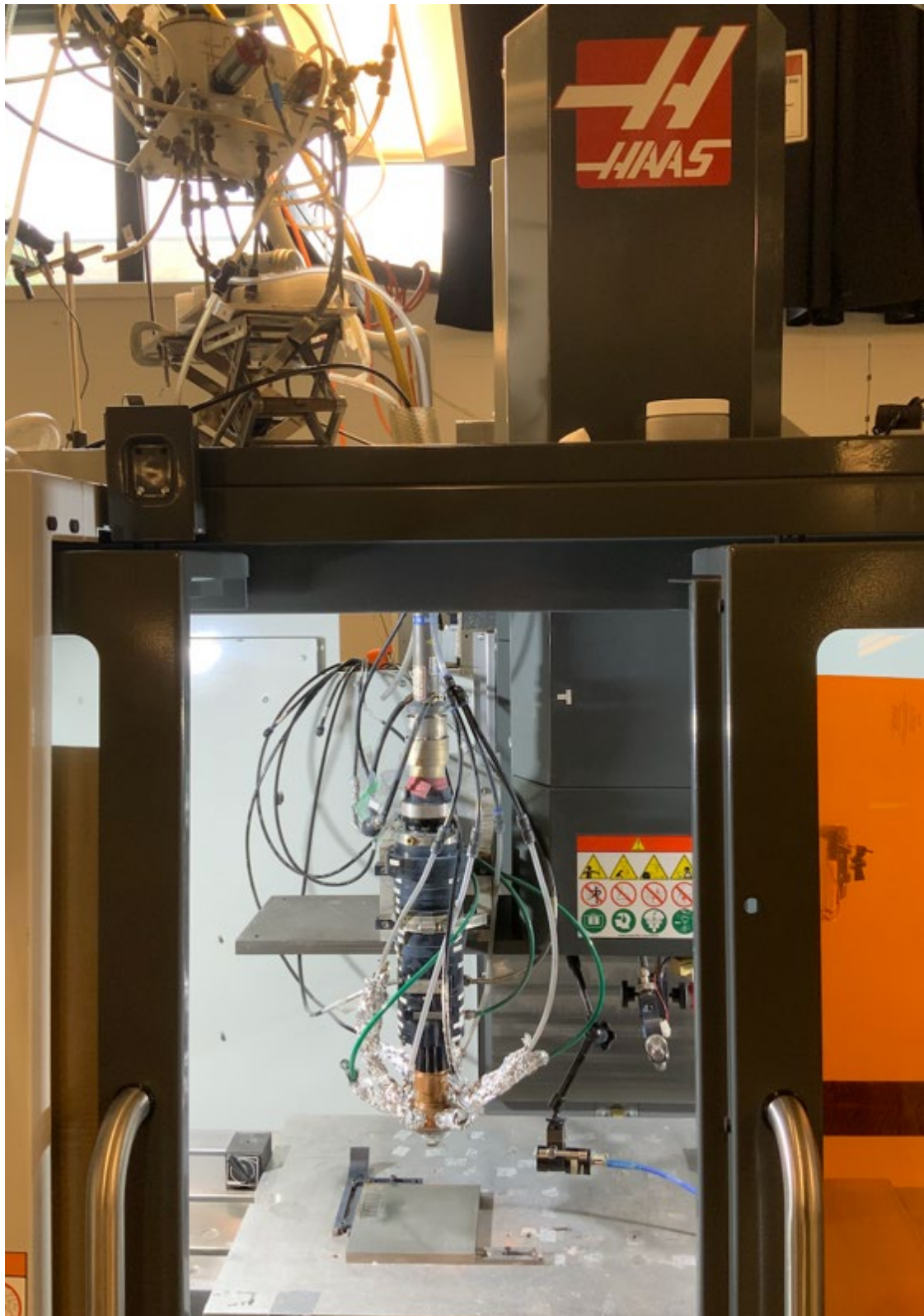
Figure 4.8 Overall DMD system
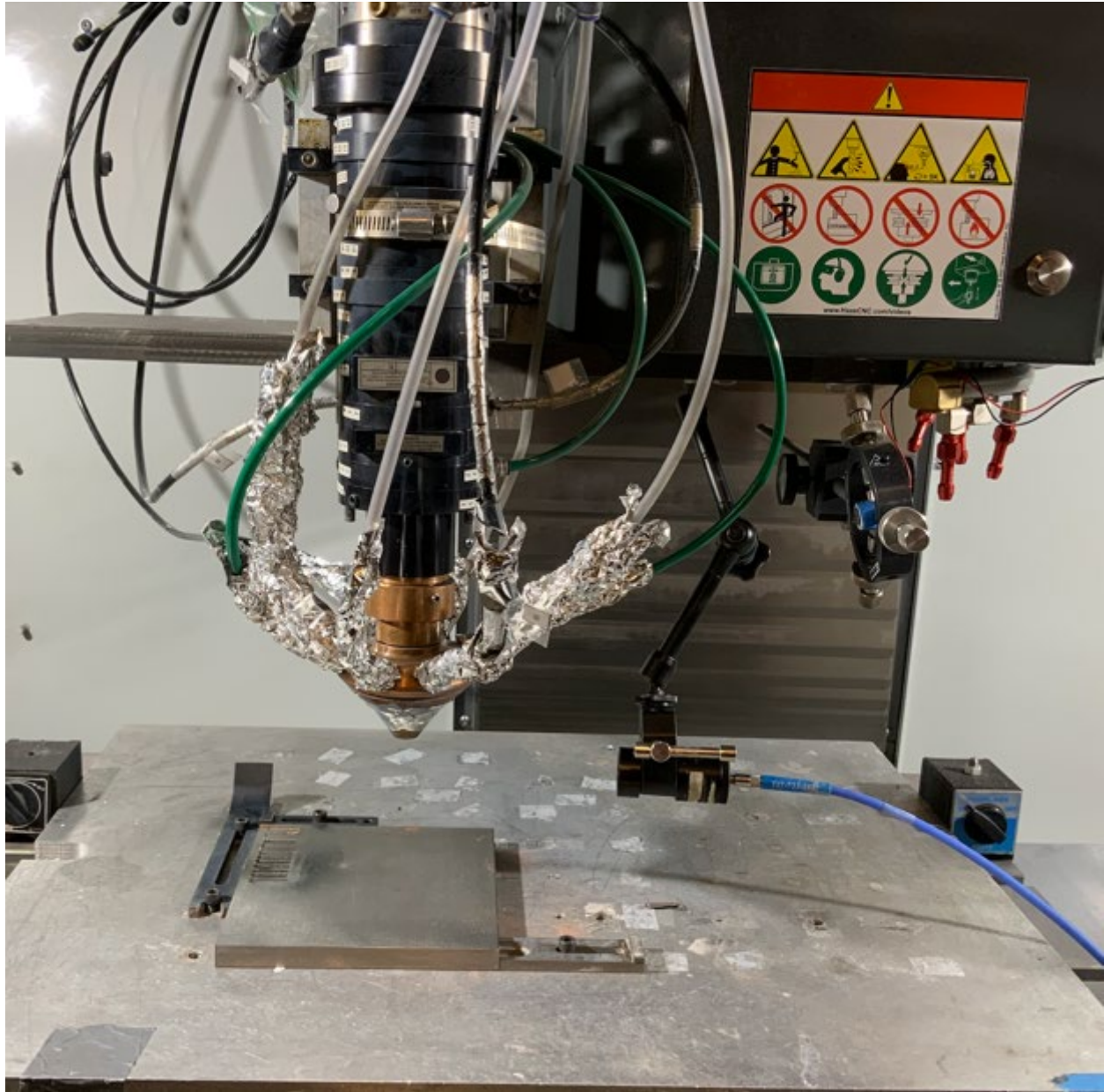
Figure 4.9 Close-up photo of DMD nozzle and position of the collimator optic

As previously mentioned, I have designed experiments for this project to create both high quality and poor-quality parts. This approach is expected to be beneficial in distinguishing one dataset from another. We have leveraged the knowledge from the Claim lab to develop our plan. Next, Table 4.1 presents the conditions for the experiment. We maintained a consistent scanning path across all experiments, adhering to a forward-backward-forward pattern.

With repetition and variation in parameters, a total of 39 experiments were conducted in the initial run. Upon inspection by eye, 10 of them were found to be worthy of further characterization (marked by a yellow circle in Figure 4.10).

Table 4.1 DMD experiment parameters

Experiment	Laser Power (Watt)	Scanning Speed (mm/s)	Laser Beam Diameter (mm)	Powder Flow Parameter (Volt)
1-10	1400-2250	3.81-5.35	1-1.15	1.5-6

Figure 4.10 All of the deposited strips and qualified ones with a yellow marker for further studies

4.2.2.3 Spectrometer Setup

The spectrometer, which we will use for this project, has an entrance aperture of 10-micron width, a holographic UV/VIS grating with a groove density of 1200 per millimeter, and a 2048-element CCD-array detector. The resolution of the spectrometer is 0.05 nm.

As for this project, the time interval to capture data is 10 milliseconds. Spectrometry will be initiated right before the deposition and turned off at the end of the experiment manually. Upon completion, the start and end time will be identified by the intensity of the signal and unnecessary entries will be cleaned before starting the analysis. In this setup, the collimator lens observes the light-material interaction from 5mm above the baseplate, where the signal is thought to be strongest. Since the collimator was fixed to the DMD head, spatial variance of the spectral signals was kept minimum. The captured data for just one time frame can be seen in the following Figure 4.11
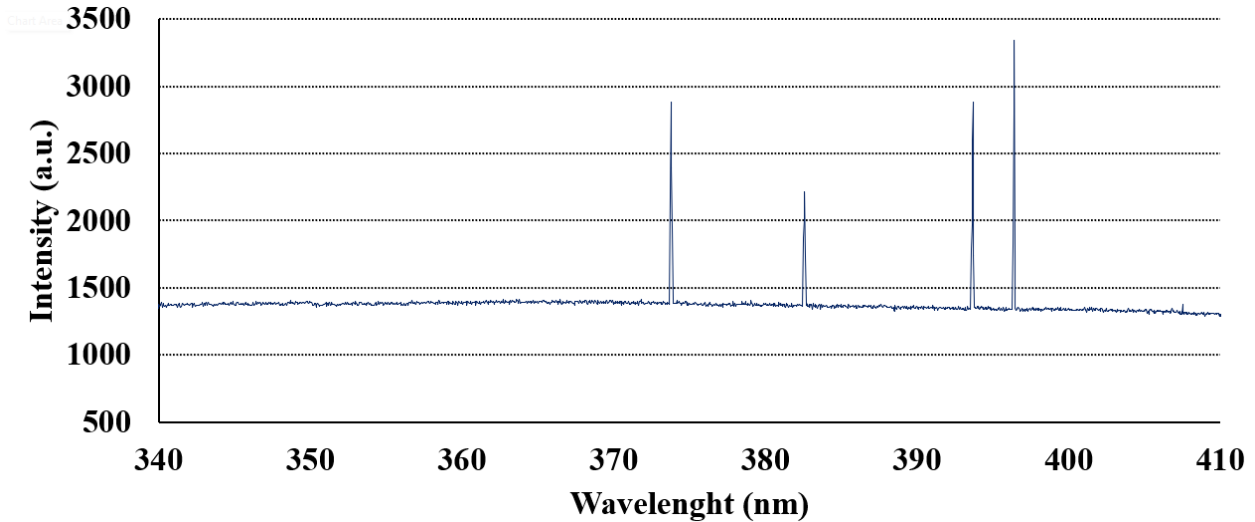
Figure 4.11 A spectra frame per defined time-step

4.2.3 Results and Discussion

The deposited material underwent a μCT scanning procedure to check the quality. If there is a void formation within the molten zone, it is considered 'Defective' irrespective of its size. This characterization was completed with help from the Michigan Characterization Center

109

(MC^2). Though the original file was received in a movie format, the individual frames for readers

of this dissertation are given in the below figure:
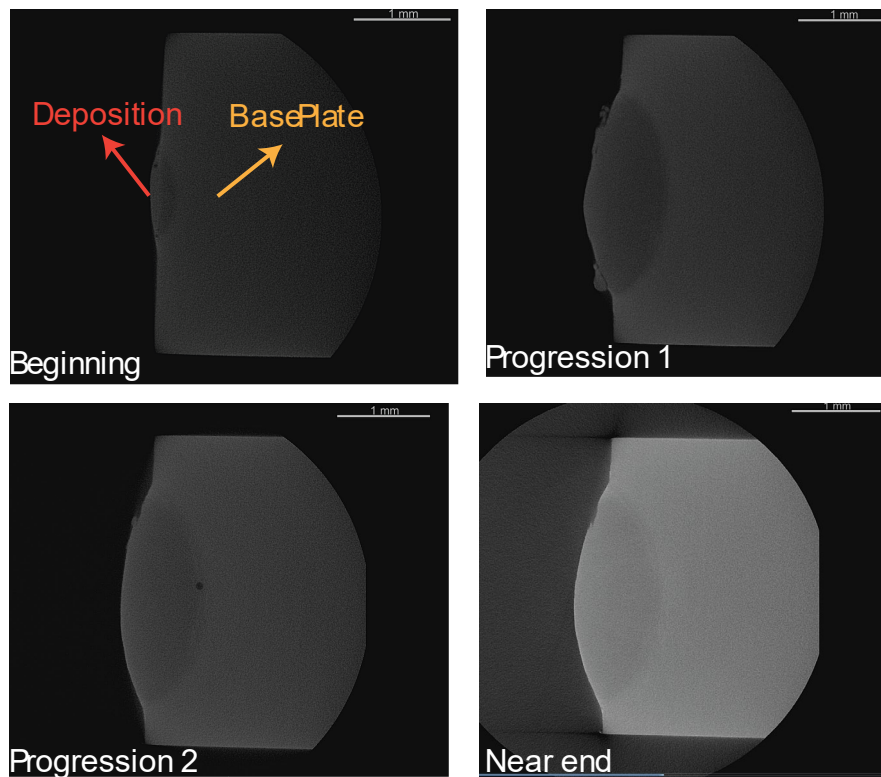
Figure 4.12 Start and the progression of a μCT image deck. The deposited material and the baseplate are illustrated in the top-left figure

The collected spectra signals can be summarized mathematically in the following:

Table 4.2 Mathematical expression of collected spectra signals.

Wavelength	Spectra Frame#1	Spectra Frame#2	...	Spectra Frame_End
WL_1	X_{11}	X_{12R}	...	X_{1i}
WL_2	X_{21}	X_{22R}	...	X_{2i}
WL_3	...	...	...	...
...	...	....	...	...
WL_end	X_{j1}	X_{j2}	...	X_{ji}

Here, X is in arbitrary unit ranging from 900 to 64000 and shows the intensity of the signals. "j" is a parameter that defines the total number of specific wavelengths, also a property of a spectrum collection box (for this case, j equals 2038). "i", on the other hand, signifies how many time steps were collected. Generally, "i" is equal to the division of total time elapsed to the timestep resolution (which is 10ms in this study). Given that, a five-second operation returns a million data points. Therefore, adequate data management (storage, access, etc.) is an integral part of this operation.

The raw spectral data contains data entry of 3 passes: front movement, back movement, and front movement of laser deposition. Since it is going to be compared with the local defect through μCT images, it is important to combine correct spectra entries of a particular region. As the old saying goes "A picture worth thousands of words", proper spectra group formation is shown in the following Figure 4.13. For this specific example, spectral data from frame#4, frame#17, and frame#24 are from the same location of the deposition. They will be analyzed

with their respective μCT scans. In this setup, the spectral resolution is roughly 4-5 times coarser than μCT. So, proper reduction should be applied to the data before proceeding to data analysis.
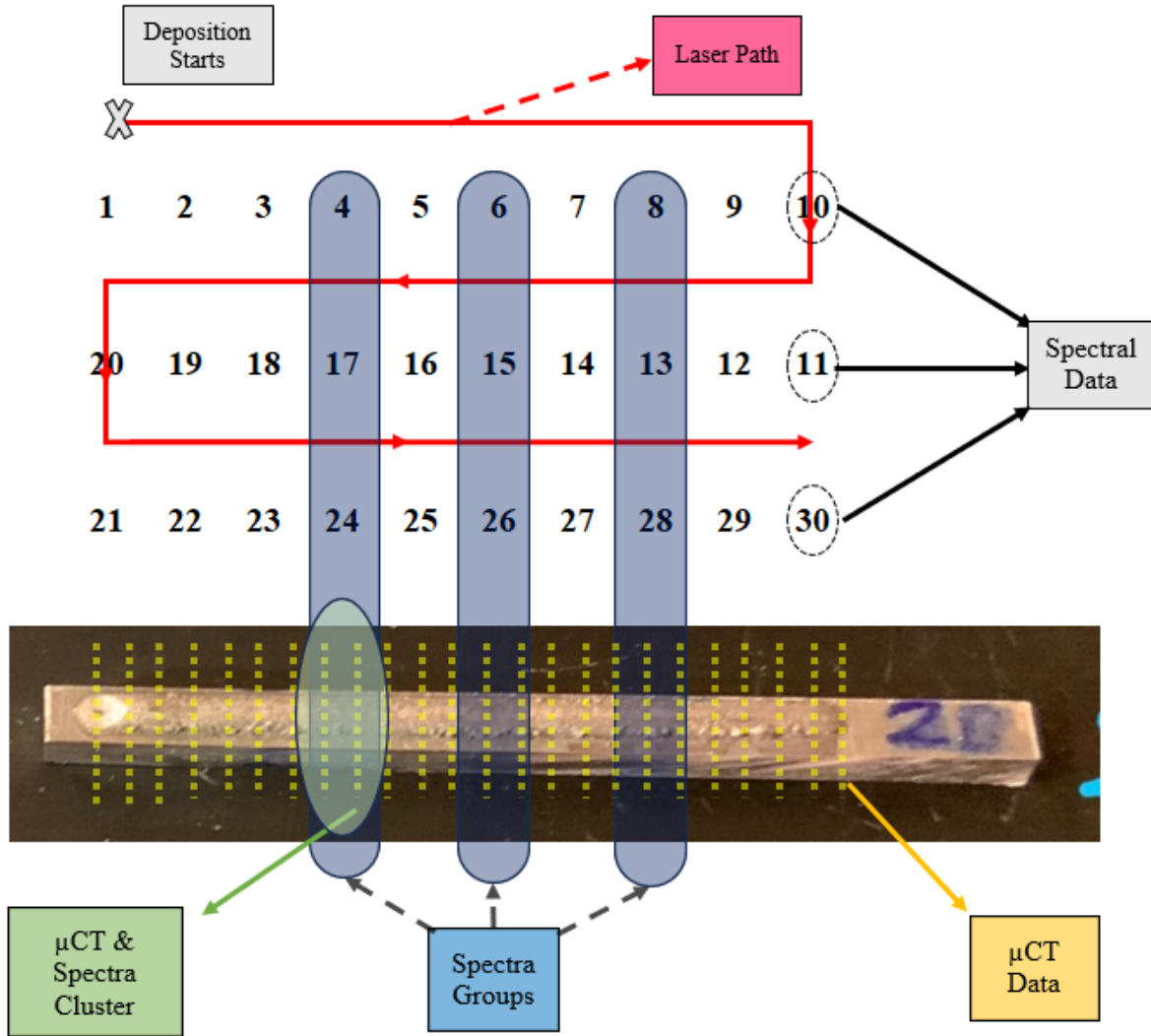
Figure 4.13 Spectra and μCT group formation with respect to their collected location. The red line shows the 2D (length-height) deposition path. Spectra data is captured in 1-30 numbers. Taking the deposition path into account, the correct grouping for spectra should be 1-20-21, 2-19-22, ..., 10-11-30.
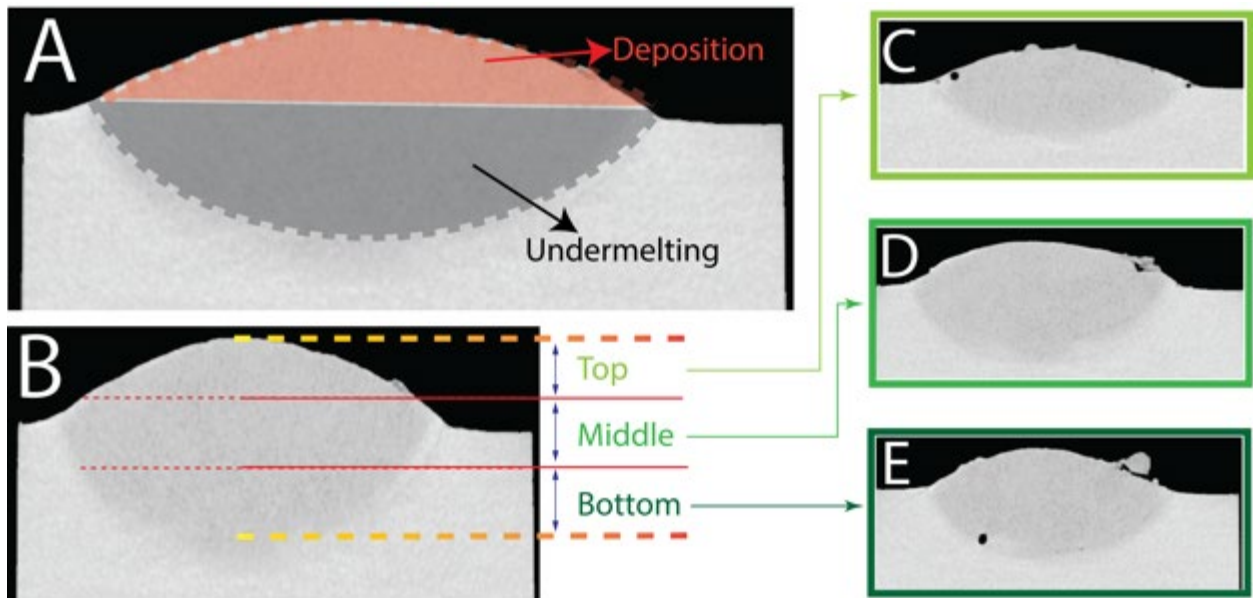
Figure 4.14 μCT images and their interpretation for the data analysis. The deposition and undermelting region can be seen in image A. C,D and E show the defects and their whereabouts, top, middle, and bottom respectively.

Overall strategy for the data processing can be explained in the diagram below:
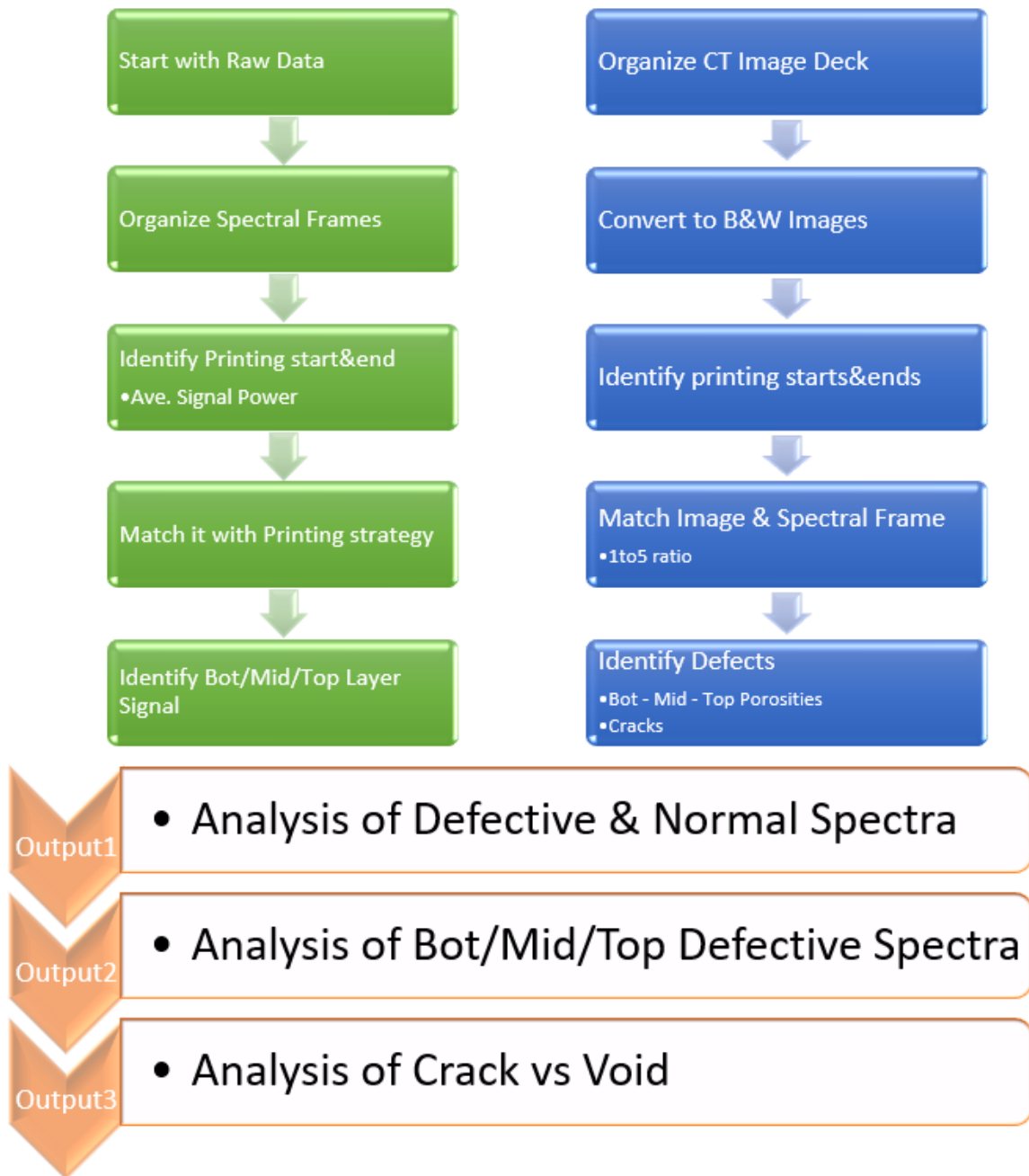
Figure 4.15 Grand strategy for data processing for spectra/CT correlation

4.2.3.1 Output1: Analysis of Defective and Normal Spectra

Defects in the deposition were characterized by their formation: crack or porosity. They were both marked as defects and the subsequent data analysis considers them as an output. For this chapter, the line intensity of the plasma was analyzed. Plasma signals were collected by a collimator lens which was mounted to the laser head. Therefore, the distance and angle from the lenses to the deposition were constant, which otherwise may affect the signal intensity. With this isolation, the line intensity method is consistent, and further analysis can be done on its foundation.

First, the spectrum signals were marked as "Clean" or "Faulty" depending on their respective μCT images.

$$\begin{bmatrix} X_{11R} & X_{12R} & X_{13R} & \cdots & \cdots & X_{1iR} \\ X_{21R} & X_{22R} & X_{23R} & \cdots & \cdots & X_{2iR} \\ X_{31R} & X_{32R} & X_{33R} & \cdots & \cdots & X_{3iR} \\ \vdots & \vdots & \vdots & \ddots & \ddots & \vdots \\ \vdots & \vdots & \vdots & \ddots & \ddots & \vdots \\ X_{j1R} & X_{j2R} & X_{j3R} & \cdots & \cdots & X_{jiR} \end{bmatrix}$$

$$i = 1,2,3, \dots, i_{end}$$

$$j = 1,2,3, \dots, j_{end}$$

$$R = C \text{ or } F \ (Clean \ or \ Faulty)$$

Then, the clean and faulty spectra signals are averaged in each wavelength.

$$ave\_WL\_clean = \qquad \forall j \ and \ R = C \ , \frac{\sum_{i=1}^{i=i_{end}} X_{jiR}}{i_{end}}$$

$$ave\_WL\_clean = \qquad \forall j \ and \ R = F \ , \frac{\sum_{i=1}^{i=i_{end}} X_{jiR}}{i_{end}}$$

115

Here the output1 is defined as follows:

$$Output1 = \frac{ave_{WL_{faulty}} - ave_{WL_{Clean}}}{ave_{WL_{Faulty}} + ave_{WL_{Clean}}}$$

The analysis showed that 96.7% of the time, faulty signals deviate from the normal (good quality region) ones (Figure 4.16). The analysis was promising, but it needed to be validated. With the random selection of the spectra, signal frames were compared against each other, and their deviation was reported, then they were checked against the collected CT images(A similar method to Monte Carlo simulation). The results were correct at 87%.
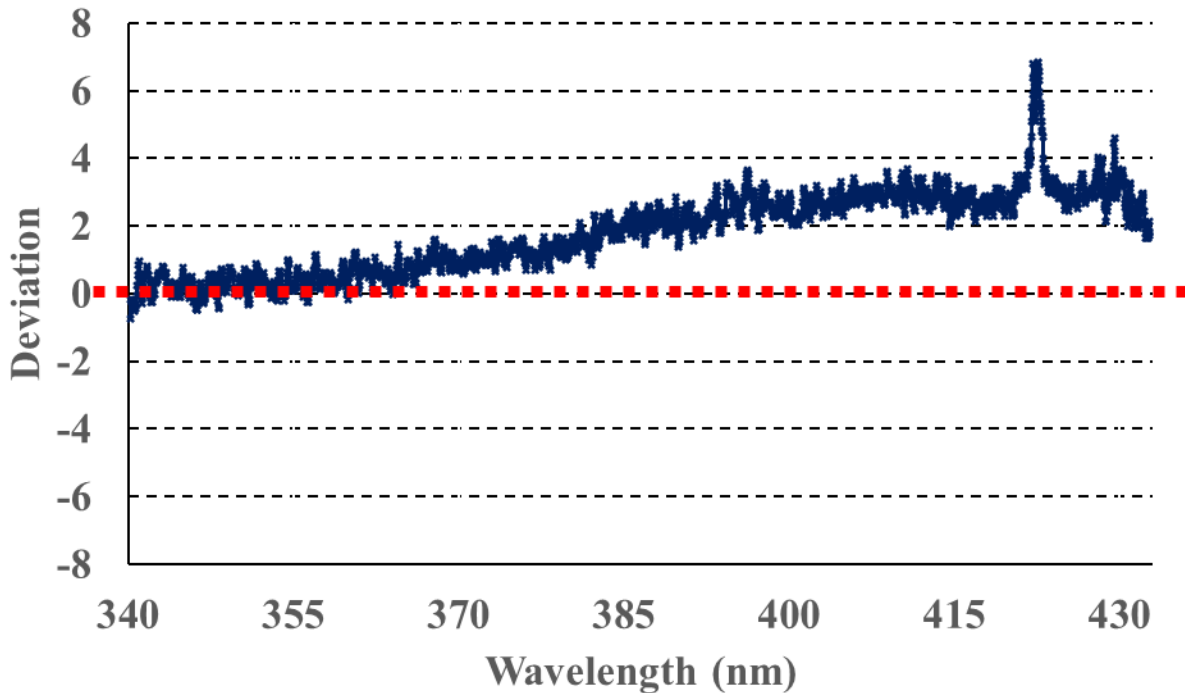
Figure 4.16 Deviation of the faulty signals from the clean

The implications of this discovery are manifold. Primarily, it beckons forth the possibility of reprocessing the deposited layer without detachment from the baseplate, thereby potentially enhancing the dimensional accuracy of the operation. Future Direct Metal Deposition (DMD)

116

technologies could consider this inclusion for their closed-loop systems, promoting greater yield

and throughput. An online defect detection capability can curtail overall production costs by

intercepting faulty parts before they reach the next process station, thereby aligning the

production process more closely with lean manufacturing principles.

4.2.3.2 Output2: Analysis of Spectra According to Location of a Defect

The location of voids within the deposition was classified according to their locations as

depicted in Figure 4.14: bottom, middle, and the top. In addition to voids, we also analyzed the

characteristics of cracks within the dataset. Then, we compared the results of signal intensities,

which were calculated using following equations. Unfortunately, as shown in Figure 4.17, no

evident data clustering was found. This is unfortunate, as pinpointing defect locations could lead

to the development of novel quality assurance methods. For instance, we could eliminate defects

on the top by machining the exposed surface. Meanwhile, defects in the middle or bottom of the

deposition could potentially be addressed using the well-known secondary process known as hot

isostatic processing (HIP).

$$\text{ave\_intensity\_faulty} = \qquad \forall i \text{ and } R = F, \frac{\sum_{j=1}^{j=j_{end}} X_{jiR,}}{j_{end}}$$

$$\text{ave\_intensity\_clean} = \qquad \forall i \text{ and } R = C, \frac{\sum_{j=1}^{j=j_{end}} X_{jiR,}}{j_{end}}$$
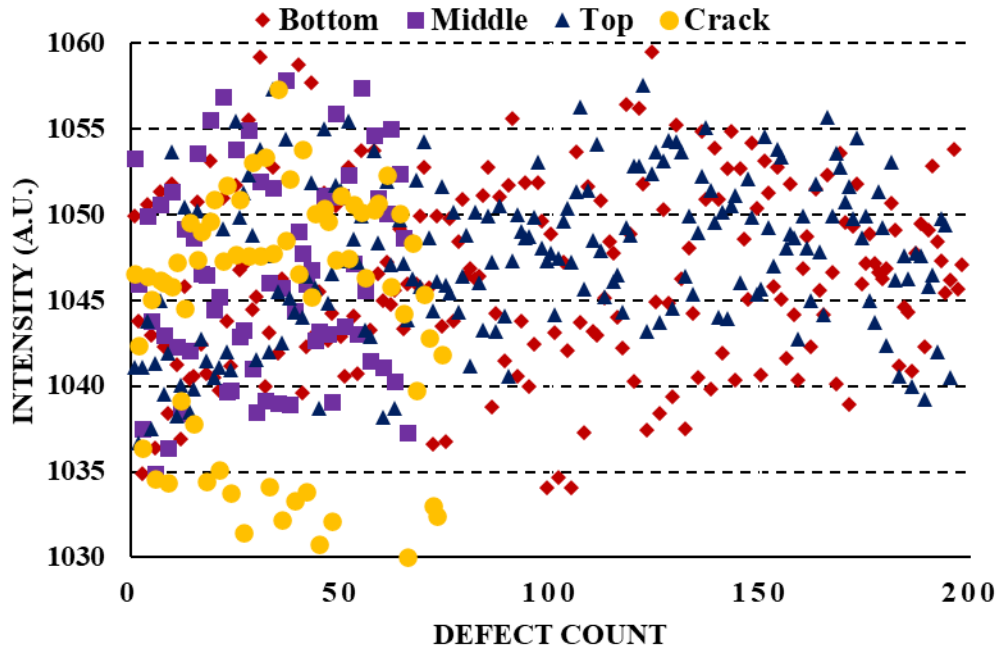
Figure 4.17 Unsuccessful try-out for clustering defective spectral intensities

4.2.3.3 Output3: Analysis of Crack and Void Defects

The spectral line intensities from the crack and voids (be it bottom, middle, or top region) were studied to see possible distinctions one from another. Crack formation in the final part might be more problematic than the void in some applications where the seal and vacuum integrity are required. Also, pores are known to be corrected but the cracks are not. Therefore, such analysis may contribute to speedy decision-making during the DMD process.
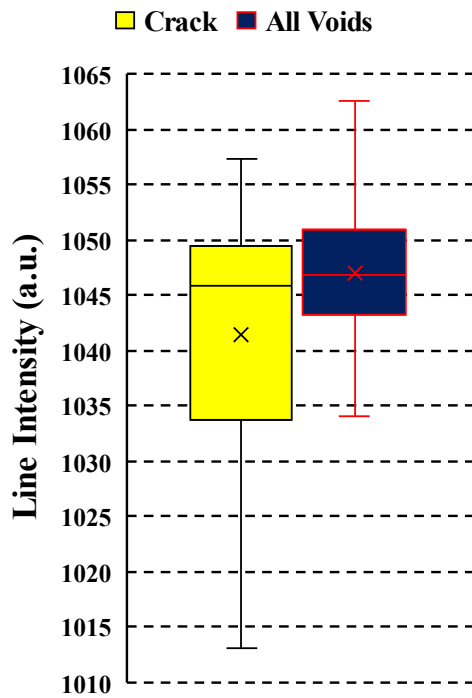
Figure 4.18 The intensity distribution of crack and void signals

There is no strong evidence supporting the void and crack distinction in the line intensity method in this study. The closest one that reveals a distinction is presented in the box and whisker diagram above. The signals from the crack region were found to be more spread than the voids. Voids generated slightly more intense signals than cracks. Although, no clear distinction, it is still reported in this section of the dissertation. Future studies can take this into account while advancing their analysis techniques.

4.2.4 Conclusions

In this section, the OES were collected during a real-time DMD process, final defects formed in the deposition zone were identified using µCT and their relevance was researched using the line intensity emission method. The conclusions can be summarized as follows:

- 96.7% of the time, defective spectra emit more intensely than clean (without defects) spectra.

- 87% of the sampled instances, defect prediction was conclusive.

- Line intensity changed irrespective of the defect location within the melt pool, thereby eliminating it from being a decision-making tool.

- Once the defect was identified, cracking and void formation were not so apparent in the line intensities of the collected spectra. Still, the former spreads more than the void formation.

Chapter 5 Laser Direct Metal Deposition of Molds for Wind Turbine Blades using Al6061-RAM2

5.1 Abstract

As the focus on reducing carbon emissions grows, wind turbines have become a prominent choice for clean electricity generation. In our study, we aimed to improve the production process of wind blades, a critical component of the system. Instead of the usual single-piece wind blade molds, we sought to create additively manufactured sub-modules, similar to Lego^{TM} pieces, using Al6061-RAM2, a new derivative of the 6061 series. Since there was no existing data for applying directed metal deposition (DMD) to this new alloy, we systematically worked on fine-tuning a fresh set of parameters. We started with a single-line deposition, conducting visual and chemical inspections after each stage. This enabled the team to produce specimens as large as 20cm in one dimension. In comparison to the traditional 6061 alloy, the new variant showed fewer instances of porosity and micro-crack formation. Continuing on this trajectory, the team was able to manufacture scaled-up versions of the wind blade mold and their dimensional accuracies have been documented.

5.2 Introduction

Aluminum alloys have been in use for a little over a century[113]. Though its relatively late discovery, aluminum alloys have found themselves in major applications, owing to their high specific strengths, heat conductivity, and corrosion resistances[84]. These days, people in academia and industry focus their research on the additive manufacturing of aluminum alloys, parallel to a new trend in manufacturing[114]. Nevertheless, this approach necessitates significant work in material development, powder metallurgy, printing strategies, and testing for the final product.

Direct Metal Deposition (also known as Directed Energy Deposition, but the DMD term has been used throughout the dissertation) is one of the metal additive manufacturing techniques that provides end users with many flexibilities. Due to its powder dispenser design, it is possible to control powder flow as well as the composition while printing. Printing volume per minute for DMD is also more advantageous than the widespread laser powder bed fusion technique; the ability to create thermal management channels, wear-resistant surfaces, and provide AI-based in-situ quality assurance make the DMD technique a better candidate for scaled-up metal additive manufacturing applications. However, there are several problems stemming from the nature of the DMD process that need to be addressed for a high-quality end part; hot cracking, surface roughness, process-related issues (powder being stuck at the tip of the copper nozzle), and requirements for high-skilled labor.

Big Area Additive Manufacturing (BAAM) is a process developed through a partnership between Cincinnati Incorporated and ORNL to scale up the extrusion of additive manufacturing processes. To achieve this, it uses injection molding material pellets and a single screw extruder to melt and meter the flow rate. They identified mold manufacturing for wind turbine blades as a potential application for the BAAM process and created a scaled mold as a test[115]. They introduced cooling/heating channels into the design and proved that the material characteristics supported a blade mold.

This study is part of a big wind blade project. We utilized the strong sides of both additive manufacturing and aluminum alloys to produce Lego-like modules for a subtask within the project. In this study, we used a new variant of Al 6061 that is optimized for enhancing the heat generation within the melt pool and optimized the process parameters to enable us to print up-scaled 3D coupons. Then, their performance compared to the existing Al 6061 alloys.

To a larger extent, the objective of this wind blade project is to reduce the cost and lead time of horizontal wind turbine blade mold tooling and blade transportation without sacrificing blade quality. Our cost-effective solution for mold manufacture includes a smart-design family of modular molds that can be transported to fabricate blades near their place of service, and the use of additive manufacturing (AM) to incorporate conformal thermal management channels that provide flexible control of thermal profiles tailored to the blade material, an in-situ quality assurance during mold fabrication, and an improved mold life and reuse, allowing amortization of the mold cost over a greater production volume.

5.3 Materials And Methods

5.3.1 Mold Design

Using Qblade software, a family of baseline 120m, 140m, and 150m blades are designed by scaling a public-domain 100m blade model from Sandia National Laboratory. With our collaborator, we applied uniform scaling for the blade span and the chord length and twist angles at each station. These individually designed blades shown in Figure 5.1 are used as baselines for the evaluation of the aerodynamic performances of the modular blade family with common sections.

Following the current practice adopted for production at TPI (major player in wind blade industry), we designed a family of 120, 140, and 150m blades with common mid-sections using Qblade. Candidates for common sections are identified as <10% difference in the number of stations and the maximum chord length. After several iterations, a 20m mid-section shown in Figure 5.1(a-c) is identified as an acceptable common section within all three blades.
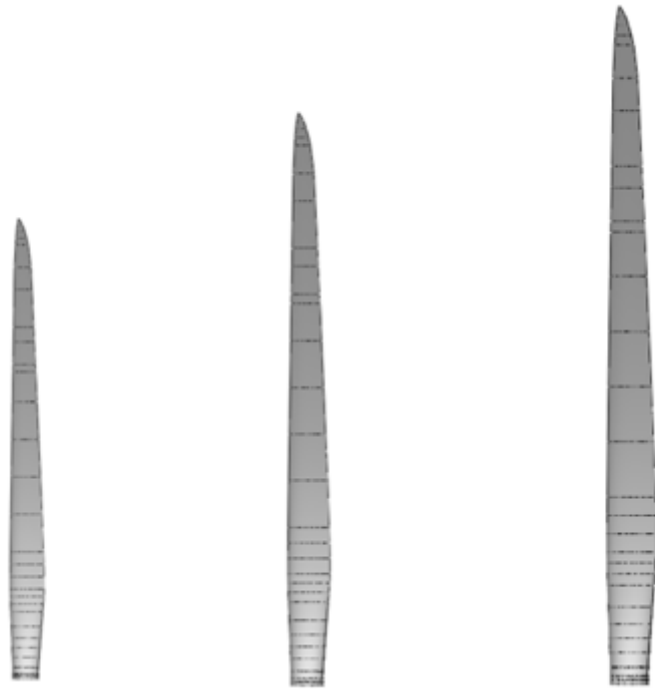
Figure 5.1 A blade family design; (left) 120m, (middle) 140m and (right) 150m.
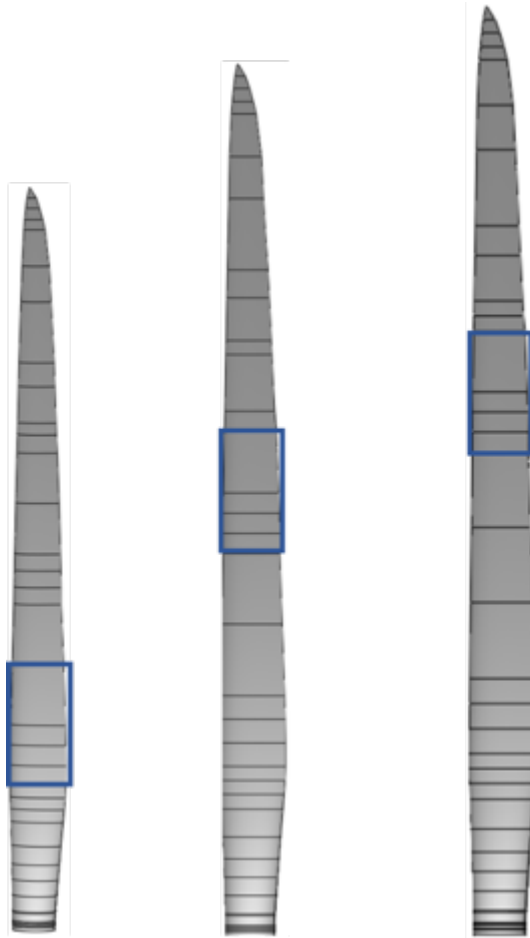
Figure 5.2 A blade family design with common midsection; (left) 120m, (middle) 140m, and (right) 150m

We compared the aerodynamic power coefficient of each blade of the family in Figure 5.2 with the individually designed blades in Figure 5.1 using QBlade. The result is shown in the following table. The maximum power coefficient Cp_{max} and its ratio to the baseline (Cp_{max} for the individually designed blades of Figure 5.1) are shown in the 2nd and 3rd columns, respectively. The results show for all blade lengths, Cp_{max} for the blades with common midsection (CM*) is 95-98% of the Cp_{max} baseline (SNL*) as predicted by QBlade.

Table 5.1 Comparison of aerodynamic power coefficient Cp_{max}

Blade Model	Cp_{max}	Relative Cp_{max}
SNL120	0.4417	1.0
CM120	0.4178	0.95
SNL140	0.4204	1.0
CM-140	0.4100	0.98
SNL150	0.4090	1.0
CM150	0.3899	0.95

5.3.2 Mold Production

5.3.2.1 Powder and Baseplate

Metal 3D printing powders were evaluated for their suitability as a feedstock material. The size distribution, powder shape, and chemical composition were evaluated for a 6061 powder, a 7075 Al alloy supplied by Valimet, and a 6061 crack-prevention formula (also known as Al6061-RAM2) supplied by Elementum3d. The 6061 powder was unacceptable as its size distribution was not uniform, small stuck to bigger ones (called satellites), and was observed to include faceted rather than spherical particles. The Valimet powder size was normally distributed but would require sieving to get rid of anything below 20 microns. It also had substantially high satellite formation and was not spherical. The powder deemed most suitable was the one from Elementum3d. It exhibited a normal and desirable size distribution, and the shape of its particles was noticeably more spherical.

The AM melt characteristics of the in-house 6061Al alloy powder on a 7075 baseplate and the Elementum3d 6061 powder on a 5052 baseplate were studied for the blade mold. For compatibility between the University of Michigan CLAIM Lab and DM3D company (Michigan-based metal additive manufacturing company for scaled-up productions), the Al6061-RAM2

alloy has been the focus of study of the build material. The 7075 and 5052 Al plates were identified as the best target baseplates, as the baseplate should mate well with the build material.

A new variant, named RAM2, of 6061 Al alloy was supplied from Elementum3D in a powder form. Upon arrival, it was prepared for scanning electron microscopy (SEM) as per Claim Lab's acceptance procedures. There, it was examined whether the powder was spherical and within the listed diameter (Figure 5.3). While the specimen was under vacuum, its chemical composition was also inspected via Electron Dispersive Spectroscopy (EDS) to validate company-provided specifications. Both of these data compared to the conventionally produced Al 6061 powder (Figure 5.3 and Figure 5.4). Later on, these powders were used for demo printings, just to observe their behavior after a laser interaction.
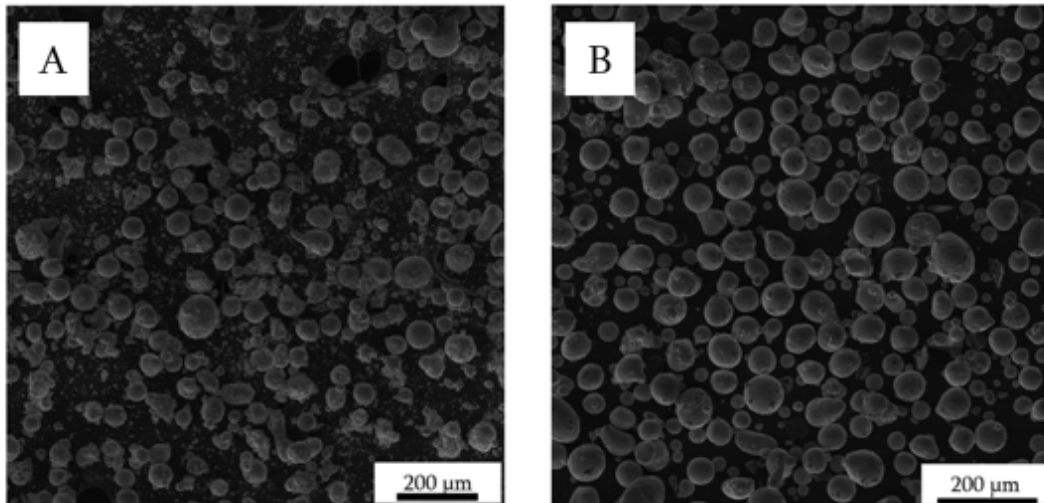
Figure 5.3 A: conventional Al6061 B: Al6061-RAM2 used in this study
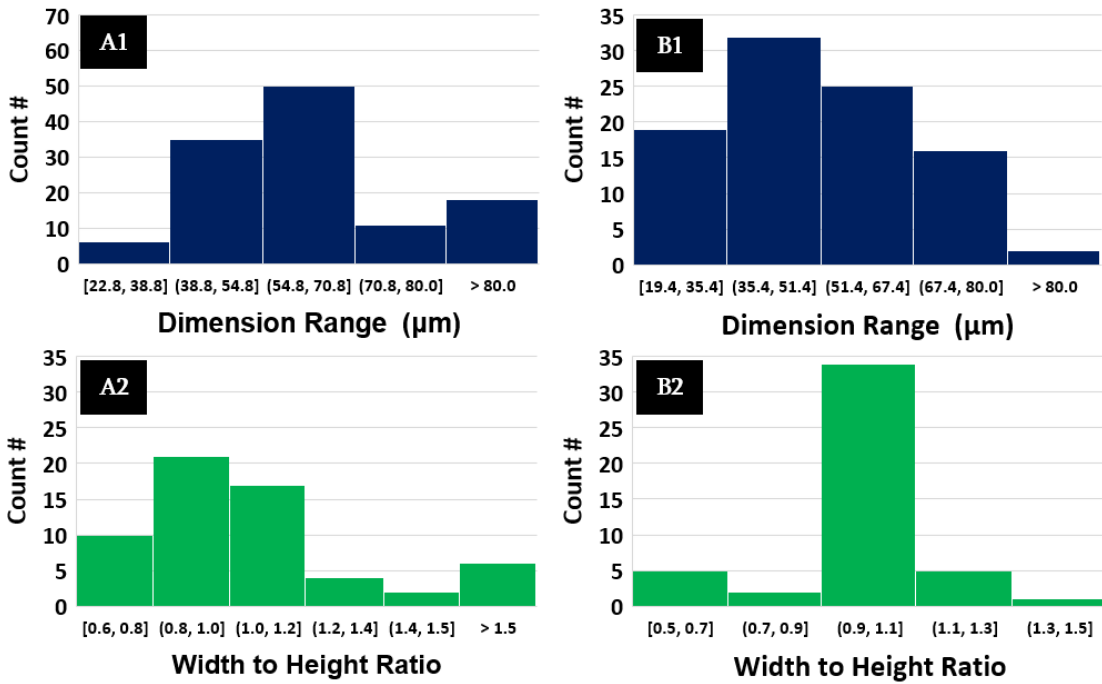
Figure 5.4 A: conventional Al6061 B: Al6061-RAM2 used in this study.

The baseplate for DMD was chosen as Al 5052 alloy at a 9.5mm thickness. After the delivery, it was cut by 20x20cm in square and drilled from the corners to fix it to the optical table. The top surface roughness was left as-rolled (around 3.2 microns), but it was brushed with a steel brush to remove a possible oxidized layer in order to remove unwanted phases and enhance the heat transfer.
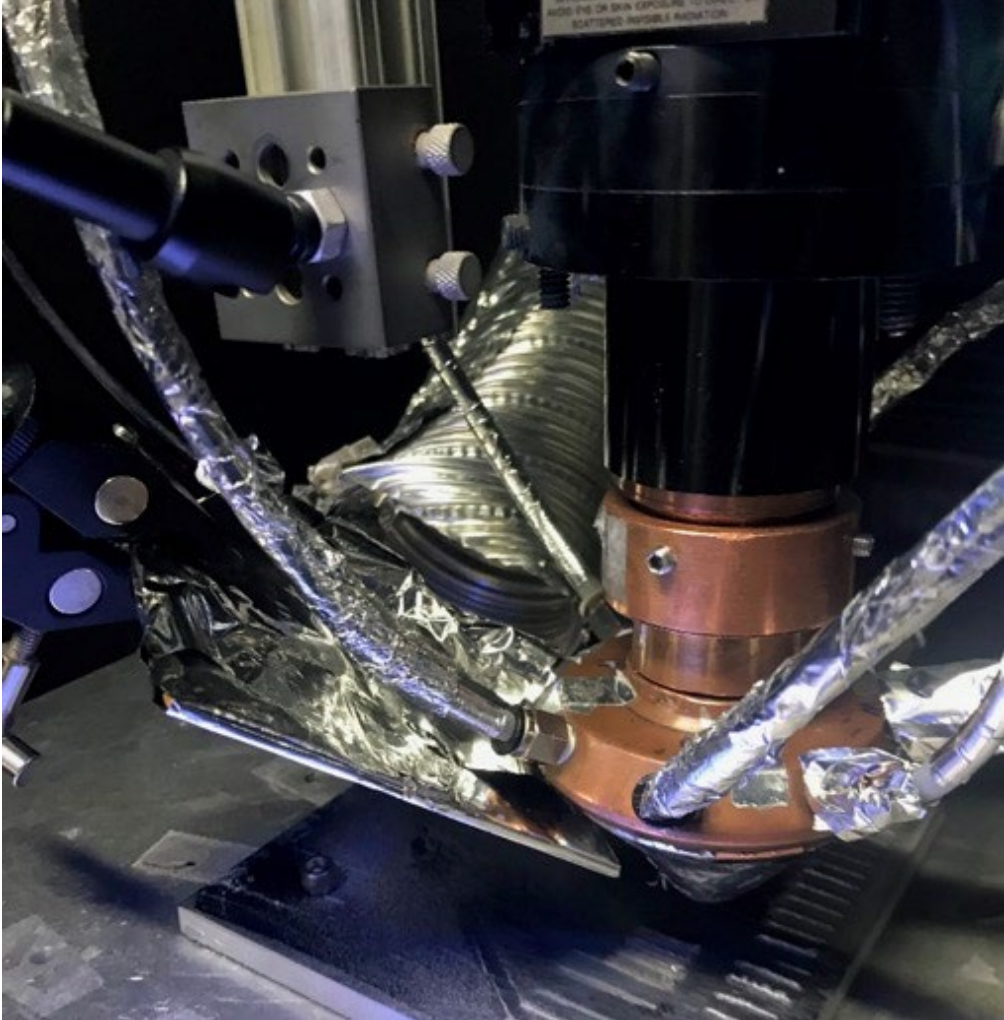
Figure 5.5 Experiment setup, a view of DMD nozzle and some printed stripes.

5.3.2.2 Printing Strategy

The DMD machine used for this study was designed customizable, which lets users control the laser, powder flow, gas flow, and printing variables separately (Figure 5.5). The number of individual controllable parameters [5] can be as high as 18. There are some efforts to consolidate the most important parameters (laser power, scanning speed, laser beam diameter) into one parameter (energy density, power density, etc.), but they generally fall short of fully explaining the printing process[116]. Therefore, it requires a systematic approach to tune them

for high quality printing. As for the printing strategy for this project, we followed an arbitrarily defined 8-step roadmap:

I. A single line with a continuous height and deposition

    a. Objective: Physically consistent and better-looking depositions.

    b. Qualifications: Bead must be continuous; the balling effect is a no-go condition. Inspections are done visually.

II. 1,2-,3- and 4-line deposition with sequentially increasing mode

    a. Objective: Evaluation of the under-melting (the melt pool depth), fully dense portion of the deposition as edges might include semi sintered powders, stable layer thickness evaluation.

    b. Qualifications: Layer thickness must be consistent for the 3rd and 4th layers. At least half of the deposition width must be fully dense.

III. 4-line on top

    a. Objective: Validating previously obtained layer heights.

IV. 4 side-by-side depositions, each of which has 4 layers

    a. Objective: Mimicking the up-scale printings

    b. Qualifications: No cracking occurs in the lateral melt pool boundaries

V. Small square (15mm) with 1 and 2 layers

    a. Objective: This is considered the first step of up-scale printing. This must show a good transition between the printing lines.

    b. Qualifications: Valley-to-peak distance should be less than 50% of the deposition height.

VI. Small cube (15x15x15mm)

a. <u>Objective</u>: Achieving the machinable cubes to; first, validate the prior findings and second, to test final surface finishing.

b. <u>Qualifications</u>: No major cracking in the printing body, having a +97% density.

VII. Small rectangular box

VIII. Aimed rectangular coupons.

For each stage of the process, we defined some criteria (namely bead width, bead depth, deposition height, continuity of the deposition, and porosity/density) to evaluate whether the process was ready to move on to the next phase. Whenever the process failed to meet these benchmarks, the experiment was redesigned. We kept track of any settings that didn't work in order to establish a range of suitable conditions or 'processing window' for this specific material and the DMD process being used.

5.4 Results And Discussion

5.4.1 Printings at CLAIM lab

Among the many adjustable parameters, a total of 5 key parameters were identified to be controlled for the initial experiments. While laser-related parameters determine the physical behavior of the laser material interaction, others like shielding gas flow and deposition length are crucial for the continuity of the deposition bead. Here, we were not able to use some benchmark parameters from the literature, because the custom-built nature of our DMD facility operates differently. Table 5.2 shows the parameters and their ranges. For ease of application, we always prefer to change the laser power as a starting point in the experiment design. Other parameters are more time-consuming to adjust and may not offer as much precision as adjusting the power.

For the very first step of the printing strategy, single-line deposition experiments were conducted for both of the alloys. Their continuity, balling effect on sides, and the deposition process (expecting no deformation to occur in the optics and nozzle) were visually inspected. Here, conventional Al 6061 (Figure 5.6) did not result in good quality, contrary to 6061 RAM2. For advancing a further experiment, we ensured that the given parameters are producing a steady deposition and repeatability. Figure 5.7 shows the advancements during the trials. Because these decisions are based on subjective assessments or require specialized knowledge in material characterization (such as cutting, polishing, etching, and SEM), DMD technology still demands highly skilled operators. This critical need for expertise is seen as the main hurdle to further commercialization of DMD technology.
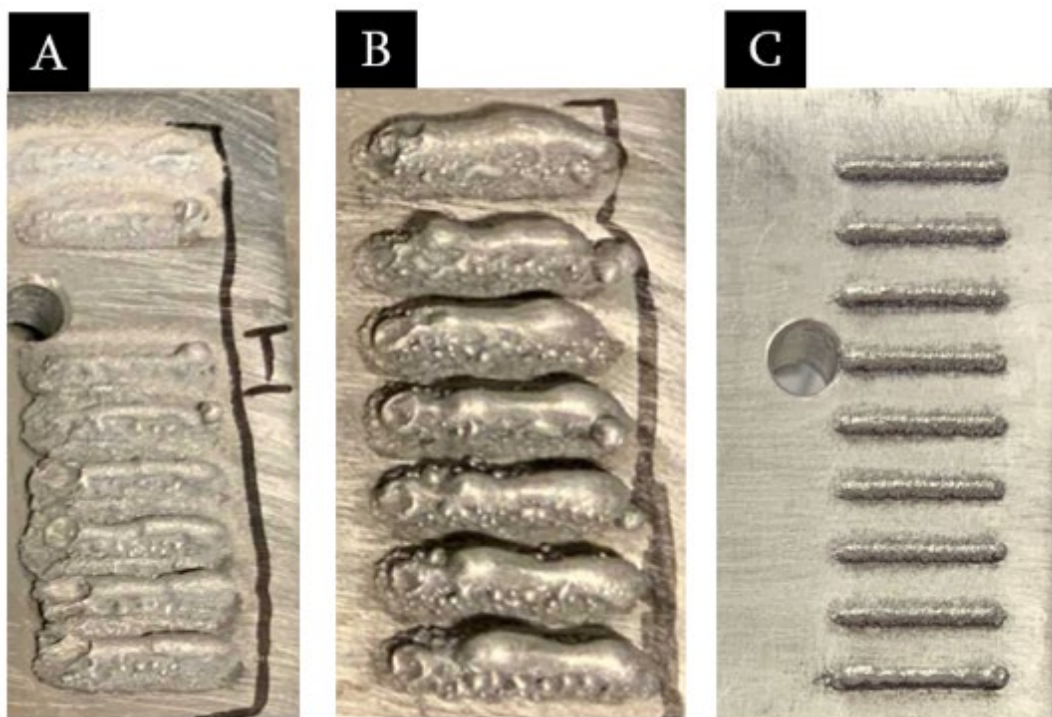
Figure 5.6 Evolution of the step1 printings from left to right (label A shows conventional Al6061 deposition and label C shows the good conditions to proceed to the next step)

Table 5.2 DMD input parameter ranges

Parameter	Range	Notes
Laser Power (W)	600 - 3500	at 1030nm wavelength
Laser Dia. (mm)	0.6 – 2	
Powder Flow Rate (mg/sec)	19.9 – 60.1	
Shielding Gas Flow Rate (SCFH)	10-90	
Deposition Length (mm)	10-50	Important to reach a steady state

Other observations were reported in the Table 6. 7.

In the next phases of the printing strategy, it's necessary for us to print multiple lines side by side while keeping the laser active. To do this, a stable printing process is essential. Without it, operators risk significant failure in the DMD system, including dangerous mishaps like nozzle meltdowns or laser-related damage to the system, or even safety risks to the operators

themselves. A good set of parameters were identified after quality validation and ensuring the system stability: 1400W power, 1.1mm laser diameter, 20 mg/sec powder deposition, 30 SCFH shielding gas, and finally 50mm of deposition track length. These were tested with the remaining steps in the printing strategy and the results were displayed in Figure 5.7 and Figure 5.8.

A rectangular coupon printed with the given set of parameters is the densest block obtained by the process. Using Archimedes' principle, its density was found to be around 98% without any post-processing (like hot isostatic pressing). While its scope is beyond this study, SEM characterization showed no traces of hot cracking or lack of fusion inside the material. Pores found within the fusion zone are thought to be from environmental conditions as they were randomly distributed and found perfectly circular.
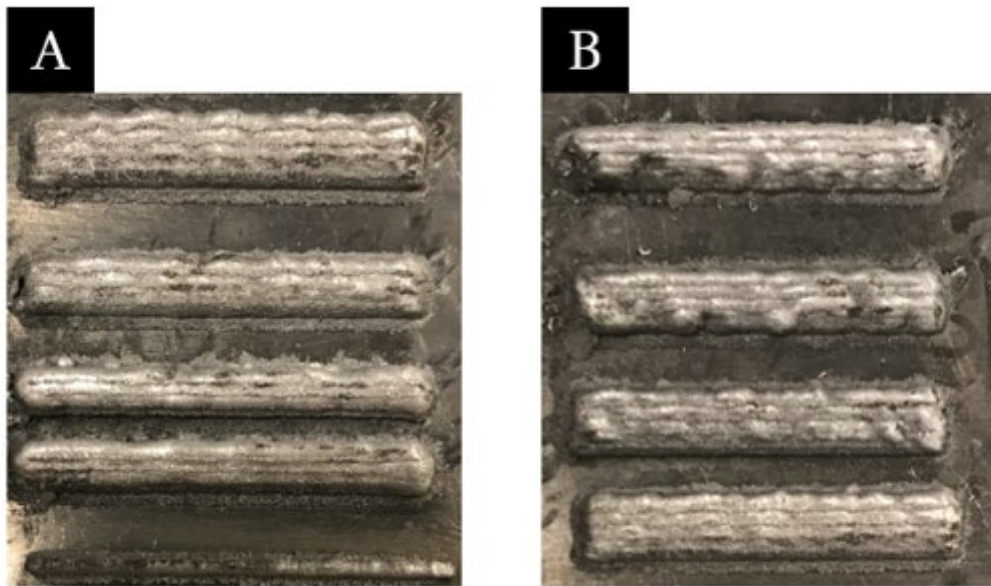
Figure 5.7 Steps 2,3 and 4 from the printing strategy. Label A shows the evolution from bottom to top and label b illustrates the stable printing from top to down.
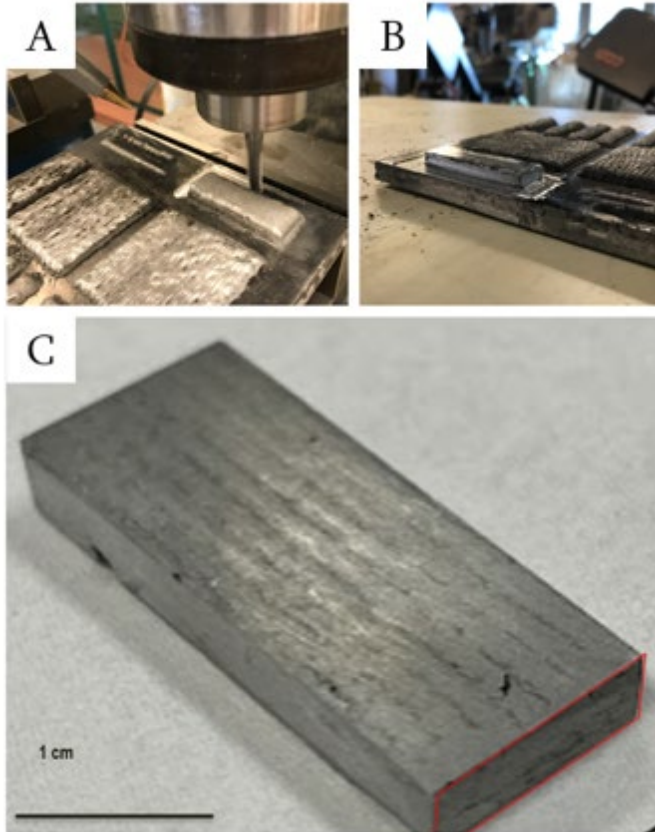
Figure 5.8 Rectangular coupon printing as a final step of the printing strategy, from the as-printed structure to the as-machined one.

5.4.2 Printings at DM3D for larger-scale parts

To handle larger-scale printings, we adopted an iterative process to avoid expensive

issues. Initially, we created representative, scaled-down test pieces (approximately 5cm in size).

Once we had made measurements and carried out characterizations on these samples, we then

scaled up to a 1:20 model (approximately 50cm in size). For measurements, we scanned both the

as-deposited and as-machined samples with a Coordinate Measuring Machine (CMM). We used

Polyworks software to interpret the results, which allowed us to extract the dimensions and any

deviations from the original CAD data.

5.4.2.1 Printing Iteration 1

This phase is designed to launch metal additive manufacturing research for the wind blade project. The contractor DM3D fabricated sample pieces using designs provided by the University of Michigan team. Although this initiative serves multiple objectives, in this section, we'll focus on its alignment with the intended design specifications. Though beyond the scope of this dissertation, the figure below provides a close-up view of the prepared and polished side panels intended for additional vacuum testing. The curved upper surfaces illustrated are part of an examination into advanced electro-chemical machining techniques to achieve mirror-like finishes.
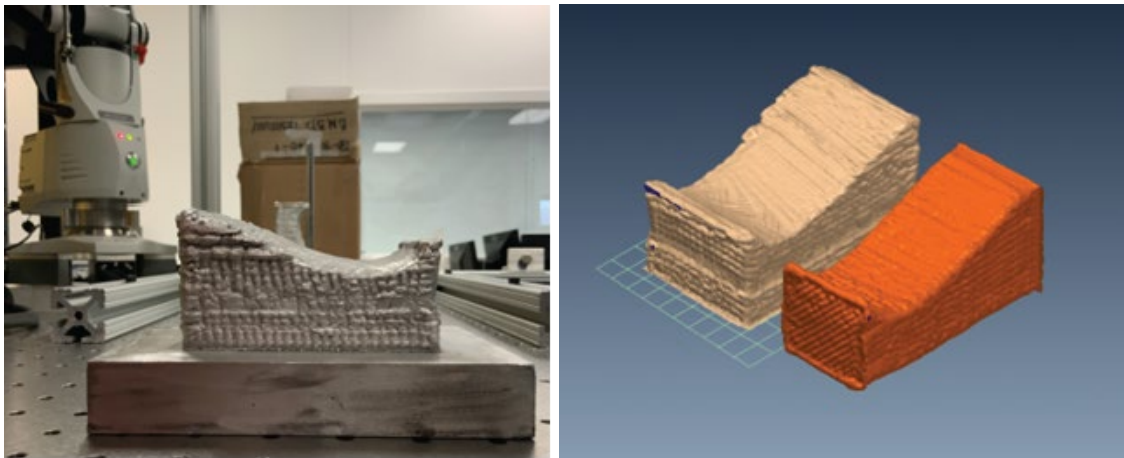
Figure 5.9 As-heat treated and unmachined 3D printed preliminary scaled-down mold (on the left) and laser scan of the of the two mold segments.
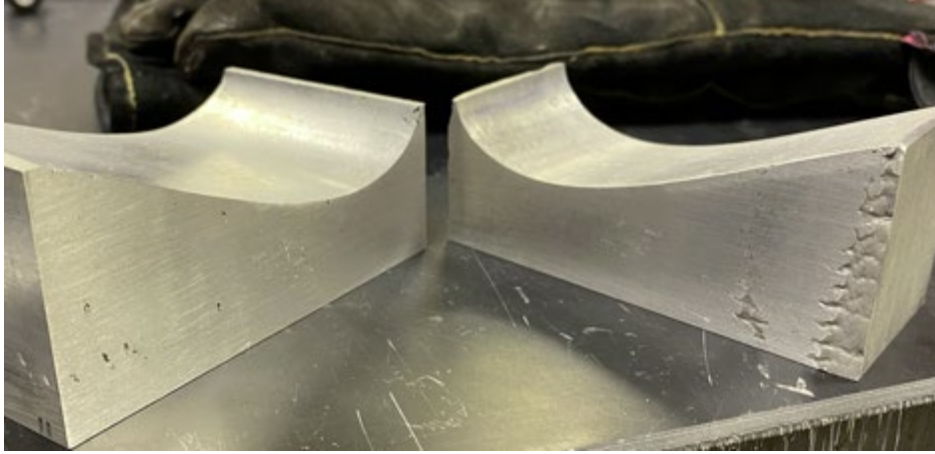
Figure 5.10 The same mold as the previous figure, but as-machined. The sides were ground and polished to reduce surface roughness to maintain vacuum in the joints.

At this point, the dimensions of the machined molds were not reported. The intention with the as-machined parts was more toward surface finishing for vacuum integrity testing. The test in this stage would fail due to the lack of fusion in the corners (Figure 5.10). These parts were subsequently passed on to a collaborator from Penn State University for destructive mechanical tests. These mechanical tests were only to validate the design intent. Otherwise, it is not a limiting factor for this study, as the composite wind blades are very lightweight and do not require excess forces for pressing.

5.4.2.2 Printing Iteration 2

This is the first 1:100 prototype of a mold for the wind blade project. Topology optimization (TO) techniques for weight reduction and necessary heating/cooling conditions were used simultaneously for this part. TO parts look quite futuristic as they place a material in a position as and when necessary. Most of the time, they are almost impossible to be realized with conventional formative or subtractive machining methods. Therefore, metal additive manufacturing and TO are perfect complementary production tools. As the next stages of this

137

project would be built on this relationship, its dimensional accuracy was inspected meticulously. The topologically optimized mold module is presented in the figure below.
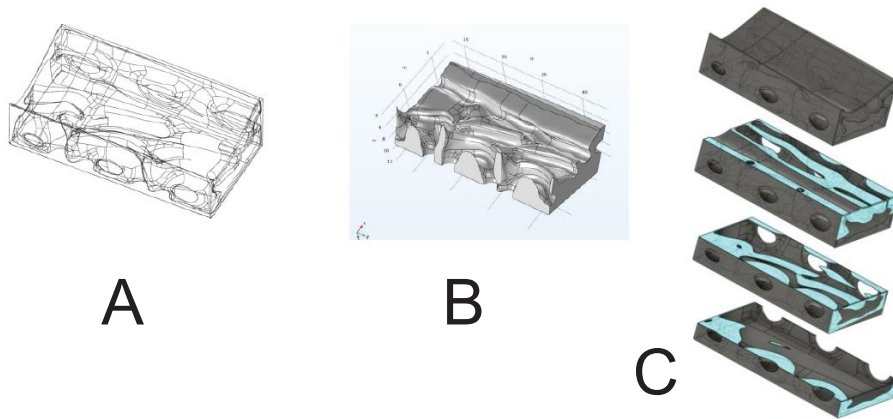
Figure 5.11 Topology optimization of a mold: A) Mold module with hidden lines B) Optimized air channel for heating and cooling C) section views of the mold module with air channels

As mentioned earlier, the DMD process for these quite complicated parts requires a state-of-the-art approach. With the fine-tuned deposition parameters in mind, the orientation of a mold, their clamping to the baseplate for improved deposition and subtracting accuracy, proper management of the excess powder to mitigate reduced final strength of a printed body, designing and minimizing the support structures and many minor but not least factors were combined together to get the product of design intend. Some of these steps are shown in the figures below, courtesy of DM3D:
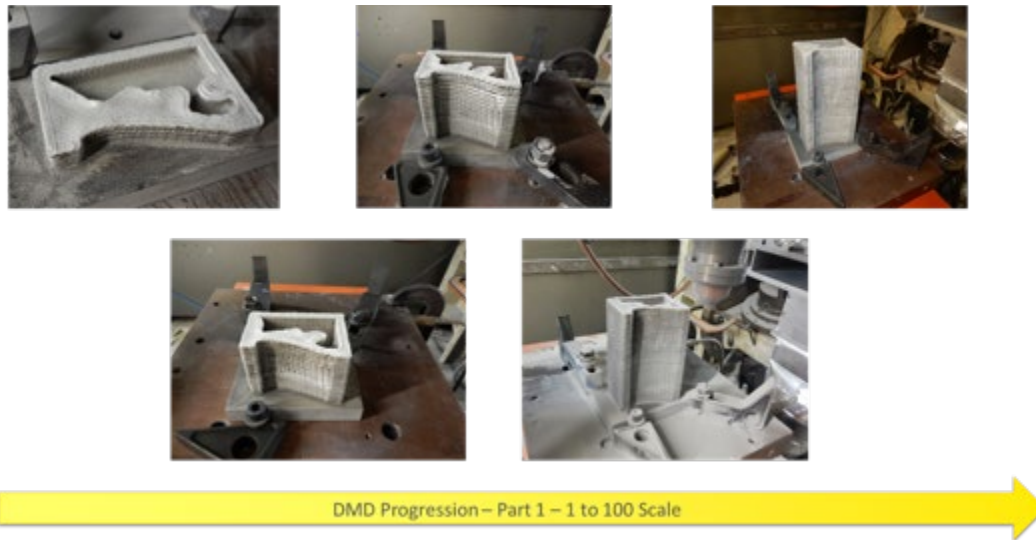
Figure 5.12 DMD progression of a TO mold with intricate internal air flow channels

Figure 5.13 A special technique to join the cap to the printed body without requiring support structures.

The as-printed part was delivered to UofM. Upon receipt, the part underwent a series of dimensional checks on the mold. It was scanned with a CMM machine and compared against a CAD (design intent) model. If discrepancies in the dimensions were detected—specifically, a decrease in size—the University of Michigan team would have had to reject the part. This is due to the fact that the subtractive machining process also removes some thickness from the part, likely causing it to deviate further from the original design.
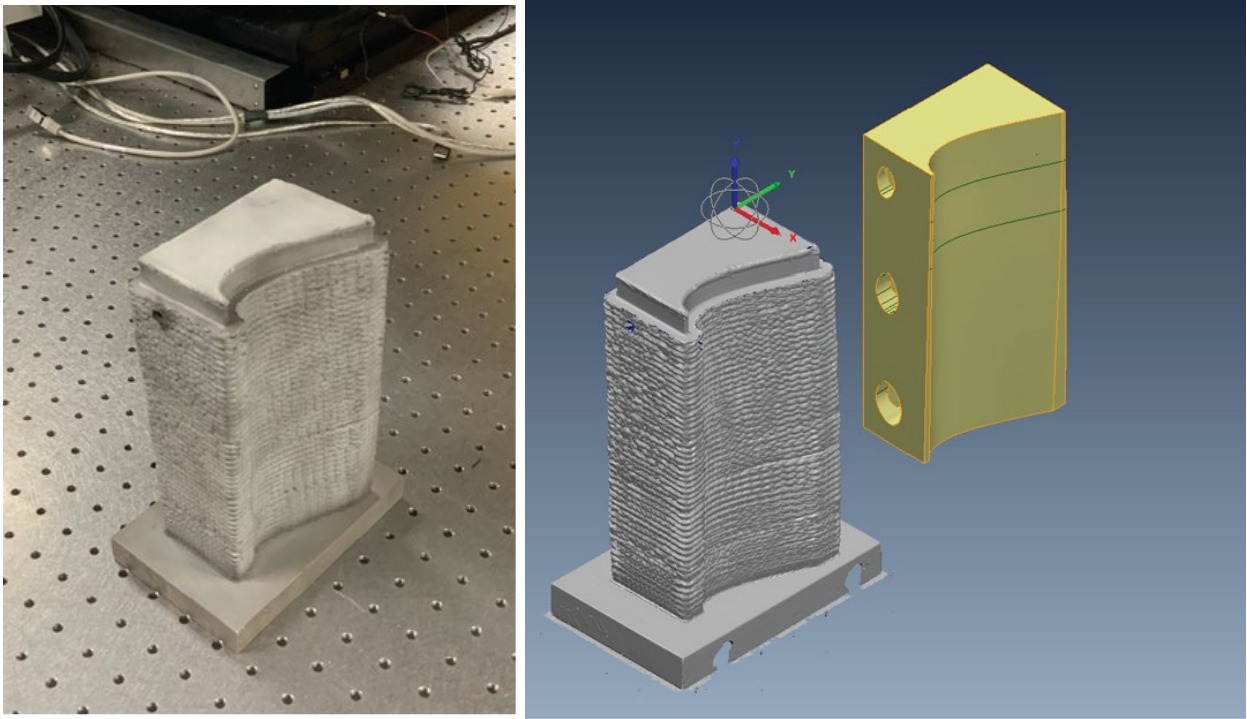
Figure 5.14 Printing iteration #2. The overall photo is given in the left and the right ones are in the software environment. The gray one is the 1-1 scaled data points and the yellow one is the design intent.
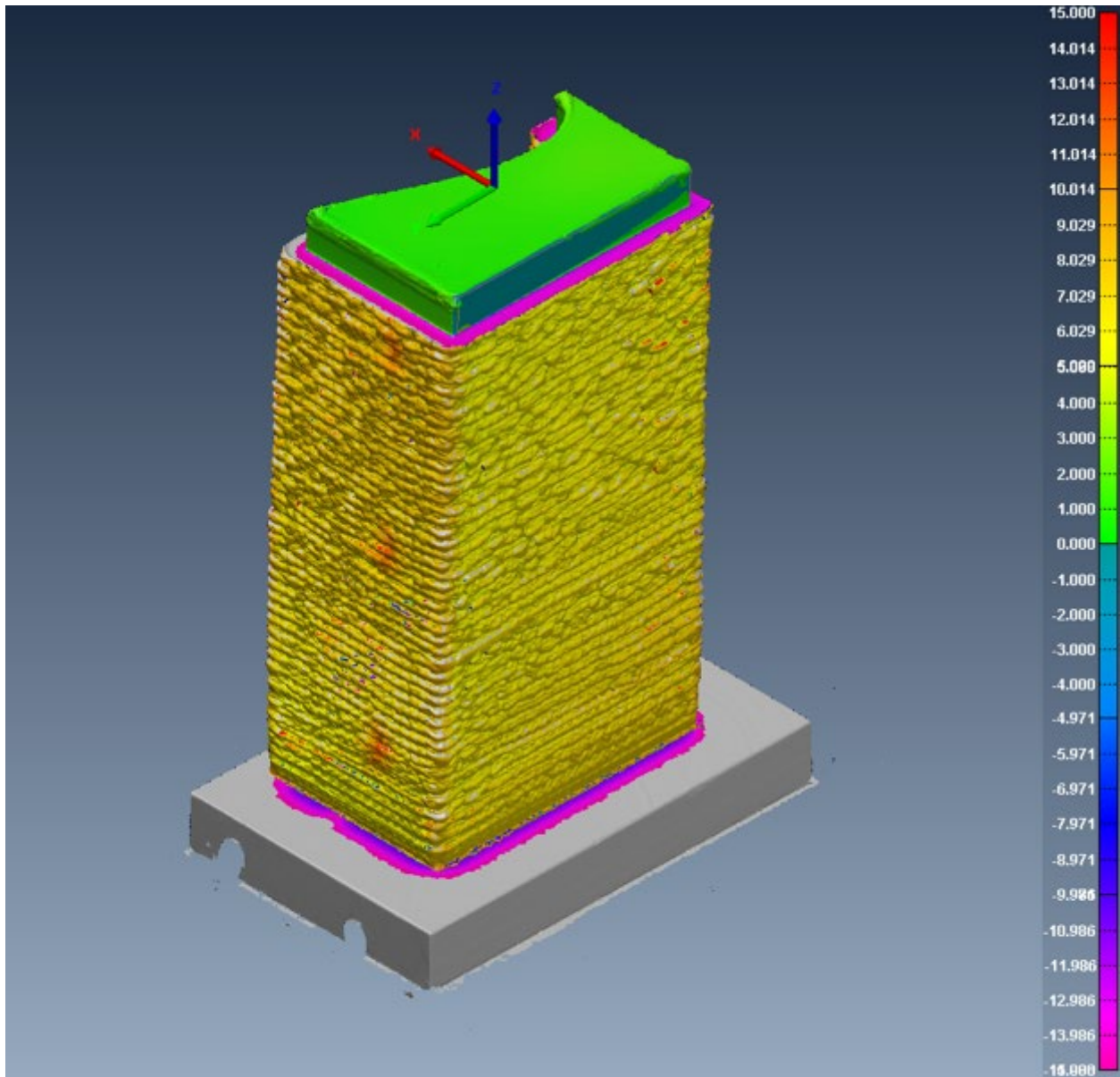
Figure 5.15 Compared to the CAD model, no negative dimensions were detected in the mold body. The pink color around the cap joining and the base plate are scanning artifacts and can be disregarded. The dimensions in the color bar are in mm.

A final comparison of the machine-finished mold and the CAD model is shown below. The surface of the mold—which is critical since it shapes the intended surface profile of the wind blade—showed satisfactory dimensional accuracy. No abrupt changes in the profile were observed. However, there was a noticeable protrusion on the side of the mold near the tip (shown

in the Figure 5.16). While this was within the established specifications, it was noted for future

iterations, given that other groups might need to perform seal testing on these sides. Such a

protrusion could potentially disrupt the seal between the mold faces, leading to issues with

vacuum integrity.
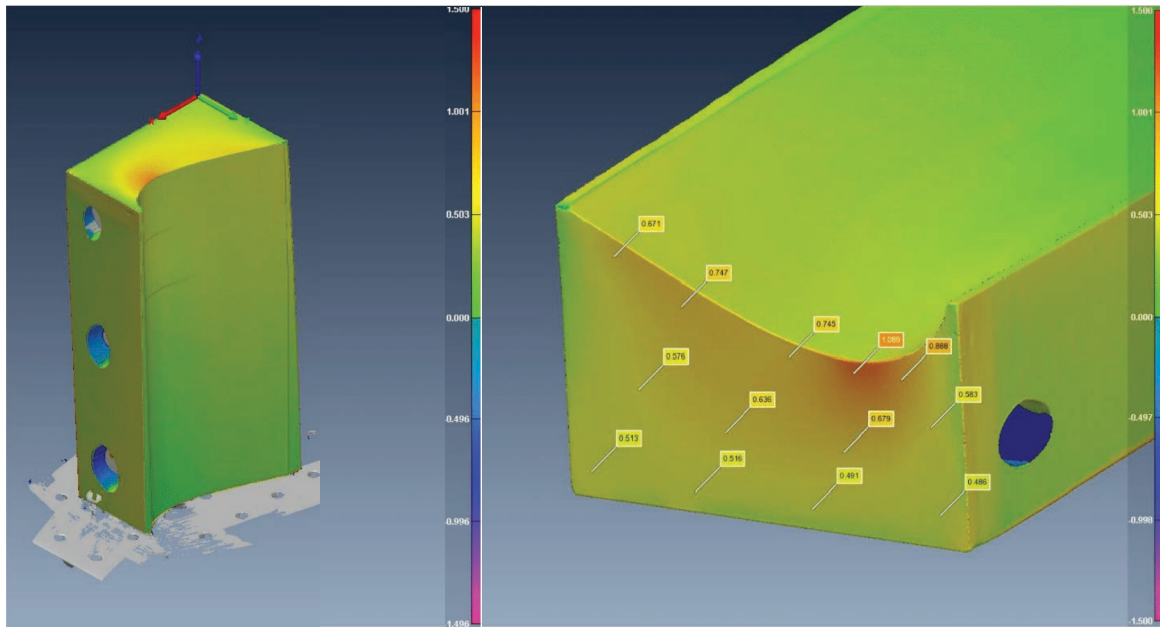
Figure 5.16 The final dimensional accuracy comparison for the printing iteration #2. Although some deviation in the side surface (illustrated in the right figure), it was still within the defined parameters, less than 5mm

5.4.2.3 Printing Iteration 3

In this section, the design of the mold has been taken one step further: shell mold type.

The enclosure in the previous study was removed to reduce overall printing time, material usage,

and definitely, not the least, printing cost. The enclosure was replaced with a support structure

made out of aluminum beams and sheets, which are readily available off the shelf.
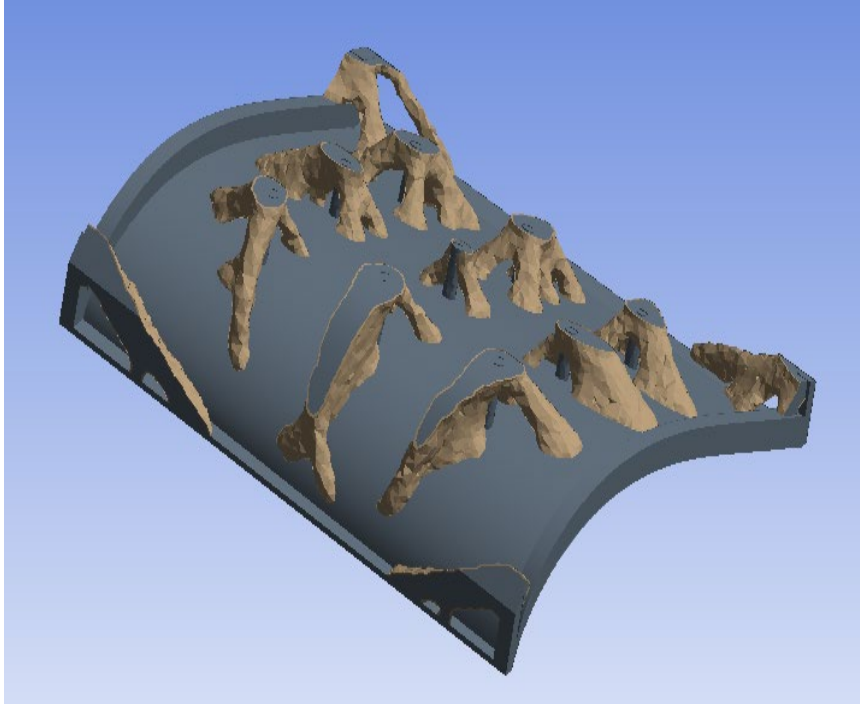
Figure 5.17 Design of a mold for the printing iteration #3. The organic-looking back supports, which causes reduction in the weight and increment in the heat exchange rates, can be seen.

he unique structure of the object, which overhangs at the back (see figure below), required a special method for production. Initially, the shell body was constructed using the Direct Metal Deposition (DMD) system. Following this, the baseplate was rotated and re-set in a new position, allowing the remaining structure to be printed. DMD operates in accordance with gravity, thus it is crucial that the target area is positioned directly under the DMD nozzle. This requirement could potentially cause significant warping of the already printed parts, and as a result, maintaining dimensional accuracy is critically important for this method. The final products, both as they appeared directly after printing and following machining, are depicted in the figure below.
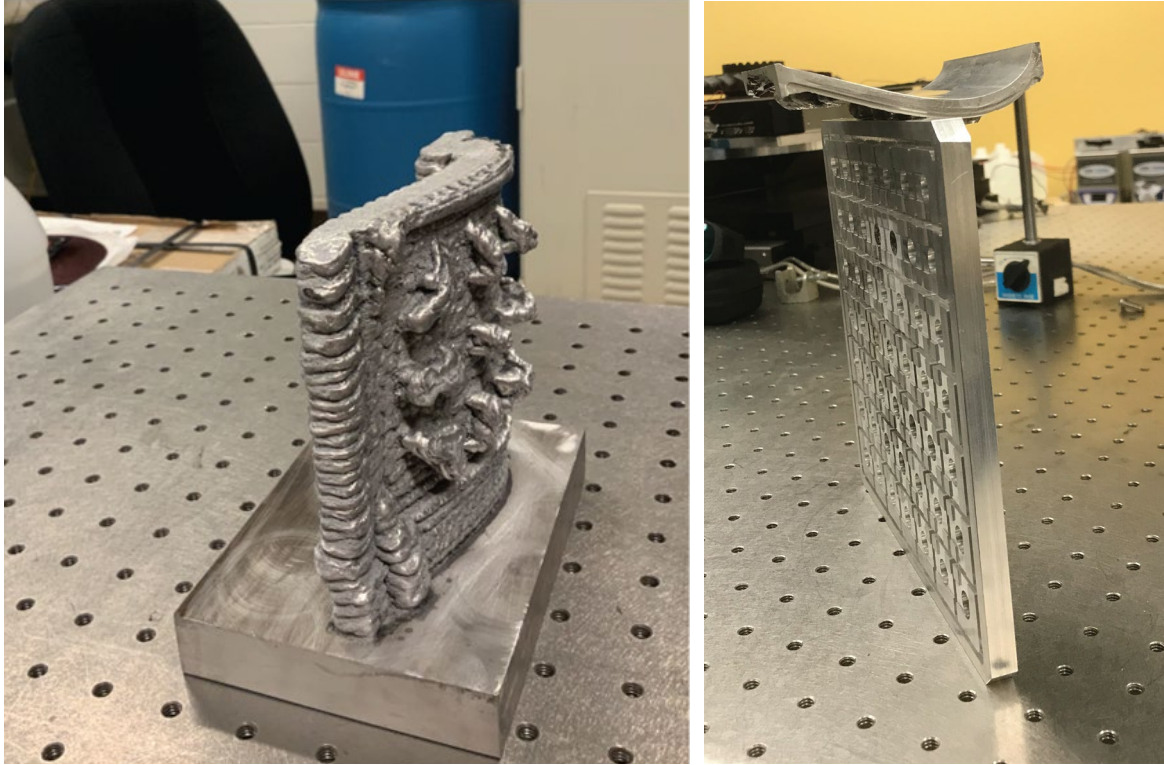
Figure 5.18 The as-printed and as-machined parts were presented. The as-machined one is placed a special plate to scan it all around in detail

The critical dimensions and the curvature surface were reported as follows. No red flag was observed in this step.
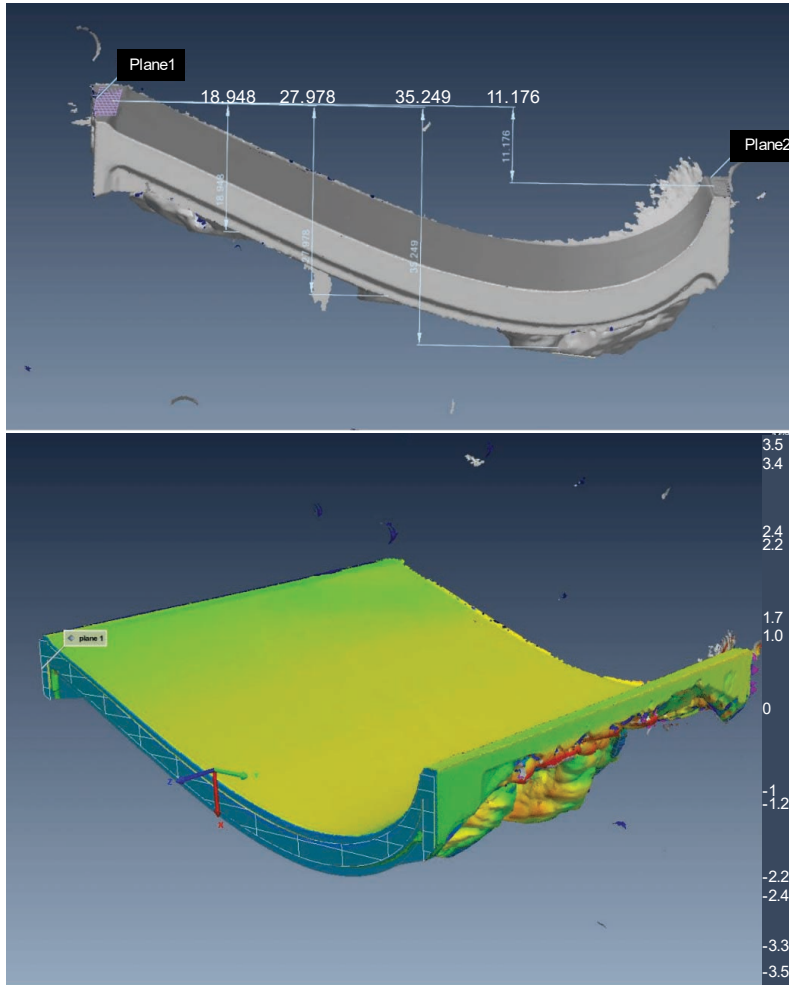
Figure 5.19 CMM inspection of the print iteration #3 (a.k.a. shell mold)

5.4.2.4 Printing Iteration 4

Hitherto, printings of a smaller scale have been evaluated for their conformance to intended dimensions and their performance in subsequent assessments, including vacuum integrity, heat transfer rates, and surface porosity metrics. Although these results are not extensively reported within the scope of this dissertation, they hold significance for the wind blade project.

In the course of the fourth iteration of the printing process, we aimed to upscale the model, transitioning from a 1:100 to a 1:20 scale. This enhancement would imply a part dimension of approximately 50x50x15cm, with an associated cost surpassing $80,000. Such a

substantial investment necessitates a corroborative justification deriving from the tests conducted

on smaller-scale models. These evaluations serve as precedent scenarios, providing invaluable

insight and validating the economic feasibility of large-scale production.
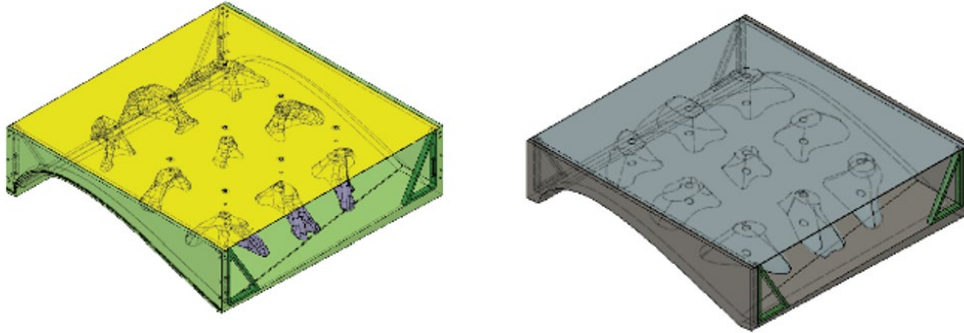
Figure 5.20 Design of molds for the printing iteration #4

The larger-scale molds were designed in two pieces, completing each other. While the

first printed one was planned to be tested for its dimensional accuracy, the other one was to make

it and complete a curvature surface mimicking the wind blade's aerodynamically favorable

surface.

Figure 5.21 DMDed and as-machined large-scale mold, back and front sides. The scale bar is not illustrated but the
distance between holes in the optical table is the same and is 1 inch.

In this step, as-printed parts were measured at their original fixture in DM3D and not reported due to the logistic hardship. Instead, the as-machined part underwent dimensional controls at the facilities of the University of Michigan.
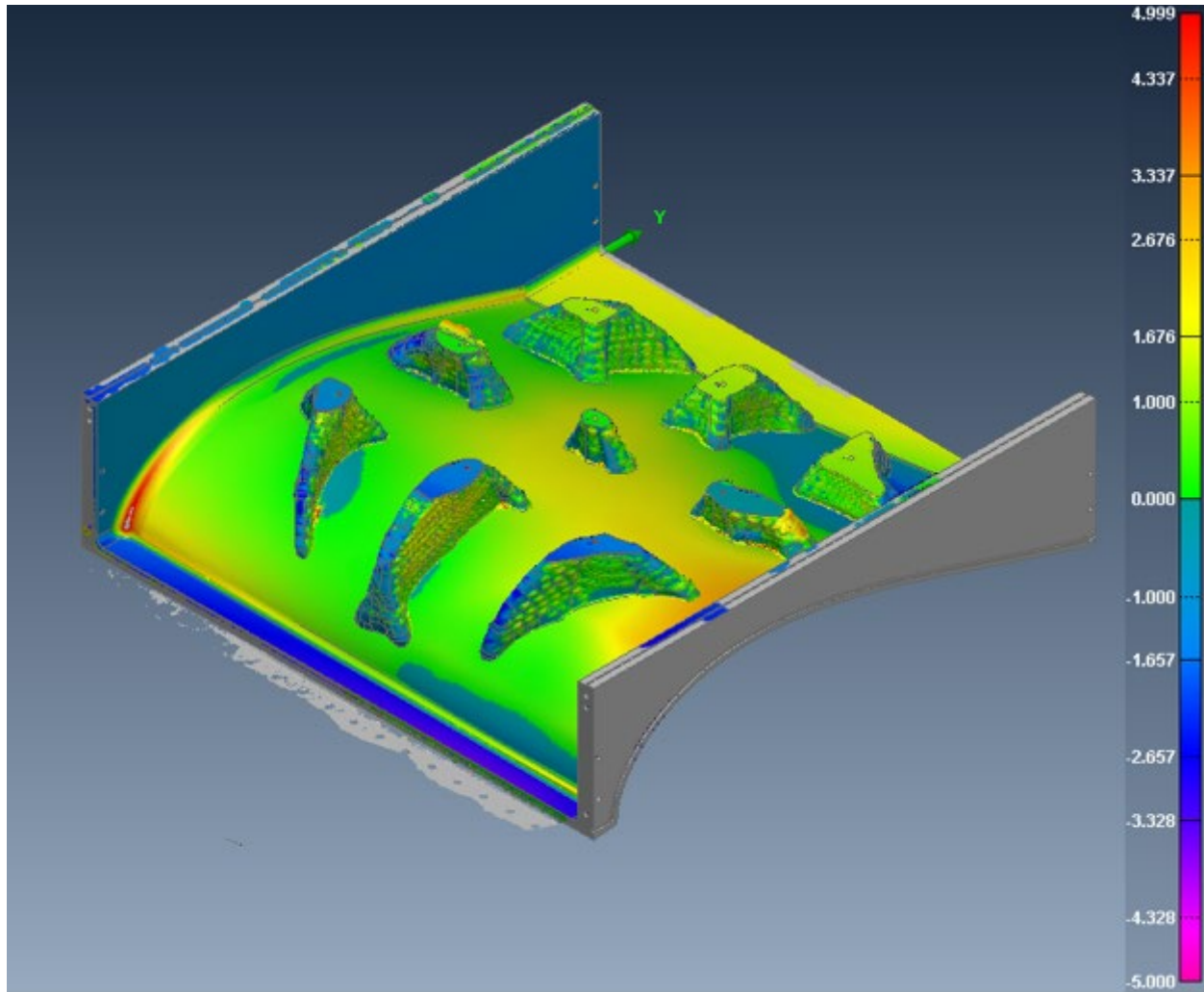
Figure 5.22 CMM measurement results for the back side of the printing iteration #4 mold. The color bar entries are in millimeters.
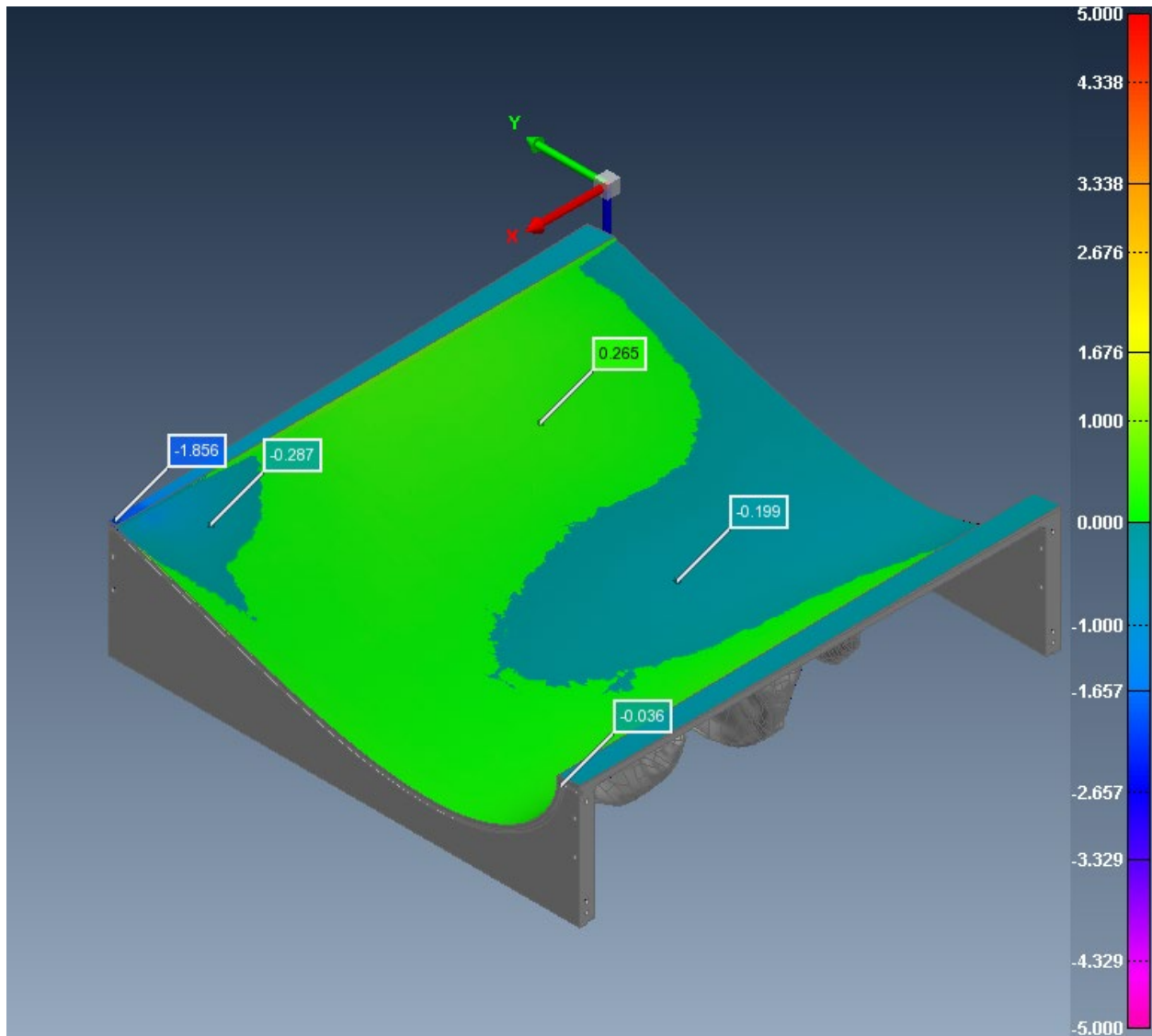
Figure 5.23 CMM measurement results for the surface side of the printing iteration #4 mold. The color bar entries are in millimeters.

As this project approached its final stages, a last measurement of its dimensional

accuracy was taken. The part is substantial, reaching 50cm in one dimension, which impedes free

mobility on the Coordinate Measuring Machine (CMM) optical bench. To overcome this

challenge, the part was scanned in two separate steps: first the back, then the surface side. These

two scans were subsequently combined into a single component using Polyworks software. The

color map shown in the figures above (Figure 5.22 Figure 5.23) depicts the deviation from the

original CAD data (Figure 5.20) and verifies its conformity to the project specifications.

5.5 Conclusion

RAM2 variant of Al 6061 is a promising candidate for big-area (when one of the dimensions exceeds 1 meter) prints. It results well in the line deposition and performs promising for the big coupons. Nevertheless, the necessity for secondary machining and handling processes remains paramount in attaining finished components that meet quality standards. The method we came up with also worked well for us to reach a final form of mold without an apparent dimensional disturbance. Considering these dynamics, the endeavor to fabricate scaled-down topologically optimized, qualified, and additively manufactured molds for wind blade production can be deemed successful.

In light of these findings, additional research is suggested. The author advocates for the drafting of a successive proposal geared towards full-scale applications continuing this project, with the aim of extending its benefits and further investigating its potential.

5.6 Notes

Chapter 6 Future works

Contemporary scientific progression typically transpires through incremental advancements as opposed to sizable leaps. Therefore, identifying the scope of a study and laying out the future work is integral to sustaining such a development pace. Possible ways to enhance this presented work are shared in subsequent sections.

6.1 Laser Surface Remelting of Al-Si alloys

LSR works are generally limited to a window between laser cutting to laser surface heating (below the phase-changing temperatures). As too much heat vaporizes the material, there will be no remaining material to inspect the effect of the laser. Should the power input not be adequate for phase changes, no effect will be observed. Therefore, faster laser scanning speeds, smaller beam diameters, and higher laser powers have been aimed so far. This processing window should be pushed to the boundaries as emerging technologies become widespread or readily available for research communities. Also, a thin-film deposition of hypereutectic Al-Si alloys can be tested with ultra-fast pulsed lasers to observe the final microstructures.

The microstructure refinement in the LSR can be increased. A former study found that for Si particles in an Al-Si binary system 40nm, the current dissertation proposed 30nm. A new study, though not published yet, will further reduce it to around 20nm. This progression must continue to a level of a perfect whisker and eventually to a glass transition point where no crystalline solidification occurs due to extreme cooling rates.

6.2 In situ Characterization of Laser-Processed Materials

In-situ mechanical testing for laser-processed alloys reveals great details about the material behavior. For the Al-Si example, Si fiber orientation varies within the Al matrix. Different orientations and alignments of Si fibers bring about different strengths of the material. The fracture mechanics of it must be studied and reported to the scientific community. When the technology allows, it must be revisited for elevated temperature and cold environment applications.

In-situ detection of metal additive manufacturing is probably the most important piece that is missing. When there is a proper way to analyze the printing processes for the defect formations and feedback control to mend it, the additive manufacturing sector will boom more than ever. To make this possible, in-situ detecting tools need to be used in combination, like a pyrometer and high-speed CCD camera or camera and spectrum analyzer. Then, those signals must be compared against the final parameter (porosity, hardness, chemical composition, layer height, etc), and meaningful datasets must be created. State-of-the-art data processing tools like convolutional neural network systems must be employed, as they are known for their data hunger.

6.3 Laser DMD of Large-Scale Applications

The presented work in Chapter 5 gives details about scaled-down wind blade mold production. This is a great foundation but requires a follow-up study for even greater goods: enhancement in wind harvesting for energy generation and reduction in costs. In this stage, problems become more funding issues than technical capacity, since the latter was proven in the chapter above. For future studies, it is thought to be useful to explore lighter and stronger materials alternative to Al. For the studies with the current selection (Al), topological

optimization must be enhanced to further reduce the cost and weight of the final molds and to further increase the airflow efficiency for faster heating and cooling cycles. Another metal additive manufacturing method that gained increased importance over the last few years with the increasing emphasis on BAAM is Wire-Arc Additive Manufacturing (WAAM). For the readily available wires, it can produce many times faster builds than DMD. With DMD's unique advantages in mind, the author suggests the exploration of that technology for larger-scale applications.

Appendix

Appendix A: Supplemental Tables for Chapter 3

Table 6.1 Process parameters used in the experiments.

Experiment Number	Laser Power (W)	Laser Scanning Speed (mm/s)
1	1200	30
2	1200	60
3	1200	90
4	1200	120
5	1200	160
6	1200	180
7	1500	60

Table 6.2 Aluminum spacing values within the melt pool.

Depth (μm)	SEM Image Number	Min. (nm)	Max. (nm)	Mean (nm)
213.95	1	12.73	139.39	36.29
194.50	2	11.80	77.32	23.78
175.05	3	8.21	59.09	22.13
155.60	4	7.87	52.34	15.70
136.15	5	8.34	46.36	15.30
116.70	6	7.70	43.50	16.76
97.25	7	6.05	34.30	15.34
77.80	8	5.12	30.73	14.36
58.35	9	5.45	23.61	12.65
38.90	10	5.62	29.83	22.55
19.45	11	3.82	22.47	10.94

Table 6.3 Silicon fiber diameters within a melt pool.

Depth (μm)	SEM Image Number	Min. (nm)	Max. (nm)	Mean (nm)
213.95	1	18.55	105.09	52.39
194.50	2	17.97	82.66	49.60
175.05	3	23.70	96.38	48.37
155.60	4	20.03	71.02	37.32
136.15	5	17.92	80.66	36.05
116.70	6	18.26	62.08	35.19
97.25	7	14.18	109.35	35.03
77.80	8	17.05	56.26	33.75
58.35	9	15.93	47.80	32.09
38.90	10	10.02	68.48	30.65
19.45	11	15.95	77.08	29.00

Table 6.4 Laser scanning process parameters.

Experiment Number	Power (W)	Scanning Speed (mm/s)	Laser Beam Diameter (mm)
1	187.5	25.4	0.4
2	375.0	25.4	0.4
3	562.5	25.4	0.4
4	187.5	101.6	0.4
5	375.0	101.6	0.4
6	562.5	101.6	0.4
7	187.5	177.8	0.4
8	375.0	177.8	0.4
9	562.5	177.8	0.4
10	750.0	25.4	2
11	1500.0	25.4	2
12	2250.0	25.4	2
13	750.0	101.6	2
14	1500.0	101.6	2
15	2250.0	101.6	2
16	750.0	177.8	2
17	1500.0	177.8	2
18	2250.0	177.8	2

Table 6.5 Eutectic formation for different experiment parameters.

Experiment Number	Eutectic Formation of Al-20Si		Eutectic Formation of Al-20Si-0.2Ce		Eutectic Formation of Al-20Si-0.2Sr	
	Total Area (in μm^2)	Percentage	Total Area (in μm^2)	Percentage	Total Area (in μm^2)	Percentage
1	3502.0	32.47%	2983.5	26.91%	11269.5	54.58%
2	25528.6	71.51%	6777.5	21.00%	50978.1	93.50%
3	50436.0	65.61%	6814.3	11.11%	85823.7	72.33%
4	301.0	2.97%	206.4	1.98%	304.9	1.82%
5	682.3	2.42%	0.0	0.00%	5696.0	10.19%
6	2339.1	5.05%	273.5	0.54%	27124.3	28.70%
7	1525.2	14.16%	183.6	1.59%	988.2	6.40%
8	2157.5	7.59%	0.0	0.00%	0.0	0.00%
9	10707.5	24.72%	0.0	0.00%	6246.7	8.04%
10	38384.2	20.27%	58671.0	12.19%	74450.3	12.26%
11	421665.5	33.60%	376566.2	29.29%	319443.3	27.84%
12	116915.8	7.82%	104641.0	7.88%	223802.7	17.97%
13	1576.3	2.97%	23519.3	3.80%	24559.2	14.63%
14	212394.3	37.03%	36856.2	5.27%	88232.0	14.15%
15	154943.6	16.95%	0.0	0.00%	44948.5	5.96%
16	0.0	0.00%	31319.8	7.54%	0.0	0.00%
17	92172.6	20.27%	264627.0	22.32%	42871.2	9.95%
18	218353.0	28.97%	41944.9	6.05%	248621.5	34.33%

Table 6.6 The list of the parameters and symbols for Equation 3.6.

Symbol	Explanation	Notes
a	Thermal diffusivity	
c	Specific heat	
G	Green's function	
k	Thermal conductivity	
n	Operating parameters	$n = qv/4\,\pi a^2 \rho C (T_c - T_0)$
q	Net heat input per unit time	(Power)
Q	Power distribution	
Q*	Heat source moving with v speed	
R	Distance to the center of arc	$R = \sqrt{w^2 + y^2 + z^2}$
R*	Dimensionless distance from the center of the arc	$R^* = \sqrt{\xi^{\wedge}2 + \psi^2 + \zeta^2}$
T	Temperature	
T_0	Ambient temperature	
T_c	Critical temperature	
u	Dimensionless distribution parameter	$u = v\sigma/2a$
v	Travel speed of arc	
w	Distance in x direction in a moving coordinate of speed v	$w = x - vt$
y	Y distance	
z	Z distance	
σ	Distribution parameter for beam	
ρ	Density	

δQ	Incremental amount of heat	
τ	Dimensionless time	
θ	Dimensionless temperature	$\theta = [T - T_0]/[T_c - T_0]$
ξ	Dimensionless distance in the moving coordinate	$\xi = vw/2a$
ψ	dimensionless distance y	
ζ	dimensionless distance z	
∞	infinity	

Table 6.7 Experiment parameters and the outputs.

Power (Watt)	Beam Dia (mm)	Feed Rate (0.01 inch/s)	Powder Deposition (Volt)	X Distance (mm)	Pattern	Layer Height (in mm)	Continuity
1000	2	5	2V	15	4 Layers - Linear	< 0.1	Not Continuous
1200	2	5	2V	15	4 Layers - Linear	1.7	Not Continuous
1200	2	5	2V	15	4 Layers - Linear	1.6	Not Continuous
1200	2	5	2V	15	4 Layers - Linear	1.9	Not Continuous
1200	2	5	2V	15	4 Layers - Linear		Not Continuous
1400	2	5	2V	15	4 Layers - Linear		Continuous
1600	2	5	2V	15	4 Layers - Linear		Continuous
1800	2	5	2V	15	4 Layers - Linear		Continuous
2000	2	5	2V	15	4 Layers - Linear		Not Continuous
2400	2	5	2V	15	4 Layers - Linear		Not Continuous
3000	2	5	2V	15	4 Layers - Linear		Continuous
1400	2	5	2V	15	4 Layers - Linear	1.5	Continuous
1400	2	5	2V	15	4 Layers - Linear	1.6	Continuous
1400	2	5	2V	15	4 Layers - Linear	1.8	Continuous
1400	2	5	2V	15	4 Layers - Linear	1.7	Continuous
1400	2	5	2V	15	2 Layers - Linear	1.9	Continuous
1400	2	5	2V	15	2 Layers - Linear	2.3	Continuous
1400	2	5	2V	15	2 Layers - Linear	2.4	Continuous
1400	2	5	2V	15	2 Layers - Linear	2.6	Continuous
1400	2	5	2V	15	2 Layers - Linear	2.7	Continuous

Bibliography

[1]   D. Strickland and G. Mourou, "Compression of amplified chirped optical pulses," *Opt. Commun.*, vol. 55, no. 6, pp. 447–449, Oct. 1985.

[2]   M. D. Hanna, S. Z. Lu, and A. Hellawell, "Modification in the Aluminum Silicon System.," *Metall. Trans. A, Phys. Metall. Mater. Sci.*, vol. 15 A, no. 3, pp. 459–469, 1984.

[3]   C. L. Xu, H. Y. Wang, F. Qiu, Y. F. Yang, and Q. C. Jiang, "Cooling rate and microstructure of rapidly solidified Al-20 wt.% Si alloy," *Mater. Sci. Eng. A*, vol. 417, no. 1–2, pp. 275–280, 2006.

[4]   Y. E. Kalay, L. S. Chumbley, I. E. Anderson, and R. E. Napolitano, "Characterization of hypereutectic Al-Si powders solidified under far-from equilibrium conditions," *Metall. Mater. Trans. A Phys. Metall. Mater. Sci.*, vol. 38 A, no. 7, pp. 1452–1457, Jul. 2007.

[5]   M. Pierantoni, M. Gremaud, P. Magnin, D. Stoll, and W. Kurz, "The coupled zone of rapidly solidified AlSi alloys in laser treatment," *Acta Metall. Mater.*, vol. 40, no. 7, pp. 1637–1644, 1992.

[6]   W. S. Miller *et al.*, "Recent development in aluminium alloys for the automotive industry," *Mater. Sci. Eng. A*, vol. 280, no. 1, pp. 37–49, Mar. 2000.

[7]   E. D. Self, "Aluminium and its alloys; with experimental investigations," *J. Franklin Inst.*, vol. 123, no. 3, pp. 209–226, 1887.

[8]   N. Tenekedjiev and J. E. Gruzleski, "Hypereutectic Aluminium-Silicon Casting Alloys— A Review," *http://dx.doi.org/10.1080/09554962.1990.11819026*, vol. 3, no. 2, pp. 96–

105, Apr. 2016.

[9]   Y. Q. Liu, S. H. Wei, J. Z. Fan, Z. L. Ma, and T. Zuo, "Mechanical Properties of a Low-thermal-expansion Aluminum/Silicon Composite Produced by Powder Metallurgy," *J. Mater. Sci. Technol.*, vol. 30, no. 4, pp. 417–422, Apr. 2014.

[10]   J. L. Murray and A. J. McAlister, "The Al-Si (Aluminum-Silicon) system," *Bull. Alloy Phase Diagrams*, vol. 5, no. 1, pp. 74–84, Feb. 1984.

[11]   J. Wu, X. Q. Wang, W. Wang, M. M. Attallah, and M. H. Loretto, "Microstructure and strength of selectively laser melted AlSi10Mg," *Acta Mater.*, vol. 117, pp. 311–320, Sep. 2016.

[12]   Q. Lei, B. P. Ramakrishnan, S. Wang, Y. Wang, J. Mazumder, and A. Misra, "Structural refinement and nanomechanical response of laser remelted Al-Al2Cu lamellar eutectic," *Mater. Sci. Eng. A*, vol. 706, pp. 115–125, Oct. 2017.

[13]   "Atomic Spectra Database." [Online]. Available: https://www.nist.gov/pml/atomic-spectra-database.

[14]   L. Song, C. Wang, and J. Mazumder, "Identification of phase transformation using optical emission spectroscopy for direct metal deposition process," in *High Power Laser Materials Processing: Lasers, Beam Delivery, Diagnostics, and Applications*, 2012, vol. 8239, p. 82390G.

[15]   L. Song, W. Huang, X. Han, and J. Mazumder, "Real-Time Composition Monitoring Using Support Vector Regression of Laser-Induced Plasma for Laser Additive Manufacturing," *IEEE Trans. Ind. Electron.*, vol. 64, no. 1, pp. 633–642, Jan. 2017.

[16]   J. Choi, M. Wooldridge, and J. Mazumder, "Spectroscopy-based smart optical monitoring system in the applications of laser additive manufacturing," *J. Laser Appl.*, vol. 35, no. 1,

Feb. 2023.

[17] B. Sjögren, A. Iregren, J. Montelius, and R. A. Yokel, *Aluminum*, Fourth Edi., vol. 1. Elsevier, 2015.

[18] J. Palazzo and R. Geyer, "Consequential life cycle assessment of automotive material substitution: Replacing steel with aluminum in production of north American vehicles," *Environ. Impact Assess. Rev.*, vol. 75, no. April 2018, pp. 47–58, 2019.

[19] Y. Kusuda, "Honda develops robotized FSW technology to weld steel and aluminum and applied it to a mass-production vehicle," *Industrial Robot*, vol. 40, no. 3. pp. 208–212, 2013.

[20] A. Gullino, P. Matteis, and F. D. Aiuto, "Review of aluminum-to-steel welding technologies for car-body applications," *Metals (Basel).*, vol. 9, no. 3, pp. 1–28, 2019.

[21] A. K. Dahle, K. Nogita, S. D. McDonald, C. Dinnis, and L. Lu, "Eutectic modification and microstructure development in Al-Si Alloys," *Mater. Sci. Eng. A*, vol. 413–414, pp. 243–248, 2005.

[22] L. F. Mondolfo, "Al–Si Aluminum–Silicon system," *Alum. Alloy.*, pp. 368–376, 1976.

[23] M. Haghshenas and J. Jamali, "Assessment of circumferential cracks in hypereutectic Al-Si clutch housings," *Case Stud. Eng. Fail. Anal.*, vol. 8, pp. 11–20, 2017.

[24] Q. Li, T. Xia, Y. Lan, W. Zhao, L. Fan, and P. Li, "Effect of rare earth cerium addition on the microstructure and tensile properties of hypereutectic Al-20%Si alloy," *J. Alloys Compd.*, vol. 562, pp. 25–32, 2013.

[25] D. Lu, Y. Jiang, G. Guan, R. Zhou, Z. Li, and R. Zhou, "Refinement of primary Si in hypereutectic Al-Si alloy by electromagnetic stirring," *J. Mater. Process. Technol.*, vol. 189, no. 1–3, pp. 13–18, 2007.

[26] H. K. Feng, S. R. Yu, Y. L. Li, and L. Y. Gong, "Effect of ultrasonic treatment on microstructures of hypereutectic Al-Si alloy," *J. Mater. Process. Technol.*, vol. 208, no. 1–3, pp. 330–335, 2008.

[27] J. E. Plumb, R C; Lewis, "THE MODIFICATION OF ALUMINIUM-SILICON ALLOYS BY SODIUM (Journal Article) | OSTI.GOV," 1958. [Online]. Available: https://www.osti.gov/biblio/4329718. [Accessed: 19-Jul-2021].

[28] G. L. Zhu, N. J. Gu, and B. J. Zhou, "Effects of Combining Na and Sr additions on Eutectic Modification in Al-Si alloy," *IOP Conf. Ser. Mater. Sci. Eng.*, vol. 230, no. 1, 2017.

[29] R. E. N. Bo and W. M. E, "Influences of complex modification of P and RE on microstructure and.pdf," 2007.

[30] B. Dang, Z. Jian, and J. Xu, "Effect of pulsed magneto oscillation and phosphorus on microstructure and tensile properties of as-cast Al-25% Si alloy," *Int. J. Mater. Res.*, vol. 112, no. 4, pp. 295–302, 2021.

[31] E. Aghaie, J. Stroh, D. Sediako, A. Rashidi, and A. S. Milani, "Improving the mechanical properties of the B319 aluminum alloy by addition of cerium," *Mater. Sci. Eng. A*, vol. 793, no. March, p. 139899, 2020.

[32] A. S. Anasyida, A. R. Daud, and M. J. Ghazali, "Dry sliding wear behaviour of Al-12Si-4Mg alloy with cerium addition," *Mater. Des.*, vol. 31, no. 1, pp. 365–374, 2010.

[33] M. Timpel *et al.*, "The role of strontium in modifying aluminium-silicon alloys," *Acta Mater.*, vol. 60, no. 9, pp. 3920–3928, 2012.

[34] Q. Li *et al.*, "Modification of Hypereutectic Al–20 wt%Si Alloy Based on the Addition of Yttrium and Al–5Ti–1B Modifiers Mixing Melt," *Int. J. Met.*, vol. 13, no. 2, pp. 367–383,

2019.

[35] E. M. Elgallad, H. W. Doty, S. A. Alkahtani, and F. H. Samuel, "Effects of la and Ce
      Addition on the Modification of Al-Si Based Alloys," *Adv. Mater. Sci. Eng.*, vol. 2016,
      2016.

[36] F. Mao *et al.*, "Different influences of Rare Earth Eu Addition on primary Si Refinement
      in hypereutectic Al-Si alloys with varied purity," *Materials (Basel).*, vol. 12, no. 21, 2019.

[37] F. Mao *et al.*, "Modification Mechanism of Rare Earth Eu on Eutectic Si in Hypoeutectic
      Al-Si Alloy," *Int. J. Met.*, no. February, 2021.

[38] D. H. Xiao, M. Song, K. H. Chen, and B. Y. Huang, "Effect of rare earth Yb addition on
      mechanical properties of Al-5·3Cu-0·8Mg-0·6Ag alloy," *Mater. Sci. Technol.*, vol. 23, no.
      10, pp. 1156–1160, 2007.

[39] W. Shi, B. Gao, G. Tu, S. Li, Y. Hao, and F. Yu, "Effect of neodymium on primary silicon
      and mechanical properties of hypereutectic Al-15Si alloy," *J. Rare Earths*, vol. 28, no.
      SUPPL. 1, pp. 367–370, 2010.

[40] M. Gamal Mahmoud, Y. Zedan, A.-M. Samuel, V. Songmene, H. W. Doty, and F. H.
      Samuel, "Applications of Rare Earth Metals in Al-Si Cast Alloys," *Adv. High-Entropy
      Alloy. - Mater. Res. Exot. Prop. Appl. [Working Title]*, vol. 2, no. c, 2021.

[41] C. L. Xu, H. Y. Wang, F. Qiu, Y. F. Yang, and Q. C. Jiang, "Cooling rate and
      microstructure of rapidly solidified Al–20 wt.% Si alloy," *Mater. Sci. Eng. A*, vol. 417, no.
      1–2, pp. 275–280, Feb. 2006.

[42] C. H. Olk, M. Lukitsch, and D. B. Haddad, "Combinatorial investigation of the
      mechanical properties of aluminum-silicon thin film nanocomposites," *J. Mater. Res.*, vol.
      22, no. 4, pp. 1029–1036, 2007.

[43] Z. Cai, R. Wang, C. Zhang, C. Peng, L. Xie, and L. Wang, "Characterization of Rapidly Solidified Al-27 Si Hypereutectic Alloy: Effect of Solidification Condition," *J. Mater. Eng. Perform.*, vol. 24, no. 3, pp. 1226–1236, 2015.

[44] H. Pouraliakbar *et al.*, "Processing of Al-Cu-Mg alloy by FSSP: Parametric analysis and the effect of cooling environment on microstructure evolution," *Mater. Lett.*, vol. 308, Feb. 2022.

[45] L. Chen, Z. Liu, X. Wang, Q. Wang, and X. Liang, "Effects of Surface Roughness Parameters on Tribological Performance for Micro-textured Eutectic Aluminum-Silicon Alloy," *J. Tribol.*, vol. 142, no. 2, pp. 1–13, 2020.

[46] W. R. Osório, N. Cheung, J. E. Spinelli, K. S. Cruz, and A. Garcia, "Microstructural modification by laser surface remelting and its effect on the corrosion resistance of an Al– 9 wt%Si casting alloy," *Appl. Surf. Sci.*, vol. 254, no. 9, pp. 2763–2770, Feb. 2008.

[47] R. A. Savrai, I. Y. Malygina, and Y. M. Kolobylin, "An Approach to Eddy-Current Evaluation of the Structural State in a Cast Aluminum–Silicon Alloy Subjected to Surface Laser Heat Treatment," *J. Nondestruct. Eval.*, vol. 38, no. 3, pp. 1–7, 2019.

[48] S. Mahanty and Gouthama, "Surface modification of Al-Si alloy by excimer laser pulse processing," *Mater. Chem. Phys.*, vol. 173, pp. 192–199, 2016.

[49] Y. Zhang *et al.*, "metals Ultrasonic-Assisted Laser Metal Deposition of the Al 4047Alloy," 2019.

[50] H. H. Lien, J. Mazumder, J. Wang, and A. Misra, "Microstructure evolution and high density of nanotwinned ultrafine Si in hypereutectic Al-Si alloy by laser surface remelting," *Mater. Charact.*, vol. 161, no. January, p. 110147, 2020.

[51] T. W. Eagar and N. S. Tsai, "Temperature Fields Produced By Traveling Distributed Heat

Sources.," *Weld. J. (Miami, Fla)*, vol. 62, no. 12, pp. 346–355, 1983.

[52] D. Dheerendra, *Production and Properties of Cast Al-Si Alloys*. 2013.

[53] J. G. (John G. Kaufman, "Properties of aluminum alloys : tensile, creep, and fatigue data at high and low temperatures," p. 305, 1999.

[54] R. Hernandez, Francisco C Robles and Ramirez, Jose Martin Herrera and Mackay, *Al-Si alloys: automotive, aeronautical, and aerospace applications*. Springer, 2017.

[55] T. H. Ludwig, P. L. Schaffer, and L. Arnberg, "Influence of phosphorus on the nucleation of eutectic silicon in Al-Si alloys," *Metall. Mater. Trans. A Phys. Metall. Mater. Sci.*, vol. 44, no. 13, pp. 5796–5805, Dec. 2013.

[56] Y. Wu, S. Wang, H. Li, and X. Liu, "A new technique to modify hypereutectic Al–24%Si alloys by a Si–P master alloy," *J. Alloys Compd.*, vol. 477, no. 1–2, pp. 139–144, May 2009.

[57] M. Faraji, I. Todd, and H. Jones, "Effect of phosphorus and strontium additions on formation temperature and nucleation density of primary silicon in Al-19 Wt Pct Si alloy and their effect on eutectic temperature," *Metall. Mater. Trans. A Phys. Metall. Mater. Sci.*, vol. 40, no. 7, pp. 1710–1715, May 2009.

[58] Q. Li, B. Li, J. Li, Y. Zhu, and T. Xia, "Effect of yttrium addition on the microstructures and mechanical properties of hypereutectic Al-20Si alloy," *Mater. Sci. Eng. A*, vol. 722, pp. 47–57, Apr. 2018.

[59] Q. Li, T. Xia, Y. Lan, P. Li, and L. Fan, "Effects of rare earth Er addition on microstructure and mechanical properties of hypereutectic Al–20% Si alloy," *Mater. Sci. Eng. A*, vol. 588, pp. 97–102, Dec. 2013.

[60] M. Zuo, D. Zhao, X. Teng, H. Geng, and Z. Zhang, "Effect of P and Sr complex

modification on Si phase in hypereutectic Al–30Si alloys," *Mater. Des.*, vol. 47, pp. 857–864, May 2013.

[61]   Q. Wang, Q. Hao, and W. Yu, "Effect of Strontium Modification on Porosity Formation in A356 Alloy," *Int. J. Met.*, vol. 13, no. 4, pp. 944–952, Oct. 2019.

[62]   H. C. Liao, W. Song, Q. G. Wang, L. Zhao, R. Fan, and F. Jia, "Effect of Sr addition on porosity formation in directionally solidified A356 alloy," *Int. J. Cast Met. Res.*, vol. 26, no. 4, pp. 201–208, Aug. 2013.

[63]   J. Abboud and J. Mazumder, "Developing of nano sized fibrous eutectic silicon in hypereutectic Al–Si alloy by laser remelting," *Sci. Reports 2020 101*, vol. 10, no. 1, pp. 1–18, Jul. 2020.

[64]   J. H. Abboud and J. Mazumder, "Ultra-refined primary and eutectic silicon in rapidly solidified laser produced hypereutectic Al–Si alloys," *Adv. Mater. Process. Technol.*, vol. 8, no. 3, pp. 2510–2532, Jul. 2022.

[65]   H. H. Lien, J. Mazumder, J. Wang, and A. Misra, "Ultrahigh strength and plasticity in laser rapid solidified Al–Si nanoscale eutectics," *Mater. Res. Lett.*, vol. 8, no. 8, pp. 291–298, Aug. 2020.

[66]   H. H. Lien, J. Mazumder, J. Wang, and A. Misra, "Ultrahigh strength and plasticity in laser rapid solidified Al–Si nanoscale eutectics," *Mater. Res. Lett.*, vol. 8, no. 8, pp. 291–298, 2020.

[67]   L. Z. Zhao, M. J. Zhao, L. J. Song, and J. Mazumder, "Ultra-fine Al–Si hypereutectic alloy fabricated by direct metal deposition," *Mater. Des.*, vol. 56, pp. 542–548, Apr. 2014.

[68]   A. Bhowmik, Y. Yang, W. Zhou, Y. Chew, and G. Bi, "On the heterogeneous cooling rates in laser-clad Al-50Si alloy," *Surf. Coatings Technol.*, vol. 408, p. 126780, Feb. 2021.

[69] A. Chaus, E. Marukovich, and M. Sahul, "Effect of Rapid Quenching on the Solidification Microstructure, Tensile Properties and Fracture of Secondary Hypereutectic Al-18%Si-2%Cu Alloy," *Met. 2020, Vol. 10, Page 819*, vol. 10, no. 6, p. 819, Jun. 2020.

[70] S. Tomida, K. Nakata, S. Shibata, I. Zenkouji, and S. Saji, "Improvement in wear resistance of hyper-eutectic Al-Si cast alloy by laser surface remelting," *Surface and Coatings Technology*, vol. 169–170. pp. 468–471, 2003.

[71] L. Song and J. Mazumder, "IN-SITU SPECTROSCOPIC ANALYSIS OF LASER INDUCED PLASMA FOR MONITORING OF COMPOSITION DURING DIRECT METAL DEPOSITION PROCESS Paper Number 408."

[72] L. Song and J. Mazumder, "Real time Cr measurement using optical emission spectroscopy during direct metal deposition process," *IEEE Sens. J.*, vol. 12, no. 5, pp. 958–964, 2012.

[73] L. Song, C. Wang, and J. Mazumder, "Identification of phase transformation using optical emission spectroscopy for direct metal deposition process," *https://doi.org/10.1117/12.908264*, vol. 8239, pp. 120–128, Feb. 2012.

[74] J. Shin and J. Mazumder, "Plasma diagnostics using optical emission spectroscopy in laser drilling process," *J. Laser Appl.*, vol. 28, no. 2, May 2016.

[75] J. Shin and J. Mazumder, "Composition monitoring using plasma diagnostics during direct metal deposition (DMD) process," *Opt. Laser Technol.*, vol. 106, pp. 40–46, Oct. 2018.

[76] W. Sun, Z. Zhang, W. Ren, J. Mazumder, and J. J. Jin, "In Situ Monitoring of Optical Emission Spectra for Microscopic Pores in Metal Additive Manufacturing," *J. Manuf. Sci. Eng. Trans. ASME*, vol. 144, no. 1, Jan. 2022.

[77] W. Ren and J. Mazumder, "In-situ porosity recognition for laser additive manufacturing of

7075-Al alloy using plasma emission spectroscopy," *Sci. Rep.*, vol. 10, no. 1, Dec. 2020.

[78]   J. Choi, J. Mazumder, and A. Rice, "Innovative Additive Manufacturing Process for Successful Production of 7000 Series Aluminum Alloy Components Using Smart Optical Monitoring System," *SAE Tech. Pap.*, vol. 2020-April, no. April, pp. 1–15, 2020.

[79]   "The third industrial revolution via the Economist 2012," 2012. [Online]. Available: https://www.economist.com/leaders/2012/04/21/the-third-industrial-revolution.

[80]   Y. Q. Liu, S. H. Wei, J. Z. Fan, Z. L. Ma, and T. Zuo, "Mechanical properties of a low-thermal-expansion aluminum/silicon composite produced by powder metallurgy," *J. Mater. Sci. Technol.*, vol. 30, no. 4, pp. 417–422, 2014.

[81]   Q. Lei, B. P. Ramakrishnan, S. Wang, Y. Wang, J. Mazumder, and A. Misra, "Structural refinement and nanomechanical response of laser remelted Al-Al2Cu lamellar eutectic," *Mater. Sci. Eng. A*, vol. 706, no. September, pp. 115–125, 2017.

[82]   J. Choi, M. Wooldridge, and J. Mazumder, "Spectroscopy-based smart optical monitoring system in the applications of laser additive manufacturing," *J. Laser Appl.*, vol. 35, no. 1, p. 012030, 2023.

[83]   H. H. Lien, J. Mazumder, J. Wang, and A. Misra, "Microstructure evolution and high density of nanotwinned ultrafine Si in hypereutectic Al-Si alloy by laser surface remelting," *Mater. Charact.*, vol. 161, no. October 2019, p. 110147, 2020.

[84]   M. Kayitmazbatir, H. H. Lien, J. Mazumder, J. Wang, and A. Misra, "Effect of Cooling Rate on Nano-Eutectic Formation in Laser Surface Remelted and Rare Earth Modified Hypereutectic Al-20Si Alloys," *Cryst. 2022, Vol. 12, Page 750*, vol. 12, no. 5, p. 750, May 2022.

[85]   B. Wei *et al.*, "In situ characterization of tensile behavior of laser rapid solidified Al–Si

heterogeneous microstructures," *Mater. Res. Lett.*, vol. 9, no. 12, pp. 507–515, 2021.

[86]   G. P. Dinda, A. K. Dasgupta, and J. Mazumder, "Evolution of microstructure in laser deposited Al-11.28%Si alloy," *Surf. Coatings Technol.*, vol. 206, no. 8–9, pp. 2152–2160, 2012.

[87]   C. A. Schneider, W. S. Rasband, and K. W. Eliceiri, "NIH Image to ImageJ: 25 years of image analysis," *Nat. Methods 2012 97*, vol. 9, no. 7, pp. 671–675, Jun. 2012.

[88]   P. Chokemorh *et al.*, "Primary Si refinement and eutectic Si modification in Al-20Si via P-Ce addition," vol. 2022, pp. 1–21, 2022.

[89]   J. D. Roehling *et al.*, "Rapid solidification growth mode transitions in Al-Si alloys by dynamic transmission electron microscopy," *Acta Mater.*, vol. 131, pp. 22–30, 2017.

[90]   G. Grimvall, *Thermophysical properties of materials*. 1999.

[91]   W. Hearn, A. A. Bogno, J. Spinelli, J. Valloton, and H. Henein, "Microstructure Solidification Maps for Al-10 Wt Pct Si Alloys," *Metall. Mater. Trans. A Phys. Metall. Mater. Sci.*, vol. 50, no. 3, pp. 1333–1345, 2019.

[92]   S. Khan and R. Elliott, "Quench modification of aluminium-silicon eutectic alloys," *J. Mater. Sci.*, vol. 31, no. 14, pp. 3731–3737, 1996.

[93]   P. A, "No Title," 1, 387, 900, 1921.

[94]   L. Qiyang, L. Qingchun, and L. Qifu, "Modification of Al☐Si alloys with sodium," *Acta Metall. Mater.*, vol. 39, no. 11, pp. 2497–2502, Nov. 1991.

[95]   G. Liu, G. Li, A. Cai, and Z. Chen, "The influence of Strontium addition on wear properties of Al-20wt% Si alloys under dry reciprocating sliding condition," *Mater. Des.*, vol. 32, no. 1, pp. 121–126, 2011.

[96]   S. S. Shin, E. S. Kim, G. Y. Yeom, and J. C. Lee, "Modification effect of Sr on the

microstructures and mechanical properties of Al–10.5Si–2.0Cu recycled alloy for die casting," *Mater. Sci. Eng. A*, vol. 532, pp. 151–157, Jan. 2012.

[97]   A. Knuutinen, K. Nogita, S. D. McDonald, and A. K. Dahle, "Modification of Al–Si alloys with Ba, Ca, Y and Yb," *J. Light Met.*, vol. 1, no. 4, pp. 229–240, Nov. 2001.

[98]   K. Nogita, S. D. McDonald, and A. K. Dahle, "Eutectic Modification of Al-Si Alloys with Rare Earth Metals," *Mater. Trans.*, vol. 45, no. 2, pp. 323–326, 2004.

[99]   Q. Li, B. Li, J. Li, Y. Zhu, and T. Xia, "Effect of yttrium addition on the microstructures and mechanical properties of hypereutectic Al-20Si alloy," *Mater. Sci. Eng. A*, vol. 722, no. February, pp. 47–57, 2018.

[100]   Q. Li, T. Xia, Y. Lan, P. Li, and L. Fan, "Effects of rare earth Er addition on microstructure and mechanical properties of hypereutectic Al-20% Si alloy," *Mater. Sci. Eng. A*, vol. 588, pp. 97–102, 2013.

[101]   L. Z. Zhao, M. J. Zhao, L. J. Song, and J. Mazumder, "Ultra-fine Al-Si hypereutectic alloy fabricated by direct metal deposition," *Mater. Des.*, vol. 56, pp. 542–548, 2014.

[102]   A. Bhowmik, Y. Yang, W. Zhou, Y. Chew, and G. Bi, "On the heterogeneous cooling rates in laser-clad Al-50Si alloy," *Surf. Coatings Technol.*, vol. 408, no. September 2020, p. 126780, 2021.

[103]   K. Nakata and M. Ushio, "Wear resistance of plasma sprayed Al–Si binary alloy coatings on A6063 Al alloy substrate," *Surf. Coatings Technol.*, vol. 142–144, pp. 277–282, Jul. 2001.

[104]   ROSENTHAL and D., "The Theory of Moving Sources of Heat and Its Application of Metal Treatments," *Trans. ASME*, vol. 68, pp. 849–866, 1946.

[105]   K. Nogita, J. Drennan, and A. K. Dahle, "Evaluation of Silicon Twinning in Hypo-

Eutectic Al-Si Alloys," *Mater. Trans.*, vol. 44, no. 4, pp. 625–628, 2003.

[106] X. W. Gu, Z. Wu, Y. W. Zhang, D. J. Srolovitz, and J. R. Greer, "Microstructure versus flaw: Mechanisms of failure and strength in nanostructures," *Nano Lett.*, vol. 13, no. 11, pp. 5703–5709, Nov. 2013.

[107] J. Ye, R. K. Mishra, A. K. Sachdev, and A. M. Minor, "In situ TEM compression testing of Mg and Mg–0.2 wt.% Ce single crystals," *Scr. Mater.*, vol. 64, no. 3, pp. 292–295, Feb. 2011.

[108] L. Borkowski, J. A. Sharon, and A. Staroselsky, "In Situ Micromechanical Testing for Single Crystal Property Characterization," *Metall. Mater. Trans. A Phys. Metall. Mater. Sci.*, vol. 49, no. 12, pp. 6022–6033, Dec. 2018.

[109] P. G. Allison, R. D. Moser, J. P. Schirer, R. L. Martens, J. B. Jordon, and M. Q. Chandler, "In-situ nanomechanical studies of deformation and damage mechanisms in nanocomposites monitored using scanning electron microscopy," *Mater. Lett.*, vol. 131, pp. 313–316, Sep. 2014.

[110] A. Haboub *et al.*, "Tensile testing of materials at high temperatures above 1700°C with in situ synchrotron X-ray micro-tomography," *Rev. Sci. Instrum.*, vol. 85, no. 8, p. 83702, Aug. 2014.

[111] E. M. Sefene, Y. M. Hailu, and A. A. Tsegaw, "Metal hybrid additive manufacturing: state-of-the-art," *Prog. Addit. Manuf.*, vol. 7, no. 4, pp. 737–749, Aug. 2022.

[112] I. Segovia Ramírez, F. P. García Márquez, and M. Papaelias, "Review on additive manufacturing and non-destructive testing," *J. Manuf. Syst.*, vol. 66, pp. 260–286, Feb. 2023.

[113] D. Ashkenazi, "How aluminum changed the world: A metallurgical revolution through

technological and cultural perspectives," *Technol. Forecast. Soc. Change*, vol. 143, pp. 101–113, Jun. 2019.

[114] S. C. Altıparmak, V. A. Yardley, Z. Shi, and J. Lin, "Challenges in additive manufacturing of high-strength aluminium alloys and current developments in hybrid additive manufacturing," *Int. J. Light. Mater. Manuf.*, vol. 4, no. 2, pp. 246–261, Jun. 2021.

[115] L. J. Love, "Utility of Big Area Additive Manufacturing (BAAM) For The Rapid Manufacture of Customized Electric Vehicles," Aug. 2015.

[116] K. G. Prashanth, S. Scudino, T. Maity, J. Das, and J. Eckert, "Is the energy density a reliable parameter for materials synthesis by selective laser melting?," *Mater. Res. Lett.*, vol. 5, no. 6, pp. 386–390, 2017.